Characterization of Dielectric-Silicon Structure by Photoreflectance Spectroscopy

フォトレフレクタンス分光法による誘電体-シリコン構造の評価に関する研究

Masayuki SOHGAWA

寒川雅之

Department of Physical Science
Graduate School of Engineering Science
Osaka University

January 2005

Abstract

Dielectric thin film/Si structures have been characterized by photoreflectance spectroscopy (PRS). The relationship between PRS spectrum and basic property of the dielectric film has been theoretically studied. The shape of PRS spectrum varies by light interference in thick (> 100 nm) and high refractive dielectric film in insulator/Si structure. PRS spectral intensity is expressed as a function of Si surface potential in insulator/Si structure. Since Si surface potential depends upon thickness and dielectric constant of dielectric film, they can be characterized by PRS spectral intensity.

SiO_2/Si structures have been characterized by PRS. E_1 critical point obtained by PRS spectrum linearly decreases with increasing tensile stress at surface of Si diaphragm structure. The growth of native Si oxide has been monitored by PRS. PRS spectral intensity increases and E_1 critical point decreases with growth of native oxide. This suggests that Si surface stress increases with growth of native oxide. From these results, a model of native oxidation mechanism has been suggested from discussion of PRS spectrum change. Moreover, thermally-oxidized SiO_2/Si structures have been also evaluated. The tensile stress at Si surface decreases with increasing temperature of thermal oxidation.

The dielectric films which have higher dielectric constant (high-k films) have been characterized by PRS. The high-k films (HfO_2, PrO_x) were mainly prepared by pulsed laser deposition (PLD). It is found that PRS spectral intensity is reduced by existence of positive charges caused by oxygen vacancy in high-k film. The suitable deposition and rapid thermal annealing (RTA) conditions of high-k films have been investigated. PRS spectral intensity becomes small in the case of deposition in N_2 atmosphere because of existence of large positive charge in the film. Moreover, the spectral intensity increases with increasing deposition temperature. It is considered that high-k films which have higher dielectric constant is obtained for deposition at higher temperature. PRS spectral intensity of high-k/Si treated by RTA in N_2 and O_2 at 600°C is the largest. At more than 600°C, the interfacial layer growth reduces dielectric constant so that PRS spectral intensity decreases. As a result, it is considered that 600°C is suitable temperature for RTA in N_2 or O_2 atmosphere.

Metal-ferroelectric-insulator-semiconductor (MFIS) structures have been characterized by PRS.

$SrBi_2Ta_2O_9$ (SBT) was used for the ferroelectric material in this study. It is found that PRS spectral intensity is closely related to the ferroelectricity of SBT film. PRS spectral intensity increases after poling process by negative voltage. It is considered that Si surface potential is increased by remanent polarization in SBT film, so that the memorized states of MFIS structure can be characterized by PRS. PRS spectral intensity gradually decreases with increasing retained time of SBT/SiO_2/Si after poling. Decrease of the spectral intensity is suppressed by introducing RTA in deposition process. This result means that retention property of SBT/SiO_2/Si structure is improved by RTA.

Acknowledgments

This work has been done at Okuyama Laboratory, Electronic Information Device Group, Area of Solid State Electronics, Division of Advanced Electronics and Optical Science, Department of Systems Innovation, Graduate School of Engineering Science, Osaka University.

Firstly, I would like to express my sincere gratitude to Prof. Masanori Okuyama in Osaka University for his valuable suggestions and constant encouragement throughtout the course of this thesis work. This thesis would not have been completed without his continuous direction and support. I am deeply grateful to Prof. Mikio Takai and Prof. Hiroaki Okamoto in Osaka University for their careful reading of the manuscript and helpful discussions. I also would like to express my sincere appreciation to Ass. Prof. Minoru Noda, Dr. Kaoru Yamashita, Dr. Takeshi Kanashima and Mr. Chitose Sada in Osaka University, for their continuous supports during the course of this thesis work.

I wish to express my appreciation to Prof. Akira Fujimoto, who was my supervisor in Wakayama National College of Technology and is my collaborator during the course of this thesis work, for his practical suggestions and discussions. I would like to express my respectful thanks to Mr. Masashi Agata in Fujitsu Ltd., Mr. Satoshi Kitai in Canon Inc., Mr. Hirofumi Kanda in Sharp Corporation, Mr. Satoshi Fujita in NEC Corporation and Mr. Koji Ikeda in Toshiba Corporation, who were co-workers in Okuyama Laboratory, and Mr. Masato Yoshida, Mr. Taizou Tada, Mr. Takuji Naoyama, Mr. Jun-ya Matsumoto and Mr. Masaki Tsumori, who are co-workers in Okuyama Laboratory, for their kind support in my experiments for this thesis.

I am indebted to Dr. Osamu Maida in The Institute of Scientific and Industrial Research, Osaka University, Dr. Zhinqiang Wei in Matsushita Electric Industrial Co., Ltd., Dr. Mitsue Takahashi in National Institute of Advanced Industrial Science and Technology, Mr. Kazushi Kodama in Fuji Photo Film Co., Ltd., Mr. Toshiaki Fukunaga in Sanyo Electric Co., Ltd., Mr. Yoshihide Toyoshima in Onkyo Corporation, Mr. Hideyuki Murakami in Matsushita Electric Industrial Co., Ltd., Latpasamixay Chansomphou in Asahi Kasei Corporation, Keiji Nishimura in Yamaha Corporation, Gen Hirooka in Toyota Corporation, Ltd., who are former members of Okuyama Laboratory, for their kind guidance and their technical assistance in this work, and also Dr. Dan Ricinschi, Mr. Akira Shibuya, Mr. Kwi-Young Yun, Mr. Daniel Popovici, Mr. Bong-Yeon Lee, Mr. Yoji

Sakioka, Mr. Hiroki Nishimoto, Mr. Masakazu Hirakawa, Mr. Shin-ichi Ikemori, Mr. Keisuke Takahashi, Ms. Misato Nakayama and Ms. Yuko Miyakai and all members of Okuyama Laboratory, for their supports during the period of my study.

Finally, I would like to express my deepest gratitude to my parents Susumu and Ryouko, and also my brother Ryuji and Keiji and my sister Rumi, for their constant supports and encouragements, and dedicate this thesis to my revered defunct grandfather Tomekazu.

Masayuki SOHGAWA

Contents

Chapter 1

Introduction

1.1 Background

1.1.1 Technology Roadmap for Semiconductors and Introduction of High-k Materials

Semiconductor devices are the basis to support our comfortable lives. They are incorporated in not only personal computers but also so many products such as mobile phones [1], home electric appliances [2] and cars [3]. A card and a tag which contain the integrated circuit (IC), so called IC card and IC tag, respectively, have already be realized to practical use today.

These applications have been allowed by a development of fine fabrication and high-integration technologies. The bipolar transistor was invented by Shockley, Brattain and Bardeen in 1947 [4]. Since then, semiconductor devices have been used for the amplifying and switching device instead of vacuum tubes. Moreover, integration of device elements has been explosively enhanced since invention of IC by Kilby in 1958 [4], and it has allowed higher-speed, lower-cost and lower power consumption for devices. Consequently, the semiconductor industry has been one of key industries in many contries as well as Japan.

However, there is "walls" for a development of more high-integrated circuit in the present day. Among their "walls", it is the big issue that the thickness of the gate insulator of field-effect-transistor (FET) will become sub-nm order so that the leakage current through the gate by the direct tunneling effect will be not negligible and the reliability of devices will decrease by diffusion of boron atoms as the dopant. Consequently, it is studied that Materials which have higher dielectric constant(k) than SiO_2 ($k = 3.9$), which called high-k materials, will be employed for the gate insulator instead of SiO_2, to increase the gate thickness as keeping the same gate capacitance. Figure 1.1 shows trends of the gate leakage current density limit and simulated gate leakage due to direct tunneling current for (a) low standby power (LSTP), (b) low operating power (LOP) and (c) high-performance (HP) logic technologies, shown in the International Technology Roadmap for

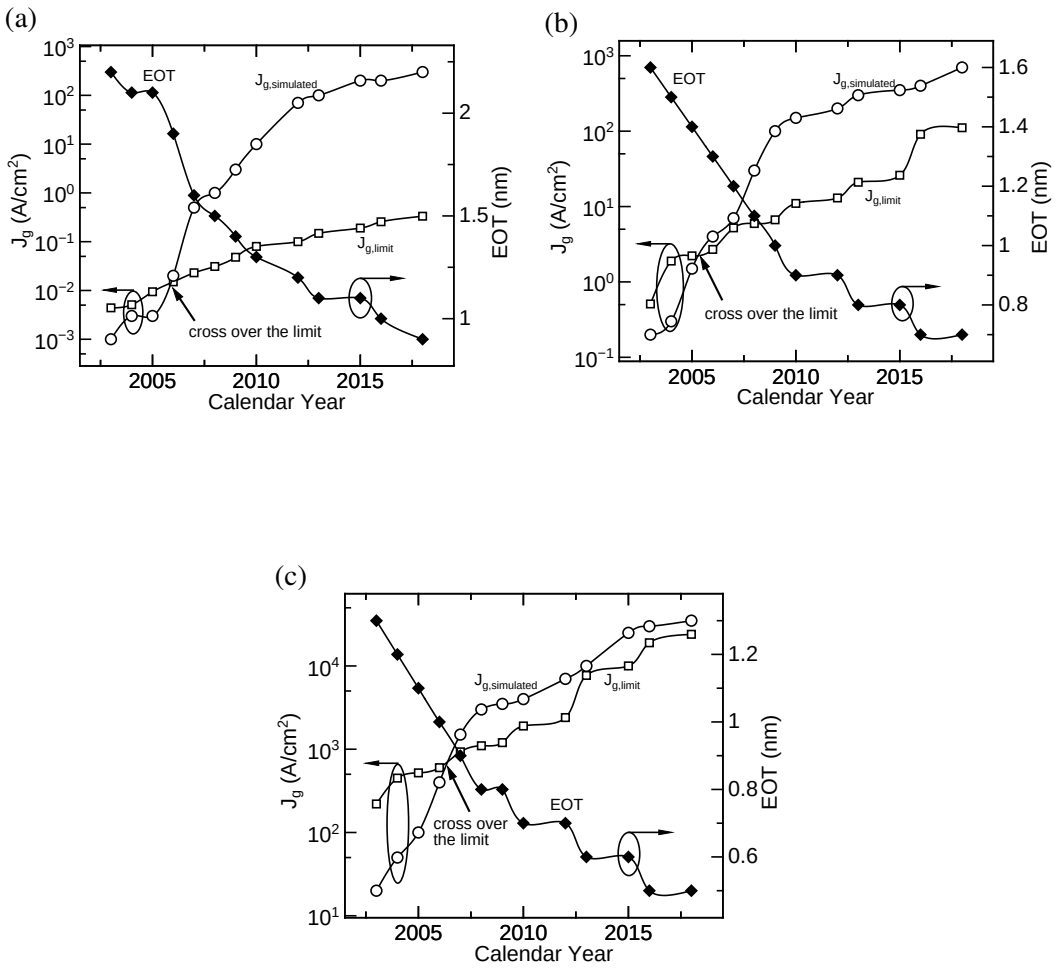

Figure 1.1: Gate leakage current density limit and simulated gate leakage due to direct tunneling for (a) LSTP, (b) LOP and (c) HP logic technologies [5].

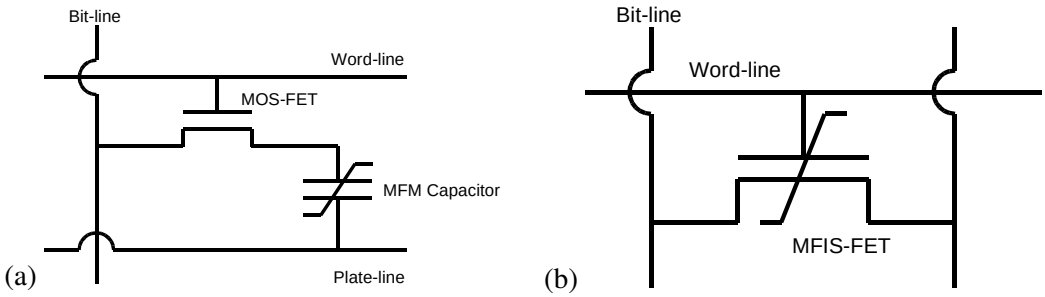

Figure 1.2: Device structure of FeRAMs, (a) 1T/1C type, (b) 1T type [14].

Semiconductors (ITRS) 2003 [5]. The direct tunneling current will cross over the leakage current limit in 2006 for LSTP or LOP and in 2007 for HP logic technology. Thus, introduction of high-k material is the pressing issue for the semiconductor industry. For high-k gate oxide material, ZrO_2 [6, 7], HfO_2 [8, 9], and lanthanoid oxides [7, 10, 11] have been investigated because of their stability to silicon substrate and high permittivity. In particular, HfO_2 and and their silicates [12] or aluminates are promised for gate oxides.

However, the high-k material is heterogeneous with silicon and must be physically deposited on the substrate so that it has various difficulties compared with SiO_2. Firstly, the interfacial layer between high-k dielectric film and silicon substrate is grown by chemical reaction and it has lower dielectric constant. Secondly, its barrier height toward carriers is usually lower than SiO_2. Moreover, it has more fixed charge and interface states. Thirdly, it has small thermal-stability so that it crystallize during high-temperature processes. Studies in search for an solution of these difficulties are performed around the world.

1.1.2 Ferroelectric Random Access Memory

As described above, a development of finer fabrication and high-integration technologies is approaching physical limits. Therefore, novel devices will be needed in the future instead of complementary metal-oxide-semiconductor (CMOS) devices. It is mentioned in ITRS2003 [5] that post-CMOS devices must be addressed.

The ferroelectric random access memory (FeRAM) has been expected as a memory device instead of the dynamic random access memory (DRAM). Ferroelectrics have permanent dipole moments and a polarization that is not necessarily zero when there is no electric field [13]. The direction of a polarization can be controlled by external electric field. It can be applied to a non-volatile memory by corresponding direction of a polarization to an binary information which is “0” or “1”, because directed polarization is hold until applying electric field again. FeRAM is classified in two types [14]. One is an one transistor and one capacitor (1T/1C) type, which is like DRAM structure, as shown Fig. 1.2 (b). Although it has already been partly-put to practical use, scalability is similar to DRAM. Additionally, data is destructed when it is read out, similar

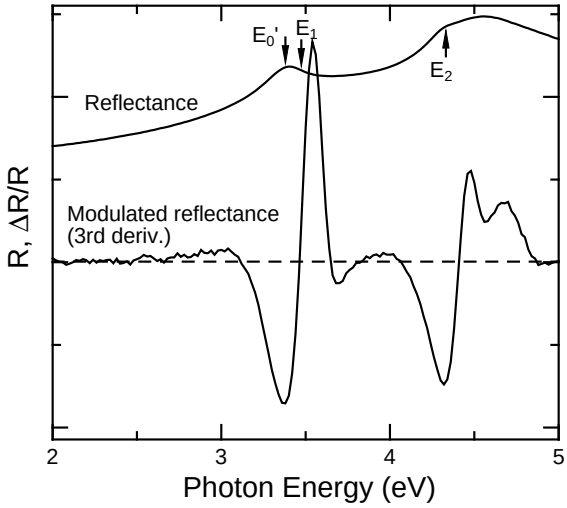

Figure 1.3: Reflectance and electrically modulated reflectance spectra of Si.

to DRAM. Second one is metal-ferroelectric-insulator-semiconductor (MFIS) -FET (1T) type, as shown in Fig. 1.2 (a). It has no capacitor so that it have much scalability. Moreover, data can be read out without destruction (non-destructive read-out). However, the retention time of MFIS-FET memory becomes degraded according to some factors such as leakage current and the relaxation of ferroelectric polarization [15]. Characteristics of MFIS structure such as the retention time is closely related to properties of silicon surface. Therefore, characterization of properties of the silicon surface in MFIS structure is very important.

1.1.3 Modulation Spectroscopy and Photoreflectance Spectroscopy

Spectra of optical constants such as the absorption coefficient and reflectivity are required to investigate an electronic energy band structure of the solid material. These spectra are closely related to electron transitions excited by the external light so that the band edges of an energy band structure can be decided by analysis of them. For actual measurements, however, the spectrum includes information from many transitions so that the energy band structure are hardly analyzed under various circumstances.

Photoreflectance spectroscopy (PRS) is one of measurement methods called modulation spectroscopy. Modulation spectroscopy is measurement method of change of the optical spectrum modulated by external perturbation. Since this change is a differential form of the spectrum without perturbation, a spectrum which has emphatic change at band edges is obtained. Electric field (electro-optical effect), temperature (thermo-optical effect), pressure (piezo-optical effect) and wavelength are employed for the external perturbation. In the case of PRS, electric field is induced at the semiconductor surface by carrier generated by irradiation of the modulation light and

electro-optical effect induced by the electric field is used for the perturbation. Figure 1.3 shows the comparison between non-modulated and modulated reflectance spectrum of Si. The critical points (E_0', E_1 and E_2) are unclear in non-modulated (conventional) reflectance so that their transition energies at critical points are hardly obtained. On the other hand, the peaks clearly appear at the critical points in the modulated spectrum.

Electro-optical effect was theoretically found as Franz-Keldysh effect, which absorption coefficient is changed by electric field, calculated by Franz [17] and Keldysh [18] in 1958, independently. Early experimental data of electro-optical effect were reported in subsequent years and its theorem was extended by Tharmalingam [19] in 1963. The first experimental result of PRS was reported by Wang et al [20] in 1967. Gay and Klauder proposed that the photoreflectance effect is due to a change in the effective density of states produced by the photoexcited carriers [21], but this was denied by experimental data reported by Nahory and Shay, and they concluded the photoreflectance arises from modulation of the built-in surface field as electroreflectance [22]. Aspnes showed that a modulated spectrum with a low electric field is third order derivative form of the spectrum without a electric field [23], which can make easier analysis. Since then, PRS has been applied to a number of compound semiconductors such as GaAs [24–26]. However, in spite of its availability, there are less applications to Si because of less modulation by less amount of photo-generated carrier.

1.2 Purpose of This Work

As described in the previous section, the introduction of high-k films or ferroelectric films in FET has captured the attention in recent years. It is considered that investigation of characteristics of silicon surface under these films is very important for future devices. In this work, various dielectric materials, deposition conditions and processes have been evaluated by investigation of the energy band structure at silicon surface by mainly PRS. It has not been studied that PRS is applied to characterization of these dielectric thin films. Particularly, it is noticed that energy-shift of PRS spectrum and PRS spectral intensity correspond to Si surface stress and Si surface potential, respectively. The targeted dielectric materials are SiO_2, high-k dielectrics (HfO_2, PrO_x, etc.) and ferroelectrics ($SrBi_2Ta_2O_9$). Si surface under these thin films is examined non-destructively and contactless with making full use of features of PRS. Conclusively, establishment of PRS as characterization tool of Si is aimed.

This work is organized into 6 chapters. The theories and the experimental method of PRS has been described in Chap. 2. The quantitative characterization of Si surface stress by PRS is described in Chap. 3. Thermally- or natively-grown SiO_2/Si structure is also discussed in Chap. 3. The deposition and annealing conditions of high-k films (high-k material: HfO_2, PrO_x, ZrO_2, Al_2O_3 and La_2O_3) are characterized and discussed in Chap. 4. Then in Chap. 5, the hysteresis

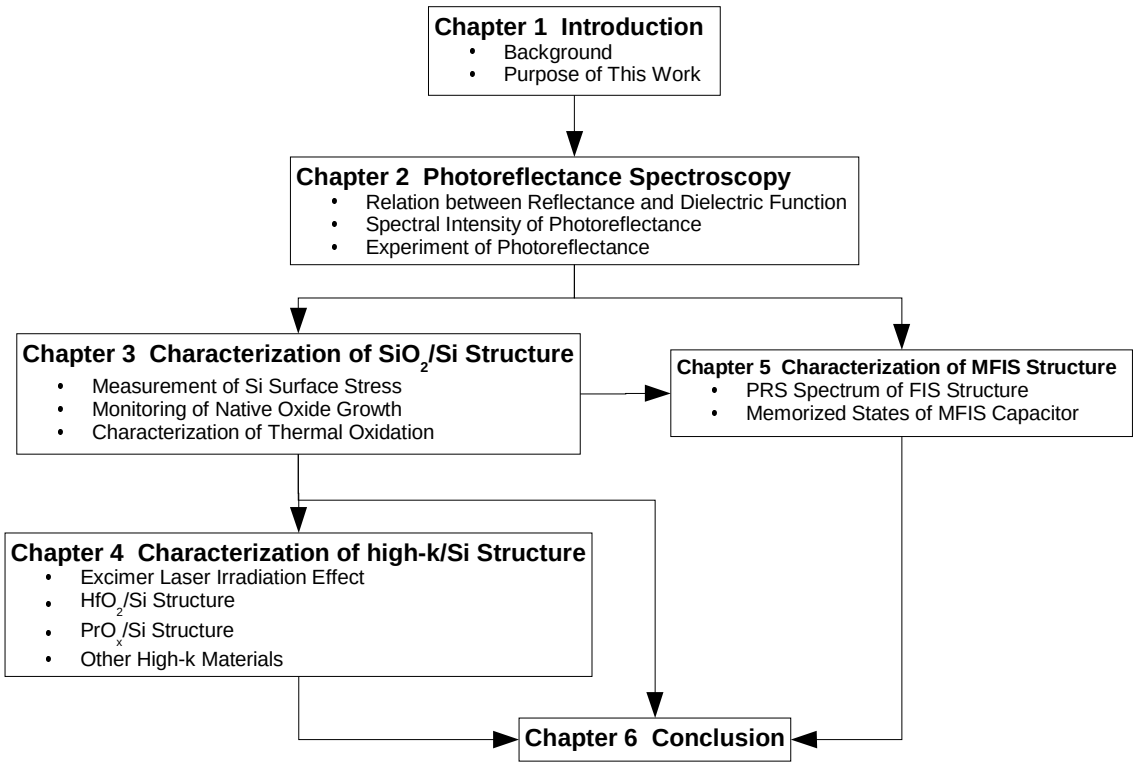

Figure 1.4: Logical organization of this thesis.

and retention properties of MFIS structures are characterized by PRS. Finally, the results from these studies are concluded in Chap. 6. The organization of this thesis is shown in Fig. 1.4.

Reference

[1] T. Miyake: Nikkei Microdevices **226** (2004) 30 [in Japanese].

[2] N. Ikeda: Keizai Sangyo Journal **394** (2004) 44 [in Japanese].

[3] T. Miyake: Nikkei Microdevices **217** (2003) 32 [in Japanese].

[4] H. Yanai and M. Nagata: *Shuseki Kairo Kougaku (1)* (Integrated Electronics), (Corona, Tokyo, 1987) 2nd ed., p. 1–7 [in Japanese].

[5] *The International Roadmap for Semiconductors*, Semiconductor Industry Association (2003).

[6] M. Sohgawa, S. Kitai, H. Kanda, T. Kanashima, A. Fujimoto and M. Okuyama: *Ext. Abstr. Int. Workshop Gate Insulator* (Business Center for Academic Societies Japan, Tokyo, 2001) p. 170.

[7] T. Kanashima, M. Sohgawa, H. Kanda, K. Ikeda and M. Okuyama: J. Kor. Phys. Soc. **42** (2003) S1357.

[8] M. Cho, H. B. Park, J. Park, C. S. Hwang, J. C. Lee, S. J. Oh, J. Jeong, K. S. Hyun, H. S. Kang, Y. W. Kim and J. H. Lee: J. Appl. Phys. **94** (2003) 2563.

[9] T. Kanashima, K. Ikeda, T. Tada, M. Sohgawa and M. Okuyama: to be published in J. Korean Phys. Soc.

[10] A. Fissel, J. Dąbrowski and H. J. Osten: J. Appl. Phys. **91** (2002) 8986.

[11] S. Kitai, O. Maida, T. Kanashima and M. Okuyama: Jpn. J. Appl. Phys. **42** (2003) 247.

[12] M. R. Visokay, J. J. Chambers, A. L. P. Rotondaro, A. Shanware and L. Colombo: Appl. Phys. Lett. **80** (2002) 3183.

[13] L. Solymar and D. Walsh: *Lectures on the Electrical Properties of Materials*, (Oxford University Press, Oxford, 1993) 5th ed., Chap. 10, p. 290.

[14] *Kyoyuudentai-Memory-no-Shintenkai* (Recent Progress in Ferroelectric Memories), ed. H. Ishiwara (CMC Books, Tokyo, 2004) p. 1–2 [in Japanese].

[15] M. Noda, K. Kodama, I. Ikeuchi, M. Takahashi and M. Okuyama: Jpn. J. Appl. Phys. **42** (2003) 2055.

[16] Y. Hamakawa: Bussei **7** (1966) 655 [in Japanese].

[17] W. Franz: Z. Naturforsch **130** (1958) 484.

[18] L. V. Keldysh: Soviet Physics JETP **34** (1958) 788.

[19] K. Tharmalingam: Phys. Rev. **130** (1963) 2204.

[20] E. Y. Wang and W. A. Albers, Jr: Phys. Lett. A **27** (1968) 347.

[21] J. G. Gay and L. T. Klauder, Jr.: Phys. Rev. **172** (1968) 811.

[22] R. E. Nahory and J. L. Shay: Phys. Rev. Lett. **21** (1968) 1569.

[23] D. E. Aspnes: Surf. Sci. **37** (1973) 418.

[24] T. Kanata, M. Matsunaga, H. Takakura and Y. Hamakawa: J. Appl. Phys. **68** (1990) 5309.

[25] N. Kallergi, B. Roughani, J. Aubel and S. Sundaram: J. Appl. Phys. **68** (1990) 4656.

[26] T. J. C. Hosea, P. J. Hughes and B. L. Weiss: J. Appl. Phys. **77** (1995) 2672.

Chapter 2

Photoreflectance Spectroscopy

2.1 Introduction

As described in Chap. 1, the study of modulation spectroscopy has a long history, and its theory has been already developed. However, in the case of PRS, it should be taken into account that the spectrum is affected by the surface potential of semiconductor, power and frequency of modulation light, the thickness and dielectric constant of the film and interference of probe light in the film. In this chapter, theories including these effects in addition to known theory are described. Moreover, actual PRS experiment in this work is also described.

2.2 Franz-Keldysh Effect

Schrödinger equation in relative coordinate system for electron-hole pair including the term of the static electric field ($\mathcal{E} = \left[\mathcal{E}_x, \mathcal{E}_y, \mathcal{E}_z\right]$) in the case of neglecting Coulomb interaction is expressed as following equation [1],

$$\left[-\frac{\hbar^2}{2\mu}\nabla^2 - q\mathcal{E}\cdot\mathbf{r}\right]\phi(\mathbf{r}) = E\phi(\mathbf{r}), \tag{2.1}$$

where μ is a reduced effective mass tensor and E is a energy eigenvalue, respectively. Using components of vectors ($\mathbf{r} = [x, y, z]$, $\nabla = \left[\frac{d^2}{dx^2}\frac{d^2}{dy^2}, \frac{d^2}{dz^2}\right]$), eq. (2.1) is expressed as a following equation,

$$\left[-\frac{\hbar^2}{2\mu_x}\frac{d^2}{dx^2} - \frac{\hbar^2}{2\mu_y}\frac{d^2}{dy^2} - \frac{\hbar^2}{2\mu_z}\frac{d^2}{dz^2} - q\left(\mathcal{E}_x x + \mathcal{E}_y y + \mathcal{E}_z z\right)\right]\phi(x,y,z) = E\phi(x,y,z), \tag{2.2}$$

where μ_i ($i = x, y, z$) are values of the principal direction of the reduced effective mass tensor. $\phi(\mathbf{r})$ can be separated $\phi(x)\,\phi(y)\,\phi(z)$, and each of them is satisfied a following equation,

$$\left[-\frac{\hbar^2}{2\mu_i}\frac{d^2}{dr_i^2} - q\mathcal{E}_i r_i - E_i\right]\phi(r_i) = 0, \tag{2.3}$$

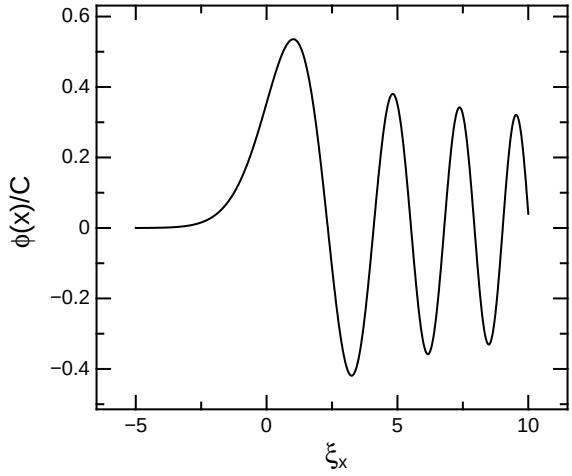

Figure 2.1: Calculated wave function ($\phi(x)$) of electron-hole pair under static electric field ($\mathcal{E}_x$).

$$E = E_x + E_y + E_z. \tag{2.4}$$

To solve this differential equation, a following variable transformation is performed,

$$\hbar\theta_i = \left(\frac{q^2\mathcal{E}_i^2\hbar^2}{2\mu_i}\right)^{\frac{1}{3}}, \tag{2.5}$$

$$\xi_i = \frac{E_i + q\mathcal{E}_i r_i}{\hbar\theta_i}. \tag{2.6}$$

Then eq. (2.3) is transformed into a following equation,

$$\frac{d^2}{d\xi_i^2}\phi(\xi_i) = -\xi_i\phi(\xi_i). \tag{2.7}$$

The solution of eq. (2.7) is given by using Airy function [2].

$$\phi(\xi_i) = C_i \mathrm{Ai}(-\xi_i), \tag{2.8}$$

where $\mathrm{Ai}(z)$ is defined as,

$$\mathrm{Ai}(z) = \frac{1}{\pi}\int_0^\infty \cos\left(\frac{1}{3}s^3 + sx\right)ds. \tag{2.9}$$

And C_i is a normalization constant of $\phi(\xi)$,

$$C_i = \frac{\sqrt{q|\mathcal{E}_i|}}{\hbar\theta}. \tag{2.10}$$

Therefore, $\phi(x, y, z)$ is expressed by a following equation,

$$\phi(x, y, z) = C_x C_y C_z \mathrm{Ai}(-\xi_x)\,\mathrm{Ai}\left(-\xi_y\right)\mathrm{Ai}(-\xi_z). \tag{2.11}$$

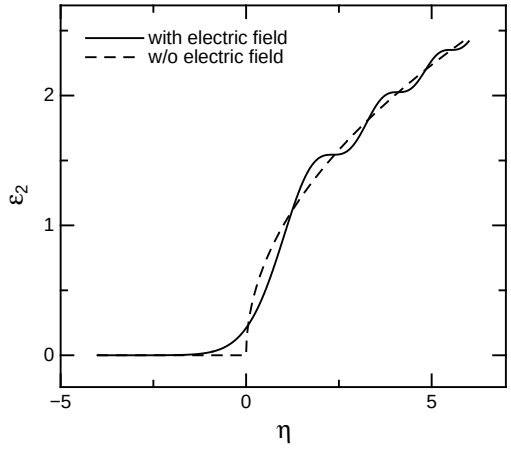

Figure 2.2: Calculated ε_2 with and without electric field vs. $\eta = \frac{E-E_g}{\hbar\theta}$ near the M_0 critical point.

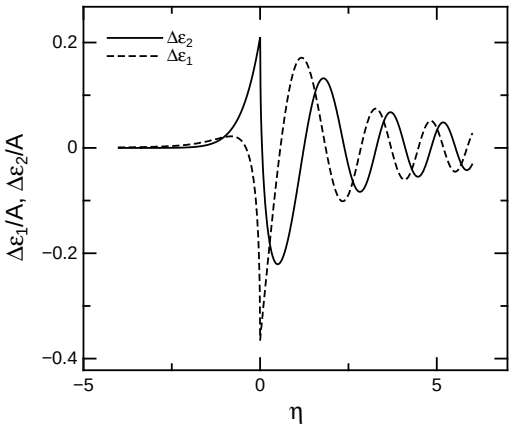

Figure 2.3: Calculated $\Delta\varepsilon_1$ and $\Delta\varepsilon_2$ for electric field modulation vs. $\eta = \frac{E-E_g}{\hbar\theta}$ near the M_0 critical point.

Figure 2.1 shows a wave function (normalized by C_i) calculated from eq. (2.11) when $\mathcal{E} = [\mathcal{E}_x, 0, 0]$, $k_y = k_z = 0$ and $E = 0$. The wave function penetrates the area of $x < 0$ ($\xi_x < 0$) so that optical transition becomes possible for the photon which has energy less than bandgap energy.

The imaginary part of the dielectric function $\varepsilon_2(E, \mathcal{E})$ at the M_0 critical point with the electric field is expressed as a following equation [1],

$$\varepsilon_2(E, \mathcal{E}) = A\pi\left[\mathrm{Ai}'^2(-\eta) + \eta\mathrm{Ai}^2(-\eta)\right], \tag{2.12}$$

where

$$\eta = \frac{E - E_g}{\hbar\theta} \tag{2.13}$$

$$\theta = \left(\theta_x\theta_y\theta_z\right)^{\frac{1}{3}}. \tag{2.14}$$

And the imaginary part of the dielectric function without field ($\varepsilon_2(E, 0)$)

$$\varepsilon_2(E, 0) = A\frac{\sqrt{E - E_g}}{\left|\sqrt{\hbar\theta}\right|}, \tag{2.15}$$

where

$$A = \frac{q^2}{2\pi m^2\omega^2}\left|\mathbf{e}\cdot\mathbf{p}\right|^2\sqrt{\frac{8\left|\mu_x\mu_y\mu_z\right|}{\hbar^6}}\left|\sqrt{\hbar\theta}\right|, \tag{2.16}$$

and $|\mathbf{e}\cdot\mathbf{p}|$ is the matrix element of momentum. Figure 2.2 shows the imaginary part of dielectric function calculated for the M_0 critical point with and without electric field. The difference $\Delta\varepsilon_2(E, \mathcal{E})$ is obtained as

$$\Delta\varepsilon_2(E, \mathcal{E}) = \varepsilon_2(E, \mathcal{E}) - \varepsilon_2(E, 0)$$

$$
\begin{aligned}
&= A\left\{\pi\left[\mathrm{Ai}'^{2}(-\eta)+\eta\mathrm{Ai}^{2}(-\eta)\right]-\frac{\sqrt{E-E_g}}{\left|\sqrt{\hbar\theta}\right|}\right\} \\
&= A\left\{\pi\left[\mathrm{Ai}'^{2}(-\eta)+\eta\mathrm{Ai}^{2}(-\eta)\right]-u(\eta)\ \sqrt{\eta}\right\} \\
&\equiv AF(-\eta) \qquad (2.17)\\
F(-\eta) &= \pi\left[\mathrm{Ai}'^{2}(-\eta)+\eta\mathrm{Ai}^{2}(-\eta)\right]-u(\eta)\ \sqrt{\eta}. \qquad (2.18)
\end{aligned}
$$

The real part of the dielectric function is obtained by the Kramers-Kronig transformation as

$$
\begin{aligned}
\Delta\varepsilon_2(E,\mathcal{E}) &= AG(-\eta), \qquad (2.19)\\
G(-\eta) &= \pi\left[\mathrm{Ai}'(-\eta)\,\mathrm{Bi}'(-\eta)+\eta\mathrm{Ai}(-\eta)\,\mathrm{Bi}(-\eta)\right] \\
&\quad +u(\eta)\ \sqrt{-\eta}. \qquad (2.20)
\end{aligned}
$$

Figure 2.3 shows calculated dielectric function from eqs. (2.17) and (2.19) for the M_0 critical point. The difference becomes maximum value at critical point energy ($\eta = 0$). The oscillation appears at photon energy over critical point ($\eta > 0$). This oscillation is called Franz-Keldysh oscillation.

2.3 Third Derivative Theory

Under low electric field, the difference of dielectric function becomes a simple shape instead of the Franz-Keldysh oscillation. It was found by Aspnes that its shape is similar to third derivative of dielectric function, so its theory is called Aspnes's third derivative theory [1].

The dielectric functions for single critical point E_g which is 1, 2 or 3 dimensional simple parabolic band are expressed as following equations considering broadening (broadening factor: Γ) [9],

$$\varepsilon(E,\Gamma)_{1D} = \frac{Q}{E^2} D_x K_y K_z i^{l+1} \left(E - E_g + i\Gamma\right)^{-\frac{1}{2}} \tag{2.21}$$

$$\varepsilon(E,\Gamma)_{2D} = \frac{Q}{E^2} D_x D_y K_z i^{l+2} \ln\left(E - E_g + i\Gamma\right) \tag{2.22}$$

$$\varepsilon(E,\Gamma)_{3D} = \frac{2\pi Q}{E^2} D_x D_y D_z i^{l+1} \left(E - E_g + i\Gamma\right)^{\frac{1}{2}}, \tag{2.23}$$

where

$$Q = \frac{q^2\hbar^2}{\pi m^2} |\mathbf{e}\cdot\mathbf{p}| \tag{2.24}$$

$$D_j = \sqrt{\frac{2\left|\mu_{jj}\right|}{\hbar^2}}, \quad j = x, y, z, \tag{2.25}$$

$K_j = K_y$ or K_z are the cutoff lengths in the Brillouin zone for 1 and 2 dimensional critical points, and l shows the critical point type which is equal to the number of negative masses μ_{jj}. These equations are shown as the generic form,

$$\varepsilon(E,\Gamma) = A\Gamma^{-k} e^{i\theta} \left(E - E_g + i\Gamma\right)^k, \tag{2.26}$$

k depends upon the dimension of the critical point, is $-\frac{1}{2}$ for 1D, 0 (logarithmic) for 2D and $\frac{1}{2}$ for 3D.

When the electric field is enough low, the difference of dielectric function with electric field is the third derivative of dielectric function without electric field [23],

$$\Delta\varepsilon(E,\Gamma,\mathcal{E}) \propto \frac{\mathcal{E}^2}{E^2} \frac{\partial^3}{\partial E^3} E^2 \varepsilon(E,\Gamma) \tag{2.27}$$

Substituting (2.26) to (2.27), we obtain

$$\begin{aligned} \Delta\varepsilon(E,\Gamma,\mathcal{E}) &= B\mathcal{E}^2 e^{i\theta} \left(E - E_g + i\Gamma\right)^{k-3} \\ &= C e^{i\theta} \left(E - E_g + i\Gamma\right)^{-n}, \end{aligned} \tag{2.28}$$

where B and C are constants and $n = -(k-3)$ depends upon dimension of the critical point, is $\frac{7}{2}$ for 1D, 3 (logarithmic) for 2D and $\frac{5}{2}$ for 3D.

Figure 2.4 shows the imaginary part of dielectric function calculated by eq. (2.26) and its difference calculated by eq. (2.28) for 3D M_0 critical point. A simple spectrum mainly composed of two plus and minus peak is observed.

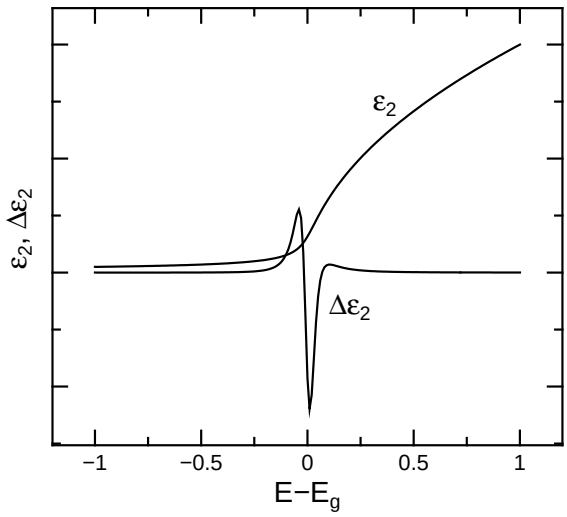

Figure 2.4: Imaginary part of dielectric function calculated by eq. (2.26) and its difference calculated by (2.28) for 3D M_0 critical point.

2.4 Relation between Reflectance and Dielectric Function

2.4.1 Normal Incidence

When the light enters from a transparent medium **I** (refractive index: $n_{\mathrm{I}} = n_a$) to a medium **II** (complex refractive index: $n_{\mathrm{II}} = n^* = n + ik$) as shown in Fig. 2.5, the complex reflectivity, r^* and reflectance, R is expressed as a following equation [3],

$$r^* = \frac{n_{\mathrm{II}} - n_{\mathrm{I}}}{n_{\mathrm{II}} + n_{\mathrm{I}}} = \frac{n^* - n_a}{n^* + n_a} \tag{2.29}$$

$$R = \left|r^*\right|^2 = \left|\frac{n^* - n_a}{n^* + n_a}\right|^2 = \frac{|n^* - n_a|^2}{|n^* + n_a|^2} = \frac{(n - n_a)^2 + k^2}{(n + n_a)^2 + k^2}. \tag{2.30}$$

There are generally relationships between the complex refractive index and the relative complex dielectric constant, $\varepsilon^* = \varepsilon_1 + i\varepsilon_2$ (permability μ equal to vacuum permability μ_0 at any time) [3],

$$n^* = \sqrt{\varepsilon^*}. \tag{2.31}$$

Substituting the refraction index of medium **II** to eq. (2.31),

$$\begin{aligned} \varepsilon_1 + i\varepsilon_2 &= (n + ik)^2 \\ &= n^2 - k^2 + 2ink. \end{aligned} \tag{2.32}$$

Since the real and imaginary parts of both sides must equal, following relationships are obtained.

$$\varepsilon_1 = n^2 - k^2 \tag{2.33}$$

$$\varepsilon_2 = 2nk \tag{2.34}$$

$$n = \sqrt{\frac{\varepsilon_1 + \sqrt{{\varepsilon_1}^2 + {\varepsilon_2}^2}}{2}} \tag{2.35}$$

$$k = \sqrt{\frac{-\varepsilon_1 + \sqrt{{\varepsilon_1}^2 + {\varepsilon_2}^2}}{2}}. \tag{2.36}$$

As described in § 2.2, the dielectric constant is varied by the electro-optical effect, so the reflectance change ΔR may be obtained as a total differential of R by using dielectric constants of all media. The total differential of eq. (2.30) is expressed as a following equation,

$$\Delta R = \frac{\partial R}{\partial \varepsilon_1}\Delta\varepsilon_1 + \frac{\partial R}{\partial \varepsilon_2}\Delta\varepsilon_2 + \frac{\partial R}{\partial \varepsilon_a}\Delta\varepsilon_a \tag{2.37}$$

Assuming that the medium **I** is affected by the perturbation, $\Delta\varepsilon_a$ is negligible. Thus, the third term of eq. (2.37) equal to zero, so that ΔR can be expressed by an easy form,

$$\Delta R = \frac{\partial R}{\partial \varepsilon_1}\Delta\varepsilon_1 + \frac{\partial R}{\partial \varepsilon_2}\Delta\varepsilon_2. \tag{2.38}$$

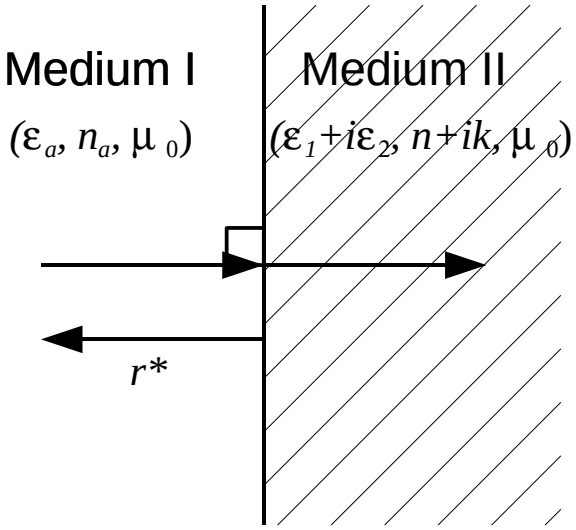

Figure 2.5: An illustration of incident light near interface between a medium **I** and a medium **II**.

Therefore, the ratio of reflectance difference to reflectance, $\frac{\Delta R}{R}$ is expressed by a following equation,

$$\begin{aligned}\frac{\Delta R}{R} &= \frac{1}{R}\frac{\partial R}{\partial \varepsilon_1}\Delta\varepsilon_1 + \frac{1}{R}\frac{\partial R}{\partial \varepsilon_2}\Delta\varepsilon_2 \\ &= \alpha(\varepsilon_1,\varepsilon_2)\,\Delta\varepsilon_1 + \beta(\varepsilon_1,\varepsilon_2)\,\Delta\varepsilon_2. \end{aligned} \tag{2.39}$$

where $\alpha(\varepsilon_1,\varepsilon_2)$ and $\beta(\varepsilon_1,\varepsilon_2)$ are called the Seraphin coefficients [4], expressed as following functions,

$$\alpha(\varepsilon_1,\varepsilon_2) = \frac{1}{R}\frac{\partial R}{\partial \varepsilon_1} = \frac{2\gamma}{\gamma^2+\delta^2} \tag{2.40}$$

$$\beta(\varepsilon_1,\varepsilon_2) = \frac{1}{R}\frac{\partial R}{\partial \varepsilon_2} = \frac{2\delta}{\gamma^2+\delta^2}, \tag{2.41}$$

where,

$$\gamma = \frac{n}{n_a}\left(n^2-3k^2-n_a^2\right) \tag{2.42}$$

$$\delta = \frac{k}{n_a}\left(3n^2-k^2-n_a^2\right). \tag{2.43}$$

Figure 2.6 shows Seraphin coefficients α and β of Si calculated by eqs. (2.40) and (2.41) by using reported complex refractive index [5]. The Seraphin coefficients give a relationship between the reflectance and the dielectric function.

2.4.2 Oblique Incidence

Now, the reflection in the case of oblique incidence is discussed. Figure 2.7 shows a model of oblique incidence with incident angle θ_i and refraction angle θ_t^* (a complex number, $\theta_t^* = \theta_{t1}+i\theta_{t2}$).

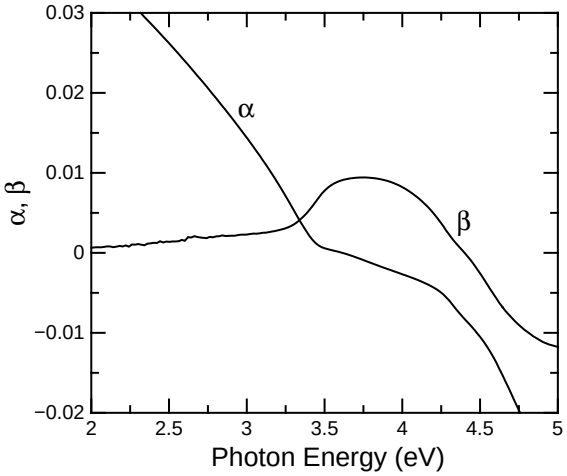

Figure 2.6: Calculated Seraphin coefficients of Si, α and β as a function of photon energy. n and k value reported in ref. [5], and $n_a = 1$ are used for calculation.

The reflectivities, r_s^* for s-polarized light and r_p^* for p-polarized light are expressed as following equations, respectively [3],

$$\begin{aligned} r_s^* &= \frac{n_{\mathrm{I}} \cos\theta_i - n_{\mathrm{II}} \cos\theta_t^*}{n_{\mathrm{I}} \cos\theta_i + n_{\mathrm{II}} \cos\theta_t^*} \\ &= \frac{n_a \cos\theta_i - (n+ik) \cos\theta_t^*}{n_a \cos\theta_i + (n+ik) \cos\theta_t^*} \end{aligned} \tag{2.44}$$

$$\begin{aligned} r_p^* &= \frac{n_{\mathrm{II}} \cos\theta_i - n_{\mathrm{I}} \cos\theta_t}{n_{\mathrm{II}} \cos\theta_i + n_{\mathrm{I}} \cos\theta_t^*} \\ &= \frac{(n+ik) \cos\theta_i - n_a \cos\theta_t^*}{(n+ik) \cos\theta_i + n_a \cos\theta_t^*}. \end{aligned} \tag{2.45}$$

There is a following relationship from Snell's low,

$$n_a \sin\theta_i = (n+ik) \sin\theta_t^*. \tag{2.46}$$

Therefore,

$$(n+ik) \cos\theta_t^* = (n+ik) \sqrt{1 - \sin^2\theta_t^*} = \sqrt{(n+ik)^2 - \sin^2\theta_i}. \tag{2.47}$$

Substituting eq. (2.47) to eqs (2.44) and (2.45), we obtain

$$r_s^* = \frac{n_a \cos\theta_i - \sqrt{(n+ik)^2 - \sin^2\theta_i}}{n_a \cos\theta_i + \sqrt{(n+ik)^2 - \sin^2\theta_i}} \tag{2.48}$$

$$r_p^* = \frac{(n+ik)^2 \cos\theta_i - n_a^2 \sqrt{(n+ik)^2 - \sin^2\theta_i}}{(n+ik)^2 \cos\theta_i + n_a^2 \sqrt{(n+ik)^2 - \sin^2\theta_i}}. \tag{2.49}$$

The reflectance R_j ($j = s$ and p for each polarized lights) is

$$\begin{aligned} R_j &= \left|r_j^*\right|^2 \\ &= \Re\left(r_j^*\right)^2 + \Im\left(r_j^*\right)^2. \end{aligned} \tag{2.50}$$

The Seraphin coefficients in eq. (2.39) are calculated as

$$\alpha_j(\varepsilon_1,\varepsilon_2) = \frac{1}{R_j}\frac{\partial R_j}{\partial \varepsilon_1} = 2\frac{\Re\left(r_j^*\frac{\partial r_j^*}{\partial \varepsilon_1}\right) + \Im\left(r_j^*\frac{\partial r_j^*}{\partial \varepsilon_1}\right)}{\Re\left(r_j^*\right)^2 + \Im\left(r_j^*\right)^2} \tag{2.51}$$

$$\beta_j(\varepsilon_1,\varepsilon_2) = \frac{1}{R_j}\frac{\partial R_j}{\partial \varepsilon_2} = 2\frac{\Re\left(r_j^*\frac{\partial r_j^*}{\partial \varepsilon_2}\right) + \Im\left(r_j^*\frac{\partial r_j^*}{\partial \varepsilon_2}\right)}{\Re\left(r_j^*\right)^2 + \Im\left(r_j^*\right)^2}. \tag{2.52}$$

The differential forms of reflectance are shown as following equations,

$$\begin{aligned} \frac{\partial r_s^*}{\partial \varepsilon_1} &= \frac{-n_a\cos\theta_i}{\sqrt{(n+ik)^2-\sin^2\theta_i}\left[n_a\cos\theta_i + \sqrt{(n+ik)^2-\sin^2\theta_i}\right]^2} \\ \frac{\partial r_s^*}{\partial \varepsilon_2} &= \frac{-in_a\cos\theta_i}{\sqrt{(n+ik)^2-\sin^2\theta_i}\left[n_a\cos\theta_i + \sqrt{(n+ik)^2-\sin^2\theta_i}\right]^2} \\ \frac{\partial r_p^*}{\partial \varepsilon_1} &= \frac{n_a\cos\theta_i\left[(n+ik)^2-2\sin^2\theta_i\right]}{\sqrt{(n+ik)^2-\sin^2\theta_i}\left[(n+ik)^2\cos\theta_i + n_a\sqrt{(n+ik)^2-\sin^2\theta_i}\right]^2} \\ \frac{\partial r_p^*}{\partial \varepsilon_2} &= \frac{in_a\cos\theta_i\left[(n+ik)^2-2\sin^2\theta_i\right]}{\sqrt{(n+ik)^2-\sin^2\theta_i}\left[(n+ik)^2\cos\theta_i + n_a\sqrt{(n+ik)^2-\sin^2\theta_i}\right]^2}. \end{aligned}$$

For unpolarized light, the reflectance R is [6]

$$R = \frac{1}{2}\left(R_s + R_p\right). \tag{2.53}$$

Thus, Seraphin coefficients are shown as following equations,

$$\alpha(\varepsilon_1,\varepsilon_2) = \frac{1}{R_s+R_p}\left(R_s\alpha_s + R_p\alpha_p\right) \tag{2.54}$$

$$\beta(\varepsilon_1,\varepsilon_2) = \frac{1}{R_s+R_p}\left(R_s\beta_s + R_p\beta_p\right). \tag{2.55}$$

The calculated α and β for unpolarized light are shown in Fig. 2.8. Obviously, the values for $\theta_i = 0^\circ$ (normal incident) are equal to that in Fig. 2.6. In the case of $\theta_i = 45^\circ$, it is exactly similar to that for $\theta_i = 0^\circ$ in this energy region. On the other hand, visible change is observed for $\theta_i = 75^\circ$.

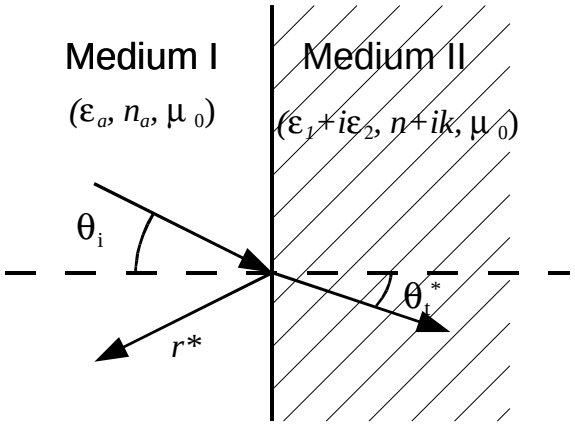

Figure 2.7: An illustration of obliquely-incident light near interface between a medium **I** and a medium **II**.

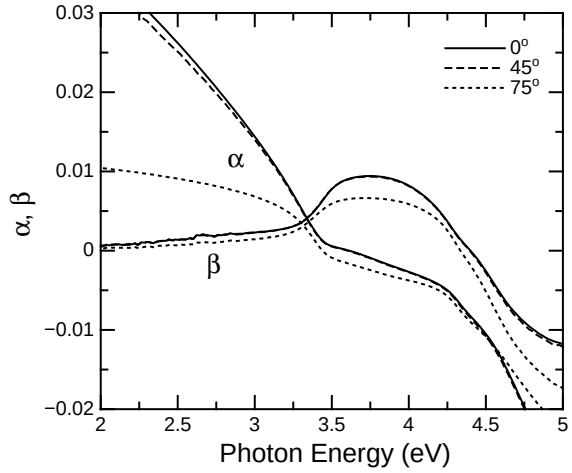

Figure 2.8: Calculated spectra of Seraphin coefficients, α and β, for 0°, 45° and 75°.

2.4.3 Incidence from Multiple Layers

In the case of incidence from thin (~wavelength) multiple layers which have different refractive indices, the optical interference must be considered.

a) 1 Layer

The reflectivity is expressed as a following equation in the case of incidence through 1 layer which have refractive index n_a as shown in Fig. 2.9 [7],

$$r^* = \frac{r_a + r_0^* e^{-i2\Delta_a}}{1 + r_a r_0^* e^{-i2\Delta_a}} \tag{2.56}$$

where

$$\Delta_a = \frac{2\pi d_a}{\lambda} n_a \cos\theta_a, \tag{2.57}$$

and λ is the wavelength of light, d_a is the thickness of layer a, respectively. From Snell's low,

$$\sin\theta_i = n_a \sin\theta_a = (n + ik)\sin\theta_t^*, \tag{2.58}$$

so there are the relation shown as following equations,

$$n_a \cos\theta_a = n_a \sqrt{1 - \sin^2\theta_a} = \sqrt{n_a^2 - \sin^2\theta_i} \tag{2.59}$$

$$(n + ik)\cos\theta_t^* = (n + ik)\sqrt{1 - \sin^2\theta_t^*} = \sqrt{(n + ik)^2 - \sin^2\theta_i} \tag{2.60}$$

r_{aj} and r_{0j}^* ($j = s$ or p) are the reflectivity at interface between the air and layer a and that between layer a and the substrate, respectively. These reflectivities are expressed as following equations,

$$\begin{aligned} r_{as} &= \frac{\cos\theta_i - n_a\cos\theta_a}{\cos\theta_i + n_a\cos\theta_a} \\ &= \frac{\cos\theta_i - \sqrt{n_a^2 - \sin^2\theta_i}}{\cos\theta_i + \sqrt{n_a^2 - \sin^2\theta_i}} \end{aligned} \tag{2.61}$$

$$\begin{aligned} r_{0s}^* &= \frac{n_a\cos\theta_a - (n + ik)\cos\theta_t^*}{n_a\cos\theta_a + (n + ik)\cos\theta_t^*} \\ &= \frac{\sqrt{n_a^2 - \sin^2\theta_i} - \sqrt{(n + ik)^2 - \sin^2\theta_i}}{\sqrt{n_a^2 - \sin^2\theta_i} + \sqrt{(n + ik)^2 - \sin^2\theta_i}} \end{aligned} \tag{2.62}$$

$$\begin{aligned} r_{ap} &= \frac{n_a\cos\theta_i - \cos\theta_a}{n_a\cos\theta_i + \cos\theta_a} \\ &= \frac{n_a^2\cos\theta_i - \sqrt{n_a^2 - \sin^2\theta_i}}{n_a^2\cos\theta_i + \sqrt{n_a^2 - \sin^2\theta_i}} \end{aligned} \tag{2.63}$$

$$r_{0p}^* = \frac{(n + ik)\cos\theta_a - n_a\cos\theta_t^*}{(n + ik)\cos\theta_a + n_a\cos\theta_t^*}$$

$$= \frac{(n+ik)^2\sqrt{n_a^2-\sin^2\theta_i}-n_a^2\sqrt{(n+ik)^2-\sin^2\theta_i}}{(n+ik)^2\sqrt{n_a^2-\sin^2\theta_i}+n_a^2\sqrt{(n+ik)^2-\sin^2\theta_i}} \tag{2.64}$$

The reflectance R_j is obtained by using eq. (2.56) as,

$$\begin{aligned} R_j &= \left|\frac{r_{aj}+r_{0j}^* e^{-i2\Delta_a}}{1+r_{aj}r_{0j}^* e^{-i2\Delta_a}}\right|^2 \\ &= \frac{\left|r_{aj}+r_{0j}^* e^{-i2\Delta_a}\right|^2}{\left|1+r_{aj}r_{0j}^* e^{-i2\Delta_a}\right|^2} \qquad (2.65) \\ &= \frac{\left[r_{aj}+\Re\left(r_{0j}^* e^{-i2\Delta_a}\right)\right]^2+\left[\Im\left(r_{0j}^* e^{-i2\Delta_a}\right)\right]^2}{\left[1+r_{aj}\Re\left(r_{0j}^* e^{-i2\Delta_a}\right)\right]^2+\left[r_{aj}\Im\left(r_{0j}^* e^{-i2\Delta_a}\right)\right]^2} \\ &= \frac{A_{1j}}{A_{2j}}, \qquad (2.66) \end{aligned}$$

where

$$A_{1j} = \left[r_{aj}+\Re\left(r_{0j}^* e^{-i2\Delta_a}\right)\right]^2+\left[\Im\left(r_{0j}^* e^{-i2\Delta_a}\right)\right]^2 \tag{2.67}$$

$$A_{2j} = \left[1+r_{aj}\Re\left(r_{0j}^* e^{-i2\Delta_a}\right)\right]^2+\left[r_{aj}\Im\left(r_{0j}^* e^{-i2\Delta_a}\right)\right]^2. \tag{2.68}$$

The Seraphin coefficient ($j = s, p$ and $k = 1, 2$) is shown as

$$\frac{1}{R_j}\frac{\partial R_j}{\partial \varepsilon_k} = \frac{\frac{\partial A_{1j}}{\partial \varepsilon_k}A_{2j}+A_{1j}\frac{\partial A_{2j}}{\varepsilon_k}}{A_{1j}A_{2j}}, \tag{2.69}$$

and the differentiations of involved equations are

$$\begin{aligned} \frac{\partial B_{1j}}{\partial \varepsilon_k} &= 2\Re\left(e^{-i2\Delta_a}\frac{\partial r_{0j}^*}{\partial \varepsilon_k}\right)\left[r_{aj}+\Re\left(r_{0j}^* e^{-i2\Delta_a}\right)\right] \\ &\quad +2\Im\left(e^{-i2\Delta_a}\frac{\partial r_{0j}^*}{\partial \varepsilon_k}\right)\Im\left(r_{0j}^* e^{-i2\Delta_a}\right) \\ \frac{\partial B_{2j}}{\partial \varepsilon_k} &= 2r_{aj}\Re\left(e^{-i2\Delta_a}\frac{\partial r_{0j}^*}{\partial \varepsilon_k}\right)\left[1+r_{aj}\Re\left(r_{0j}^* e^{-i2\Delta_a}\right)\right] \\ &\quad +2r_{aj}^2\Im\left(e^{-i2\Delta_a}\frac{\partial r_{0j}^*}{\partial \varepsilon_k}\right)\Im\left(r_{0j}^* e^{-i2\Delta_a}\right) \\ \frac{\partial r_{0s}^*}{\partial \varepsilon_1} &= \frac{-\sqrt{n_a^2-\sin^2\theta_i}}{\sqrt{(n+ik)^2-\sin^2\theta_i}} \\ &\quad \frac{1}{\left[\sqrt{n_a^2-\sin^2\theta_i}+\sqrt{(n+ik)^2-\sin^2\theta_i}\right]^2} \end{aligned} \tag{2.70}$$

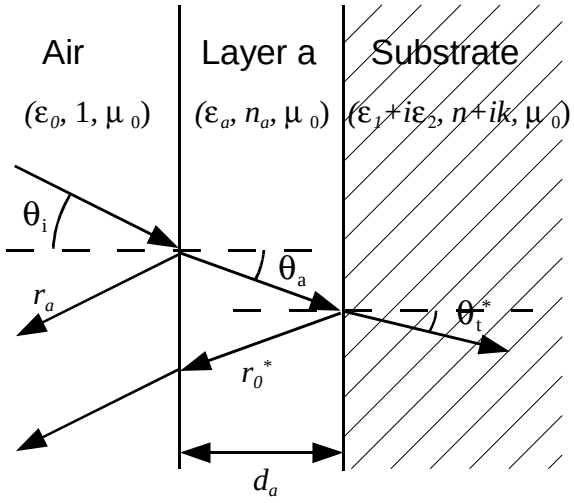

Figure 2.9: An illustration of obliquely-incident light near the region of layer stacked on a substrate.

$$\frac{\partial r_{0s}^*}{\partial \varepsilon_2} = \frac{-i\sqrt{n_a^2 - \sin^2\theta_i}}{\sqrt{(n+ik)^2 - \sin^2\theta_i}} \frac{1}{\left[\sqrt{n_a^2 - \sin^2\theta_i} + \sqrt{(n+ik)^2 - \sin^2\theta_i}\right]^2} \tag{2.71}$$

$$\frac{\partial r_{0p}^*}{\partial \varepsilon_1} = \frac{n_a^2\sqrt{n_a^2 - \sin^2\theta_i}}{\sqrt{(n+ik)^2 - \sin^2\theta_i}} \times \frac{\left[(n+ik)^2 - 2\sin^2\theta_i\right]}{\left[(n+ik)^2\sqrt{n_a^2 - \sin^2\theta_i} + n_a^2\sqrt{(n+ik)^2 - \sin^2\theta_i}\right]^2} \tag{2.72}$$

$$\frac{\partial r_{0s}^*}{\partial \varepsilon_2} = \frac{in_a^2\sqrt{n_a^2 - \sin^2\theta_i}}{\sqrt{(n+ik)^2 - \sin^2\theta_i}} \times \frac{\left[(n+ik)^2 - 2\sin^2\theta_i\right]}{\left[(n+ik)^2\sqrt{n_a^2 - \sin^2\theta_i} + n_a^2\sqrt{(n+ik)^2 - \sin^2\theta_i}\right]^2} \tag{2.73}$$

The Seraphin coefficients for unpolarized light can be calculated by using eqs. (2.54) and (2.55). Figures 2.10 and 2.11 show calculated Seraphin coefficients with and without film. The film thicknesses are 1, 10 and 100 nm for Fig. 2.10, and the dielectric constants of the films are 1.46 (proper for SiO_2), 1.8 and 2.2 for Fig. 2.11. The shape of Seraphin coefficient vertiginously

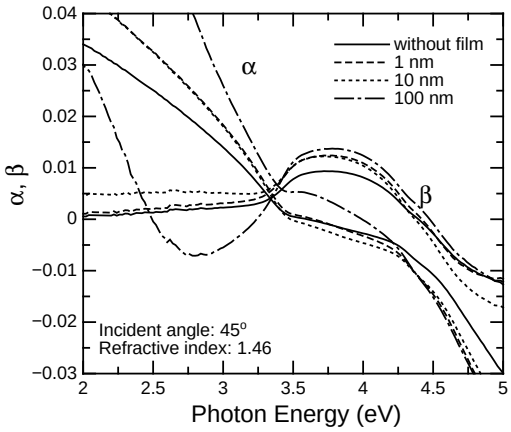

Figure 2.10: Calculated spectra of Seraphin coefficients of the structure without and with thin film, α and β for layer stacked on a substrate. The layer thicknesses are 1, 10 and 100 nm.

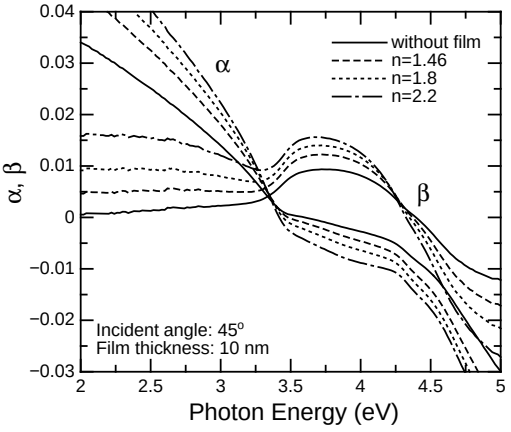

Figure 2.11: Calculated spectra of Seraphin coefficients of the structure without and with thin film for layer stacked on a substrate. The refractive indices of the layers are 1.46, 1.8 and 2.2.

varies with thickness and dielectric constant of the film. This suggests that the shape of modulation spectrum strongly correlate with thickness and material of the film.

b) 2 Layers

In the case of incidence through 2 layers as shown in Fig. 2.12, the reflectivity is expressed as a following equation [7],

$$r^* = \frac{r_b A + Be^{-i2\Delta_b}}{A + Br_b e^{-i2\Delta_b}} = \frac{C_1}{C_2}, \tag{2.74}$$

where

$$A = 1 + r_a r_0^* e^{-i2\Delta_a} \tag{2.75}$$

$$B = r_a + r_0^* e^{-i2\Delta_a} \tag{2.76}$$

$$C_1 = r_b A + Be^{-i2\Delta_b} \tag{2.77}$$

$$C_2 = A + Br_b e^{-i2\Delta_b} \tag{2.78}$$

$$\Delta_a = \frac{2\pi d_a}{\lambda} n_a \cos\theta_a \tag{2.79}$$

$$\Delta_b = \frac{2\pi d_b}{\lambda} n_b \cos\theta_b \tag{2.80}$$

The reflectance is expressed as

$$R = \left| \frac{r_b A + Be^{-i2\Delta_b}}{A + Br_b e^{-i2\Delta_b}} \right|^2 = \frac{|C_1|^2}{|C_2|^2}. \tag{2.81}$$

Thus, the Seraphin coefficients becomes

$$\frac{1}{R}\frac{\partial R}{\partial \varepsilon_k} = \frac{1}{|C_1|^2 |C_2|^2}\left[|C_2|^2 \frac{\partial |C_1|^2}{\partial \varepsilon_k} - |C_1|^2 \frac{\partial |C_2|^2}{\partial \varepsilon_k} \right], \tag{2.82}$$

where

$$\frac{\partial |C_l|^2}{\partial \varepsilon_k} = 2\Re(C_l)\,\Re\left(\frac{\partial C_l}{\partial \varepsilon_k}\right) + 2\Im(C_l)\,\Im\left(\frac{\partial C_l}{\partial \varepsilon_k}\right) \quad (l = 1, 2) \tag{2.83}$$

$$\begin{aligned} \frac{\partial C_1}{\partial \varepsilon_k} &= r_b \frac{\partial A}{\partial \varepsilon_k} + e^{-i2\Delta_b} \frac{\partial B}{\partial \varepsilon_k} \\ &= r_a r_b e^{-i2\Delta_a} \frac{\partial r_0^*}{\partial \varepsilon_k} + e^{-i2(\Delta_a + \Delta_b)} \frac{\partial r_0^*}{\partial \varepsilon_k} \end{aligned} \tag{2.84}$$

$$\begin{aligned} \frac{\partial C_2}{\partial \varepsilon_k} &= \frac{\partial A}{\partial \varepsilon_k} + r_b e^{-i2\Delta_b} \frac{\partial B}{\partial \varepsilon_k} \\ &= r_a e^{-i2\Delta_a} \frac{\partial r_0^*}{\partial \varepsilon_k} + r_b e^{-i2(\Delta_a + \Delta_b)} \frac{\partial r_0^*}{\partial \varepsilon_k}. \end{aligned} \tag{2.85}$$

The reflectivity r_0^* and its differential for s- and p-polarized lights are shown as eqs. (2.62), (2.64) and (2.70)–(2.73), respectively. The reflectivity r_a and r_b for each polarized lights are expressed as following equations, respectively,

$$r_{bs} = \frac{\cos\theta_i - \sqrt{n_b^2 - \sin^2\theta_i}}{\cos\theta_i + \sqrt{n_b^2 - \sin^2\theta_i}} \tag{2.86}$$

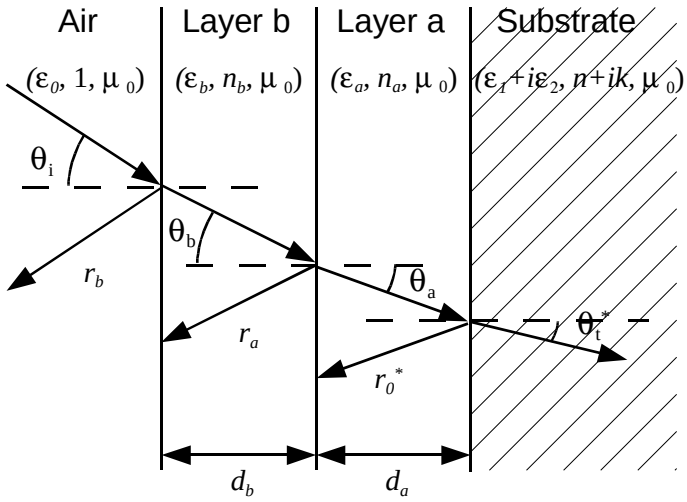

Figure 2.12: An illustration of obliquely-incident light near the region of double layers stacked on a substrate.

$$r_{as} = \frac{\sqrt{n_b^2 - \sin^2\theta_i} - \sqrt{n_a^2 - \sin^2\theta_i}}{\sqrt{n_b^2 - \sin^2\theta_i} + \sqrt{n_a^2 - \sin^2\theta_i}} \tag{2.87}$$

$$r_{ap} = \frac{n_a^2\sqrt{n_b^2 - \sin^2\theta_i} - n_b^2\sqrt{n_a^2 - \sin^2\theta_i}}{n_a^2\sqrt{n_b^2 - \sin^2\theta_i} + n_b^2\sqrt{n_a^2 - \sin^2\theta_i}} \tag{2.88}$$

$$r_{bp} = \frac{n_b^2\cos\theta_i - \sqrt{n_b^2 - \sin^2\theta_i}}{n_b^2\cos\theta_i + \sqrt{n_b^2 - \sin^2\theta_i}}. \tag{2.89}$$

Figure 2.13 shows the Seraphin coefficients for unpolarized light calculated by using eqs. (2.54) and (2.55). The spectral shape changes significantly and mercurially for the model with layer b. This change arises from the interference effect in 2 layers.

2.4.4 Complex Form of Reflectance

The relationship between reflectance and dielectric function shown as eq. (2.39) can be also expressed as complex form as shown below,

$$\begin{aligned}
\frac{\Delta R}{R} &= \alpha\Delta\varepsilon_1 + \beta\Delta\varepsilon_2 \\
&= \Re\left[\alpha\Delta\varepsilon_1 - (-1)\beta\Delta\varepsilon_2 + i\alpha\Delta\varepsilon_2 - i\beta\Delta\varepsilon_1\right] \\
&= \Re\left[\alpha\left(\Delta\varepsilon_1 + i\Delta\varepsilon_2\right) - i\beta\left(\Delta\varepsilon_1 + i\Delta\varepsilon_2\right)\right] \\
&= \Re\left[(\alpha - i\beta)\left(\Delta\varepsilon_1 + i\Delta\varepsilon_2\right)\right] \\
&= \Re\left[C_s\Delta\varepsilon^*\right],
\end{aligned} \tag{2.90}$$

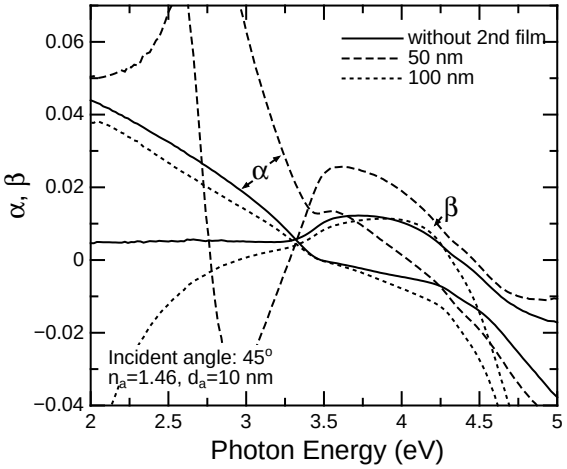

Figure 2.13: Calculated spectra of seraphin coefficients of the structures with and without multi-layer structure, α and β.

where $C_s = \alpha - i\beta$ and $\Delta\varepsilon^* = \Delta\varepsilon_1 + i\Delta\varepsilon_2$ are complex forms of Seraphin coefficient and dielectric function, respectively. Therefore, the reflectance difference is obtained by substituting eq. (2.28),

$$\frac{\Delta R}{R} = \Re\left[Ce^{i\theta}\left(E - E_g + i\Gamma\right)^{-n}\right], \tag{2.91}$$

where n depends upon dimension of the critical point, is $\frac{7}{2}$ for 1D, 3 for 2D and $\frac{5}{2}$ for 3D. The spectrum for all energy region is expressed as summation of the spectrum for all critical points,

$$\frac{\Delta R}{R} = \Re\left[\sum_j C_j e^{i\theta_j}\left(E - E_j + i\Gamma_j\right)^{-n_j}\right]. \tag{2.92}$$

2.4.5 Dependence of PRS Spectrum on Thickness and Refractive Index of Film

Figures 2.14 and 2.15 show PRS spectra of SiO_2(n = 1.46)/Si and high-refractive film(n = 2.2)/Si structures calculated by using Seraphin coefficients discussed in § 2.4.3, respectively. The spectral shape varies for thick film (> 100 nm). Moreover, the refractive index affects the spectral shape. This drastic change of the spectral shape is caused by the interference effect in the film. On the other hand, the spectral intensity changes little with thickness and refractive index. This means that PRS spectral intensity is not effected by optical property of the transparent film.

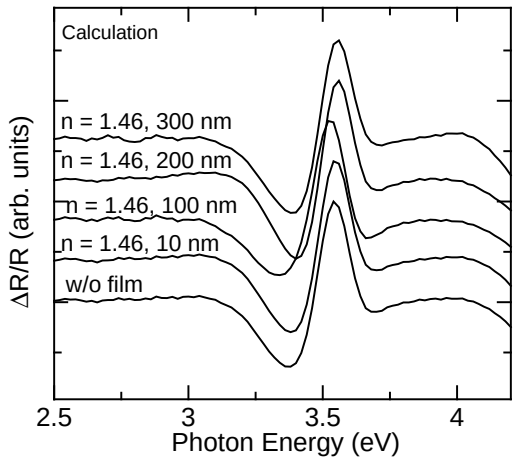

Figure 2.14: Calculated PRS spectra of SiO_2(n = 1.46)/Si structure. SiO_2 thicknesses are 10, 100, 200 and 300 nm.

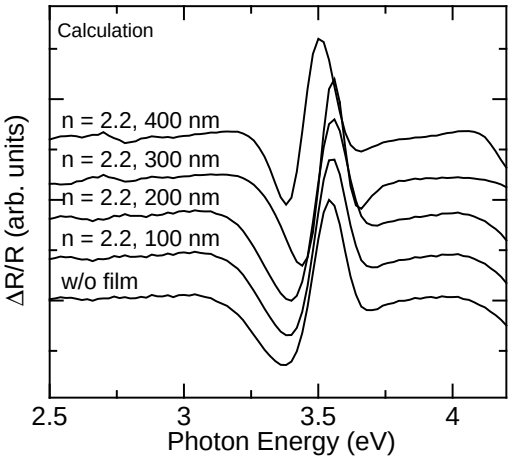

Figure 2.15: Calculated PRS spectra of high-refractive film(n = 2.2)/Si structure. The film thicknesses are 100, 200, 300 and 400 nm.

2.5 Spectral Intensity of Photoreflectance

2.5.1 Relation of PRS spectral intensity to Built-in Surface Potential

Under low electric field, the spectral intensity of PRS spectrum is proportional to square of electric field as shown in eq. (2.27) [23],

$$\frac{\Delta R}{R} \propto \mathcal{E}^2. \tag{2.93}$$

For actual PRS measurement, there is the built-in potential by Fermi level pinning effect at Si surface, so that the electric field not equal to zero even without the external electric field. Measured PRS spectrum is difference between that under a certain field $\mathcal{E}$ and that under the built-in electric field $\mathcal{E}_0$,

$$\begin{aligned} \frac{\Delta R}{R} &= \frac{\Delta R^{\mathcal{E}}}{R} - \frac{\Delta R^{\mathcal{E}_0}}{R} \\ &= k\mathcal{E}^2 - k\mathcal{E}_0^2 \\ &= k\Delta\left(\mathcal{E}^2\right), \end{aligned} \tag{2.94}$$

where k is constant which do not include the electric-field dependent term. Therefore, PRS spectrum is proportional to the difference between reflectances with and without electric field.

Figure 2.16 shows the energy band diagram near n-type Si surface with modulation light irradiation. Ψ_s and $\Delta\Psi_s$ are the built-in surface potential and difference potential induced by photo-generated carrier.

From Poisson's equation, the depletion width W and average electric field $\mathcal{E}(\Psi_s)$ is expressed as [10]

$$W(\Psi_s) = \sqrt{\frac{2\varepsilon_s\Psi_s}{qN_D}} \tag{2.95}$$

$$\mathcal{E}(\Psi_s) = \frac{\Psi_s}{W(\Psi_s)} = \sqrt{\frac{qN_D\Psi_s}{2\varepsilon_s}}, \tag{2.96}$$

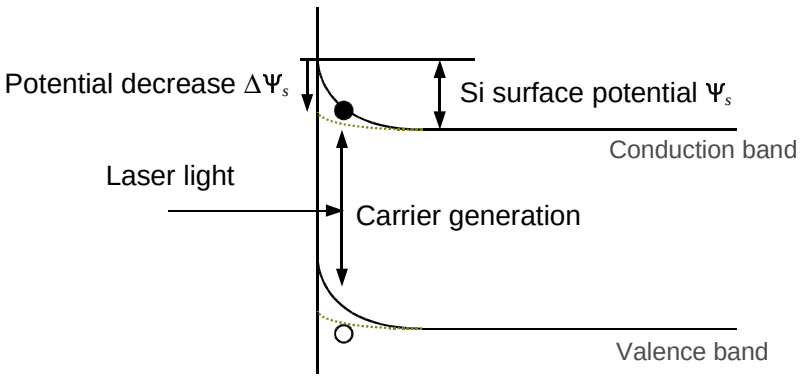

Figure 2.16: Energy band diagram near n-type Si surface with light irradiation.

Table 2.1: Variables for Si and Ar^+ laser

Reflectance	R_0	0.39
Effective Richardson constant	A^*	120 $Acm^{-2}K^{-2}$
Quantum efficiency	γ	0.58

where ε_s is the dielectric constant of Si. $\Delta\left(\mathcal{E}^2\right)$ in eq. (2.94) becomes

$$\Delta\left(\mathcal{E}^2\right) = \mathcal{E}^2\left(\Psi_s\right) - \mathcal{E}^2\left(\Psi_s - \Delta\Psi_s\right) = \frac{qN_D}{2\varepsilon_s}\Delta\Psi_s. \tag{2.97}$$

Therefore,

$$\frac{\Delta R}{R} \propto \Delta\Psi_s. \tag{2.98}$$

where above relationship is true when the following inequality is satisfied,

$$\Psi_s - \frac{E_c - E_F}{q} \gg \Delta\Psi_s. \tag{2.99}$$

Generally, this inequality is satisfied for almost of PRS measurement.

$\Delta\Psi_s$ is caused by photo-voltage V_m by irradiation of modulation light, so $\Delta\Psi_s = qV_m$. V_m is described by the equilibrium state of photo-generated carrier in the Schottky barrier. Neglecting recombination current in the depletion layer, we obtain a following equation [11].

$$\frac{P_m\gamma(1-R_0)}{\hbar\omega} = \frac{A^*T^2}{q}\exp\left[-\frac{\Psi_s}{kT}\right]\left[\exp\left(\frac{qV_m}{nkT}\right) - 1\right] \tag{2.100}$$

where P_m is area density of modulation light power, A^* is the effective Richardson constant, $\hbar\omega$ is photon energy of modulation light, γ and R_0 are quantum efficiency and reflectance of the sample at wavelength of modulation light, respectively, and n is the ideal factor. These variables for Si and Ar^+ laser (wavelength = 488 nm) which has been used in this work are shown in Table 2.1. Solving eq. (2.100) for $\Delta\Psi_s = qV_m$, we obtain,

$$\begin{aligned}\Delta\Psi_s &= nkT\ln\left[\frac{qP_m\gamma(1-R_0)}{A^*T^2\hbar\omega}\exp\left(\frac{\Psi_s}{kT}\right) + 1\right] \\ &\propto \ln\left[A\cdot\frac{P_m}{T^2}\exp\left(\frac{\Psi_s}{kT}\right) + 1\right],\end{aligned} \tag{2.101}$$

where

$$A = \frac{q\gamma(1-R_0)}{A^*\hbar\omega}, \tag{2.102}$$

is a constant. Therefore, from eqs. (2.98) and (2.101), PRS spectral intensity is expressed as a following equation,

$$\frac{\Delta R}{R} = B\cdot\ln\left[A\cdot\frac{P_m}{T^2}\exp\left(\frac{\Psi_s}{kT}\right) + 1\right], \tag{2.103}$$

where B is a constant.

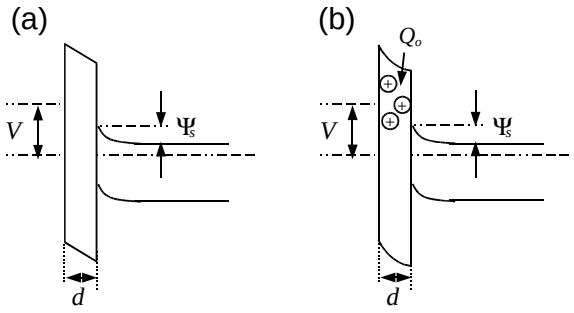

Figure 2.17: Band diagrams of insulator/Si structure for (a) ideal case, and (b) case of existence of positive charge in insulator.

2.5.2 Effect of Thickness and Dielectric constant of Dielectric film on Si

For an ideal insulator/n-Si structure as shown in Fig. 2.17 (a), the potential V at surface of insulator film is expressed as a sum of the voltage (V_i) applied to an insulator film and that (V_s) applied to Si surface,

$$V = V_i + V_s, \tag{2.104}$$

where $V_s = \frac{\Psi_s}{q}$. V_i is obtained by using the capacitance of insulator and the space charge Q_s induced at Si surface,

$$V_i = \mathcal{E}d = \frac{|Q_s|\,d}{\varepsilon_i}, \tag{2.105}$$

where d and ε_i are thickness and dielectric constant of insulator film, respectively. Q_s is obtained by solving the Poisson equation at Si surface [12],

$$|Q_s| = \frac{\sqrt{2}\varepsilon_s kT}{qL_D} F(\Psi_s), \tag{2.106}$$

where, L_D is the Debye length expressed as $L_D = \sqrt{\varepsilon_s kT/q^2 n}$. $F(\Psi_s)$ is expressed as a function of Si surface potential Ψ_s.

$$F(\Psi_s) = \sqrt{\left(e^{-\frac{\Psi_s}{kT}} + \frac{\Psi_s}{kT} - 1\right) + \frac{p}{n}\left(e^{\frac{\Psi_s}{kT}} - \frac{\Psi_s}{kT} - 1\right)} \tag{2.107}$$

Thus, substituting these equations to eq. (2.104), we obtain relation between potential V at insulator surface and Si surface potential Ψ_s,

$$V = \frac{\Psi_s}{q} + \frac{d}{\varepsilon_i}\frac{\sqrt{2}\varepsilon_s kT}{qL_D} F(\Psi_s) \tag{2.108}$$

PRS spectral intensity can be calcurated by using Ψ_s obtained from eqs. (2.103) and (2.108). Figure 2.18 shows the dependence of PRS spectral intensity on the insulator thickness (d) calculated from eq. (2.103) by substituting Ψ_s obtained by numerical calculation using eq. (2.108),

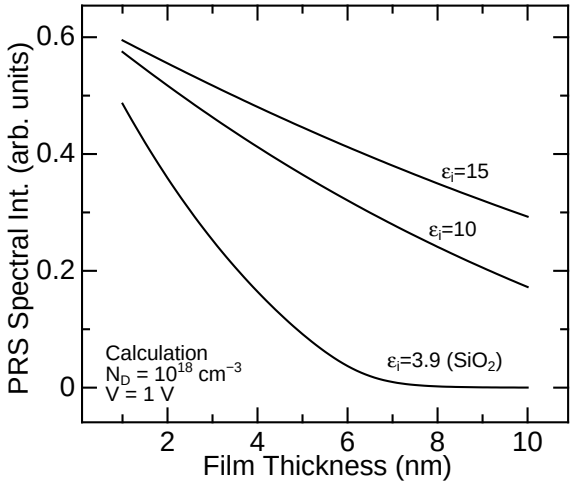

Figure 2.18: Peak intensities of calculated PRS spectra as a parameter of insulator thickness.

when $V = 1$ V, $n = 10^{18}$ cm^{-3} and $T = 300$ K. It is found that the PRS spectral intensity decreases with increasing insulator thickness. Moreover, the intensity for the high-k ($\varepsilon_i > 3.9$) insulator is larger than that for SiO_2 ($\varepsilon_i = 3.9$).

In the case of the existence of the effective oxide charge density (Q_o) (per unit area) in the insulator (Fig. 2.17 (b)), the potential at insulator surface V is transformed from ideal case (eq. (2.108)) as expressed by [12]

$$V = \frac{\Psi_s}{q} + \frac{d}{\varepsilon_i}\left[\frac{\sqrt{2}\varepsilon_s kT}{qL_D}F(\Psi_s) + qQ_o\right]. \tag{2.109}$$

The dependence of PRS spectral intensity on the positive oxide charge density (Q_o) calculated using eq. (2.103) by substituting Ψ_s obtained by numerical calculation using eq. (2.109) is shown in Fig. 2.19. Si surface potential decreases and consequently PRS spectral intensity decreases, as shown in Fig. 2.19.

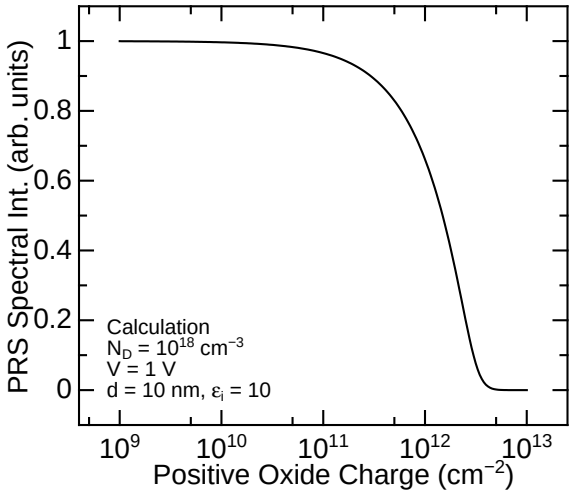

Figure 2.19: Dependence of PRS spectral intensity on positive oxide charge (Q_o) calculated using eqs. (2.109) and (2.103). Spectral intensity is normalized to equal 1 for ideal case ($Q_o = 0$).

2.6 Experiment of Photoreflectance

Measurement condition Figure 2.20 shows a schematic diagram for PRS measurement. The surface potential of the sample is modulated with an Ar^+ laser which has wavelength of 488 nm (Spectra-Physics Stabilite 2017) intermitted by a mechanical chopper (frequency: 100–200 Hz). Simultaneously, the sample is irradiated with a probe light from a Xe discharge lamp (Ushio UXL-500D) and reflected light from the sample is guided to the monochromator (Spex 1704). The light dispersed by the monochromator is detected by a photomultiplier (Hamamatsu R1508). A small change in reflectance (ΔR) is measured by a lock-in amplifier (NF 5610B) referring to chopping frequency. The reflectance (R) is measured by digital multimeter (Advantest R6551). All PRS measurements are performed in air at room temperature. Detailed conditions of PRS measurement is shown in Table 2.2.

Analysis of PRS spectrum Figure 2.21 shows an example of measured PRS spectrum of Al_2O_3/n-Si measured at room temperature. PRS spectrum is expressed by eq. (2.92). E_0' (3 dimension) and E_1 (2 dimension) critical points exist in the spectral range 3–4 eV. So, measured data of PRS spectrum should be fitted by using following equation,

$$\frac{\Delta R}{R} = \Re\left[C_0' e^{i\theta_0'}\left(E - E_0' + i\Gamma_0'\right)^{-5/2} + C_1 e^{i\theta_1}\left(E - E_1 + i\Gamma_1\right)^{-3}\right]. \tag{2.110}$$

The solid line in Fig. 2.21 is fitted curve by using eq. (2.110). The fitted spectrum suits the measured data. The dashed line and dotted line are E_0' and E_1 components of fitted spectrum, respectively. Fitted parameters of these components are shown in Table 2.3. It is found that E_0' and E_1 almost equal to reported value [13] are obtained by this fitting. It is considered that the sample is modulated by not only photo-carrier generation (PRS) but also heating by irradiation of modulation laser light. The thermally modulated spectrum is expressed as first derivative of non-modulated spectrum [9], which has obviously different spectral shape. If the thermal modulation effect is not negligible, the measured data cannot be fitted by using eq. (2.110). Therefore, in this work, we consider that thermal effect by irradiation of modulation light is negligible, so eq. (2.110) is used for curve fitting of PRS spectrum.

Measured region The penetration depth d_p of irradiated light is expressed as a following equation [1],

$$d_p = \frac{\lambda}{4\pi k}, \tag{2.111}$$

where λ is the wavelength of light and k is the extinction coefficient (imaginary part of comlex refractive index), respectively. For Si, k is about 3 around E_1 critical point, so d_p of the probe light becomes about 10 nm. Therefore, it is considered that the measured region by PRS is from surface to 10 nm.

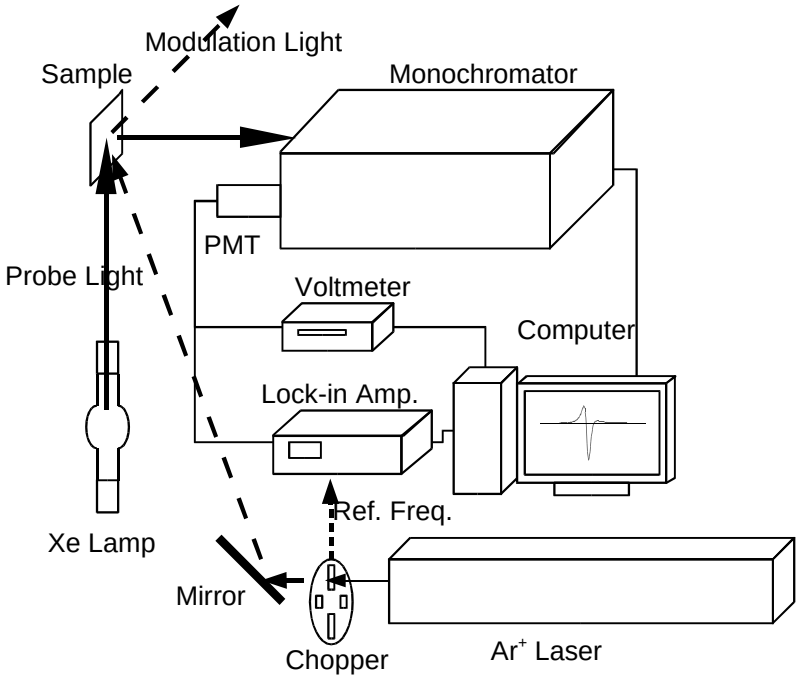

Figure 2.20: Schematic diagram for PRS measurement.

Table 2.2: Conditions of PRS measurement.

Probe light	Xe discharge lamp
Probe spot size	$\sim$ 0.1 mmϕ
Modulation light	Ar^+ laser 488 nm
Power of modulation light	0.2–1 W
Diameter of modulation light	1.4 mm
Wavelength region	330–400 nm
Chopping frequency	100–200 Hz
Incident angle of probe light	45°
Incident angle of modulation light	30°
Temperature	R. T.

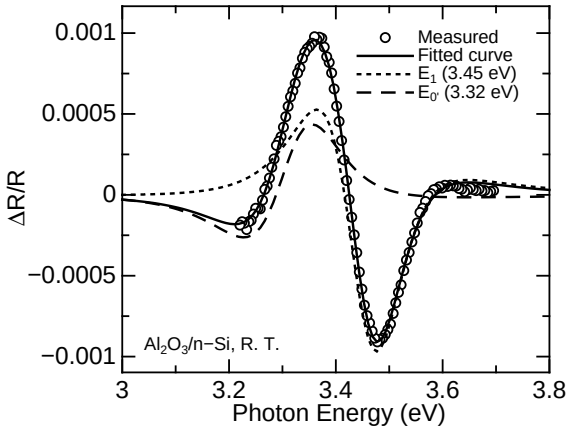

Figure 2.21: An example of PRS spectrum and fitted theoretical curve (solid line). Dashed and broken lines show spectra at E_1 and E_0' critical points, respectively, composing of the fitted curve.

Table 2.3: The parameters of curve fitting in Fig. 2.21.

Parameter	Fitted value
C_0'	3.08×10^{-6}
θ_0'	165°
E_0'	3.32 eV
Γ_0'	0.13 eV
C_1	2.30×10^{-6}
θ_1	41°
E_1	3.45 eV
Γ_1	0.13 eV

2.7 Summary

The theories of PRS have been described. The Seraphin coefficients, which show the relationship between reflectance and dielectric function, are calculated for dielectric film/Si structure. The spectral shape of PRS spectrum calculated by using Seraphin coefficients varies in the case of thick and high-refractive dielectric film/Si structure. On the other hand, PRS spectral intensity hardly depends on Seraphin coefficients.

PRS spectral intensity is expressed as a monotonically increasing function of Si surface potential. From calculation of space charge at Si surface of dielectric film/Si structure, it is found that PRS spectral intensity depends on thickness and dielectric constant of the film. Moreover, PRS spectral intensity is decreased by existence of positive charge in the film. It is considered that these properties of dielectric film can be investigated by using PRS.

Reference

[1] T. Hamaguchi: *Handoutai Butsuri* (Physics of Semiconductors) (Asakura Shoten, Tokyo, 2001) Chap. 4–5 [in Japanese].

[2] *Handbook of Mathematical Functions*, ed. M. Abramowitz and I. A. Stegun (Dover Publications, New York, 1964), p. 446.

[3] T. Kambayashi and Y. Kidou: *Hikari Electronics* (Optical Electronics) (Morikita-Shuppan, Tokyo, 1992) Chap. 2., p. 34–40 [in Japanese].

[4] B. O. Seraphin and N. Bottka: Phys. Rev. **145** (1966) 628.

[5] *Handbook of Optical Constants of Solids*, ed. E. D. Palik (Academic Press, San Diego, 1998), Vol. 3, p. 529, p. 535, p. 536.

[6] D. Huang, D. Mui and H. Morkoç: J. Appl. Phys. **66** (1989) 358.

[7] K. Kudou: *Bunkou no Kiso to Houhou* (Basis and Method of Spectroscopy) (Ohm-sha, Tokyo, 1985) 187.

[8] D. E. Aspnes: Surf. Sci. **37** (1973) 418.

[9] D. E. Aspnes: *Handbook on Semiconductors*, ed. M. Balkanski (North-Holland, New York, 1980), Vol. 2, Chap. 4A.

[10] K. Nemoto, R. Iwaki and H. Ohyama: *Handoutai Device Nyumon* (Introduction to Semiconductor Device), ed. T. Nakamura (Morikita-Shuppan, Tokyo, 1991) Chap. 10 [in Japanese].

[11] T. Kanata, M. Matsunaga, H. Takakura and Y. Hamakawa: J. Appl. Phys. **68** (1990) 5309.

[12] S. M. Sze, *Physics of Semiconductor Devices*, 2nd ed. (Wiley, New York, 1981) p. 368.

[13] *Semiconductors: group IV elements and III-V compounds*, ed. O. Madelung (Springer-Verlag, Berlin, 1991) p. 13.

Chapter 3

Characterization of SiO_2/Si Structure

3.1 Introduction

SiO_2 film has been used for the gate insulator for a long time because of its good characteristics. As described Chap. 1, alternative materials are examined instead of SiO_2 recently, it is still a basic and important material. In particular, the strained Si devices are expected for high-speed MOS-FET [1]. Hence, the necessity of evaluation techniques for determing the stress and strain has increased [2] curvature measurement [3, 4], electroreflectance [5] and Raman scattering [2] have already been proposed; however, these techniques have not yet been established as stress evaluation methods. We have attempted to apply PRS to monitor the stress induced at the SiO_2/Si interface [6]. The stress measurement was obtained by the empirical pseudopotential method [5] mentioned in Ref. [6]. In this chapter, characterization of SiO_2/Si structures by PRS is described. Firstly, the stress value is quantified by the shift of E_1 critical point obtained from PRS spectra, because it has been reported that E_1 critical point changes due to the strain induced at the Si/SiO_2 interface [7]. The stress was induced by using Si diaphragm structure. Secondly, the changes of stress and PRS spectral intensity with native oxide growth is monitored by PRS. As described in § 2.5.2, it is considered that SiO_2 thickness and the potential at SiO_2 surface can be characterized by PRS spectral intensity. Finally, PRS is applied to the stress between thermal oxidized SiO_2 and Si. Moreover, dependence of PRS spectral intensity on thickness of SiO_2 is discussed.

3.2 Measurement of Si Surface Stress by using Si Diaphragm

3.2.1 Sample Preparation

The n-Si (100) wafers (resistivity: $\sim$ 0.02 Ω cm) were used for substrates. The Si diaphragm structure was fabricated to produce the strain at the Si surface by anisotropic etching in mixture of ethylenediamine pyrocatechol water (EPW). The mixing ratio of EPW solution was ethylenediamine(ml) :

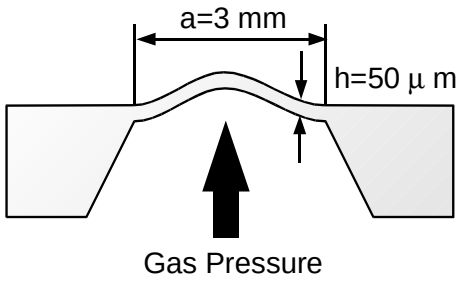

Figure 3.1: Cross-sectional view of the Si diaphragm structure prepared by preferential etching.

pyrocatechol(g) : water(ml) = 17 : 3 : 8. Covering the surface by thermal oxide, the Si substrate was etched from the back. Etching time and temperature of EPW solution were 10 h and 114°C, respectively. After etching, the thermal oxide on the surface was removed, and an ultrathin chemical oxide was newly grown by boiling with HNO_3 solution (60%, boiling point: 122°C) to enhance PRS spectral intensity.

The lateral dimensions of diaphragm were about 3×3 mm^2, and the thickness of the diaphragm was approximately 50 μm. The diaphragm was set and pressed from the back side by compressed N_2 gas. Cross sectional view of pressed diaphragm structure is shown in Fig. 3.1.

3.2.2 Strain estimation by elastic analysis

Prior to strain evaluation by PRS spectrum, the strain of the diaphragm was estimated by elastic analysis. The coordinate of the diaphragm is defined as horizontal center of the diaphragm becomes coordinate origin. The diaphragm is a regular tetragon, whose four sides are fixed. The side length is $2a$ and the thickness of the diaphragm is h. The bending rigidity of this diaphragm is given as

$$D \equiv \frac{Eh^3}{12\left(1-\nu^2\right)}, \tag{3.1}$$

where E is Young's modulus of Si and ν is Poisson's ratio of Si. When a uniform pressure P bends the diaphragm, the vertical displacement w of the diaphragm is given as follows,

$$w\left(x,y\right) = \frac{\alpha}{12a^2}\frac{P}{D}\left(x^2-a^2\right)^2\left(y^2-a^2\right)^2, \tag{3.2}$$

where α is a constant (~ 0.383).

The diaphragm deformation generates the bending stress σ_x and horizontal strain ϵ_x. When the central plane of the diaphragm is taken as the origin, the values of σ_x and ϵ_x are given by the following equations:

$$\sigma_x\left(x,y,z\right) = \frac{E}{1-\nu^2}\frac{z}{\rho_x\left(x,y\right)} \tag{3.3}$$

$$\epsilon_x\left(x,y,z\right) = \frac{z}{\rho_x\left(x,y\right)} \tag{3.4}$$

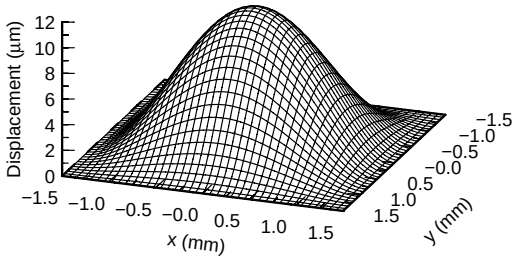

Figure 3.2: Spacial distribution of calculated displacement w of the diaphragm. The pressure P is 100 kPa.

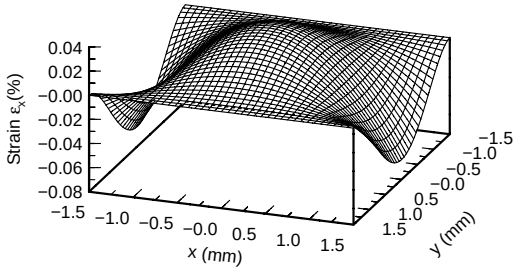

Figure 3.3: Spacial distribution of calculated horizontal strain (x-component) ϵ_x at surface ($z = h/2$) of the diaphragm. The pressure P is 100 kPa.

$$\frac{1}{\rho_x(x,y)} = -\frac{\partial^2 w}{\partial x^2}(x,y), \tag{3.5}$$

where $\epsilon_x > 0$ indicates a tensile strain and $\epsilon_x < 0$ indicates a compressive strain. From eqs. (3.3) and (3.4), the relationship between the stress and the strain is given by the following equation,

$$\sigma_x = \frac{E}{1-\nu^2}\epsilon_x. \tag{3.6}$$

The next equation is obtained by substituting $w(x,y)$ with eq. (3.2).

$$\epsilon_x(x,y,z) = -\frac{2\alpha}{9a^4}\frac{P}{D}z\left(3x^2-a^2\right)\left(y^2-a^2\right)^2. \tag{3.7}$$

Substituting $h/2$ for z, Si surface strain is obtained as follows,

$$\epsilon_x(x,y) = -\frac{\alpha h}{9a^4}\frac{P}{D}\left(3x^2-a^2\right)\left(y^2-a^2\right)^2. \tag{3.8}$$

Figures 3.2 and 3.3 show the calculated distributions of displacement $w(x,y)$ and horizontal strain (x-component) at the diaphragm surface ϵ_x toward x-y position on the diaphragm, respectively. Where, $P = 100$ kPa, $E = 130$ GPa, $\nu = 0.28$ for Si (100) [8] are used for calculation.

The reliability of the estimation by the elastic analysis was confirmed by measuring the vertical displacement of the Si diaphragm by laser triangulation using an optical displacement gauge (as shown in Fig. 3.4). Figure 3.5 shows a comparison between the calculated displacement by elastic analysis and the directly measured one at points along x axis ($y = 0$). There is good agreement between the calculated and measured displacements. Hence, it is considered that the estimation by elastic analysis gives us reasonable results.

3.2.3 Relation between PRS spectrum and Stress at Si Diaphragm Surface

The PRS spectra were measured for the Si diaphragm with and without N_2 gas pressing. Figure 3.6 shows the PRS spectra with and without gas pressing. It appears that N_2 gas pressing changes the

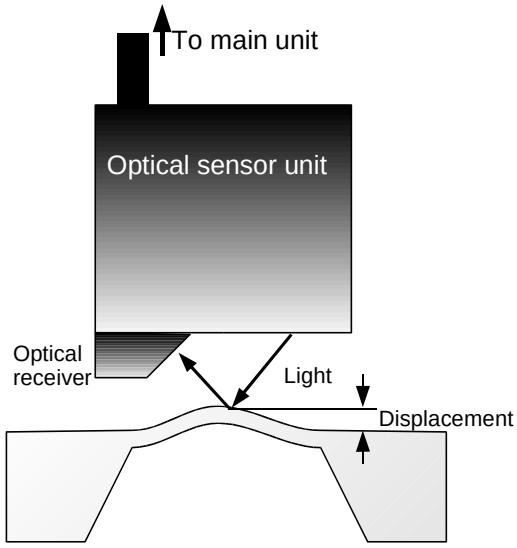

Figure 3.4: Measurement of vertical displacement of Si diaphragm by using an optical displacement gauge.

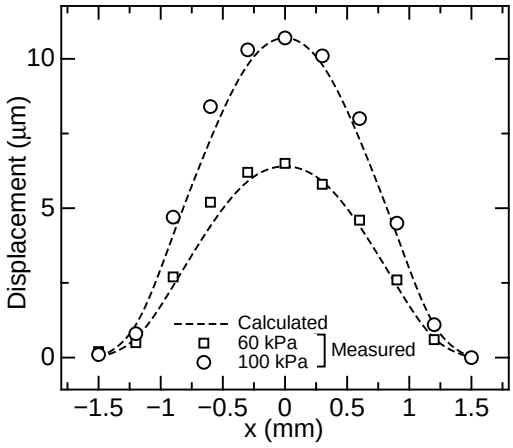

Figure 3.5: Spacial distribution of calculated (dashed lines) and measured (open circles and squares) displacements along x-axis of the Si diaphragm.

PRS spectrum. E_1 critical point were obtained by curve fitting using eq. (2.110). The relationship between E_1 critical point and the N_2 gas pressure is shown in Fig. 3.7. The top axis of Fig. 3.7 is the surface stress obtained by using eqs. (3.6) and (3.8). It is found that E_1 critical point is proportional to the gas pressure and the surface stress σ_x.

As shown in Fig. 3.3, tensile strain is generated near the center of the diaphragm surface, while the compressive strain is generated near the fringe of the diaphragm. The lateral distribution of PRS spectrum was obtained by scanning the probe light beam along the x-axis on the x-y coordinate of the diaphragm. Near the center of the diaphragm, tensile strain is induced at diaphragm surface, as shown in Fig. 3.3. On the other hand, near the fringe of the diaphragm, compressive strain (negative value in Fig. 3.3) is induced. Figure 3.8 shows the relationship between the calculated strain and E_1 obtained from PRS spectra. The top axis of Fig. 3.8 is the surface stress obtained by using eq. (3.8). Figure 3.9 shows E_1 obtained from PRS spectra vs the surface stress obtained by combining Figs. 3.7 (open square) and 3.8 (open circle). E_1 critical point shows a good correlation with the surface stress. The dashed line in Fig. 3.9 shows the result of linear fitting expressed as a following equation.

$$E_1 = 3.45 - 0.001\sigma_x \quad \text{[eV]}, \tag{3.9}$$

where the unit of σ_x is MPa. E_1 critical point shifts to low energy side with tensile stress of Si surface.

As a result, Si surface stress σ_x can be obtained from E_1 critical point by using a following

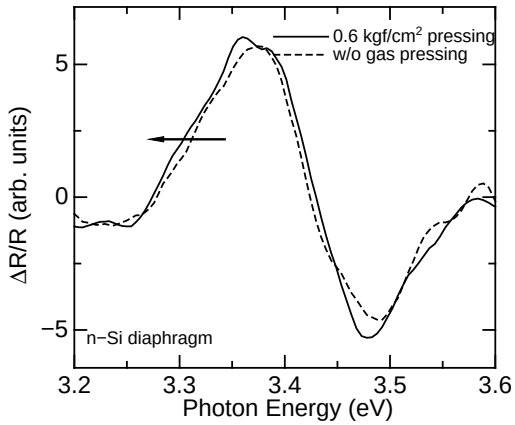

Figure 3.6: Measured PRS spectra with (solid line) and without (dashed line) stress application induced by N_2 gas pressing.

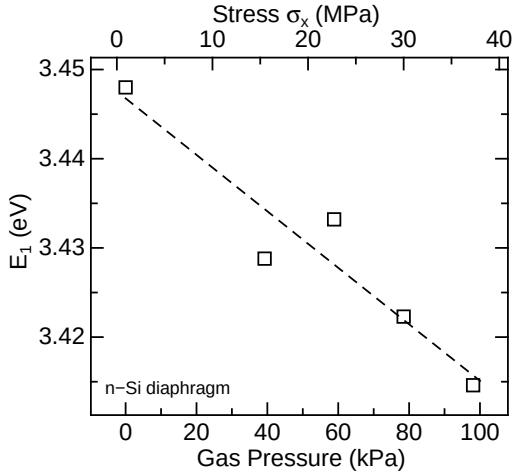

Figure 3.7: E_1, transition energy of critical point obtained from PRS spectra as a function of N_2 gas pressure. Interpolated curve is shown with dashed line.

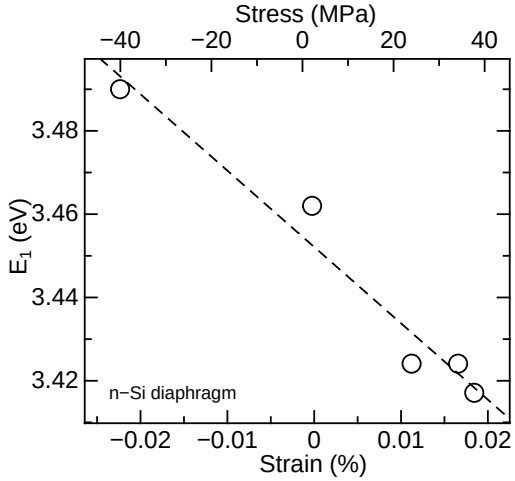

Figure 3.8: E_1, transition energy of critical point and stress obtained from lateral distribution as a function of calculated strain.

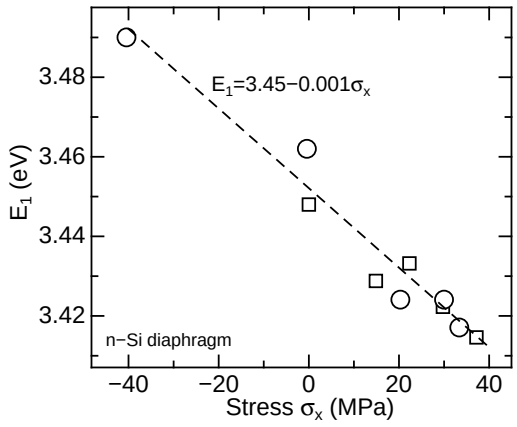

Figure 3.9: E_1, transition energy of critical point vs. the surface stress of the diaphragm.

equation,

$$\sigma_x = a(E_1(0) - E_1(\sigma_x)), \tag{3.10}$$

where $a = 1 \times 10^{-9}$ eV/Pa. $E_1(0)$ is E_1 critical point in the case of no stress in Si. It is well known that Si surface is given large tensile stress by Si oxide grown on that [9]. We should note that there is stress in the diaphragm even without N_2 gas pressing because of existing the oxide to PRS spectra measurable. So, $E_1(0)$ is not equal to 3.45 eV. $E_1(0)$ is obtained from PRS measurement of native oxidation of Si, as described in a follow section.

3.3 Monitoring of Native Oxide Growth

3.3.1 Experimental Procedures

After cleaning by RCA method, Si (100) substrates (n-type or p-type, resistivity: $\sim 0.02\ \Omega$ cm) were dipped into buffered HF (NH_4HF_2 20%) to remove the surface oxide. Then they were exposed to air for about 90 d to grow native oxide. X-ray photoelectron spectroscopy (XPS) measurement was carried out for determination of native oxide thickness. Si $2p$ spectra were measured by XPS instruments (Shimadzu-Kratos Axis-Hsi2). The X-ray source with Mg Kα radiation was used without a monochromator. SiO_2 thickness d_{ox} were determined from ratio of chemically-shifted integrated intensity I_{SiO_2} to not-shifted integrated intensity I_{Si} of Si $2p$ peak, using by following equation [10],

$$d_{ox} = \lambda_{SiO_2} \cos\theta \ln\left(k\frac{I_{SiO_2}}{I_{Si}} + 1\right), \tag{3.11}$$

where $k = 2.086$ is a constant, $\lambda_{SiO_2} = 2.5$ nm is the escape depth of photoelectron in SiO_2, and θ is the escape angle of photoelectron.

3.3.2 PRS Spectral Intensity with Native Oxide Growth

Figure 3.10 shows PRS spectra of naturally oxidized n-Si as a parameter of the exposure time. PRS spectral intensity increases with increasing the exposure time. The dependence of XPS Si $2p$ spectrum intensity on the exposure time is shown Fig. 3.11. It is found that chemical-shifted peak intensity (from the Si-O bond) increases with increasing the exposure time. Thus, native oxide growth progresses continually with exposure to air.

Figure 3.12 shows PRS spectral intensity and native oxide thickness calculated from eq. (3.11) as a function of the exposure time. Assuming that the oxide growth follows Deal-Groove model, the oxide thickness is expressed a following equation in the case of a long time oxidation [9].

$$d_{ox}^2 \simeq Bt, \tag{3.12}$$

where B is parabolic rate constant. The dot-dashed curve in Fig. 3.12 is the curve fitted to measured oxide thickness by eq. (3.12). The rate constant B is determined 0.000171 nm^2/h by curve fitting. Figure 3.13 shows PRS spectral intensity vs native oxide thickness calculated from eq. (3.12). PRS spectral intensity is approximately proportional to native oxide thickness. Assuming that the potential at native oxide surface is constant, PRS spectral intensity must decrease with increasing the oxide thickness, as shown in Fig. 2.18. Therefore, this result means that the potential at native oxide surface increases with native oxidation.

On the other hand, for p-type Si, PRS spectral intensity decreases with increasing the exposure time as shown in Fig. 3.14. PRS spectral intensity is expressed as a function of downward

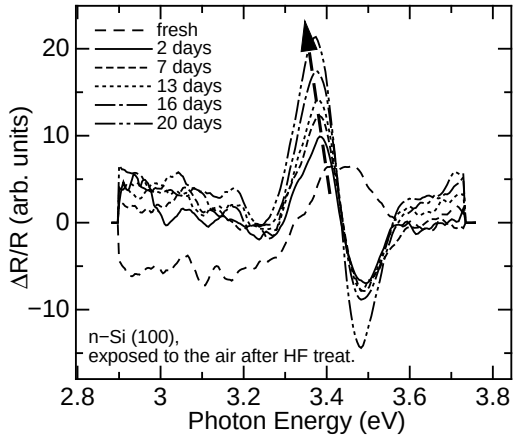

Figure 3.10: Dependence of PRS spectra on the exposure time in air atmosphere.

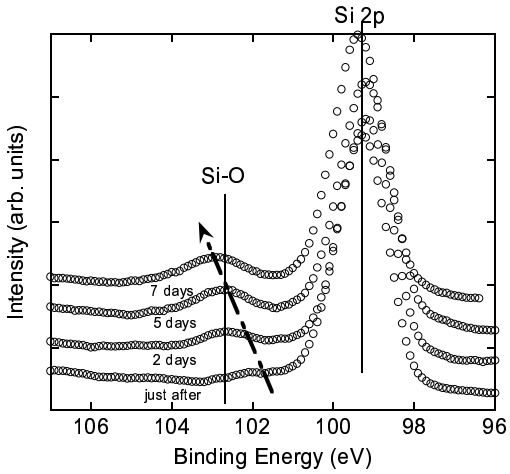

Figure 3.11: Dependence of XPS Si 2*p* spectra on the exposure time.

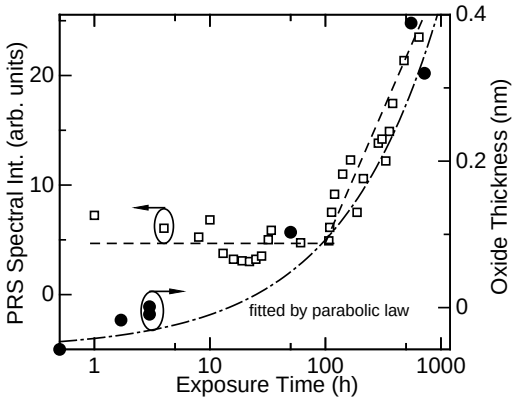

Figure 3.12: PRS spectral intensity (open square) and native oxide thickness (closed circle) as a function of the exposure time.

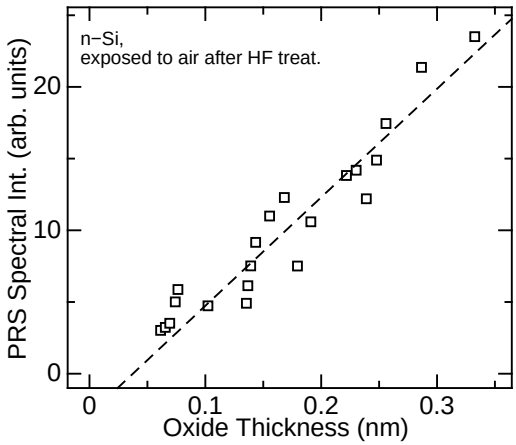

Figure 3.13: PRS spectral intensity vs. native oxide thickness.

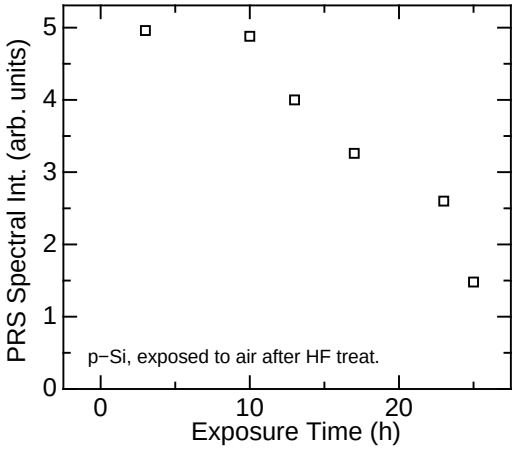

Figure 3.14: PRS spectral intensity as a function of the exposure time for p-type Si.

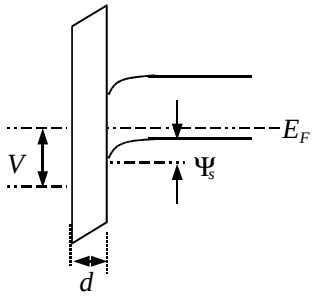

Figure 3.15: Energy band diagram for insulator/p-Si structure.

band bending in the energy band diagram for p-Si, as shown in Fig. 3.15 (cf. Fig. 2.17 for n-Si). Thus, when the potential V at oxide surface changes from downward to upward in band diagram corresponding to conduction type of Si (it means that surface charge at oxide surface changes from positive to negative), PRS spectral intensity for n-Si increases and that for p-Si decreases, respectively.

We can consider a following model from these results. Si surface is positively charged by hydrogen-termination just after HF treatment. Hydrogen-termination decreases as Si surface is naturally oxidized. The SiO_2 surface is negatively charged in air [11] because of adsorbed hydroxide ions [12].

3.3.3 Increase of Tensile Stress by Native Oxide Growth

PRS spectra normalized by peak intensity of them are shown in Fig. 3.16 (same spectra in Fig. 3.10). PRS spectrum shifts to low energy side with increasing the exposure time. The shift of E_1 critical point obtained by curve fitting of PRS spectrum is shown in Fig. 3.17. E_1 critical point linearly changes toward native oxide thickness.

The stress is usually sum of thermal stress and intrinsic stress [2]. The thermal stress is generated when the sample is cooled after oxide growth, and originates from difference of thermal expansion coefficient between SiO_2 and Si. The intrinsic stress is due to the molar volume mismatch between the Si substrate and the oxidized SiO_2 film, as shown in Fig. 3.18. In this temperatures case, oxidation and PRS measurement temperatures are the same, room temperature, hence thermal stress is almost zero and the stress is only the intrinsic stress.

The dashed line in Fig. 3.17 shows a linear fitting result. y-intercept of this line is $E_1 \sim 3.59$ eV. It is considered that the surface stress is zero at $d_{ox} = 0$ so that $E_1(0)$ in eq. (3.10) is

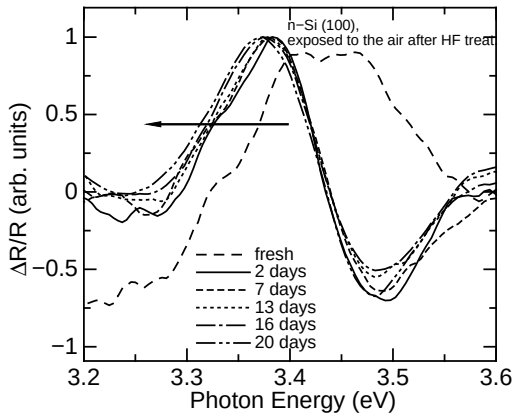

Figure 3.16: Dependence of shift of PRS spectra on the exposure time of Si in air atmosphere.

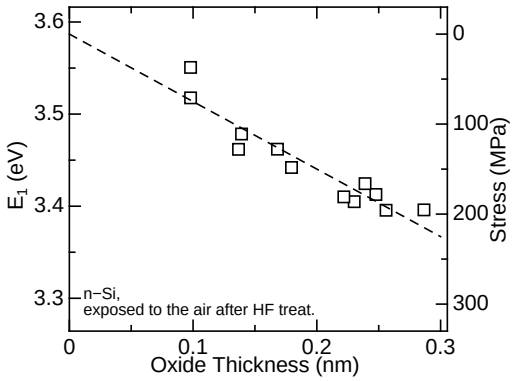

Figure 3.17: Oxide thickness dependences of E_1, the transition energy at E_1 critical point obtained by curve fitting of PRS spectrum and interface stress.

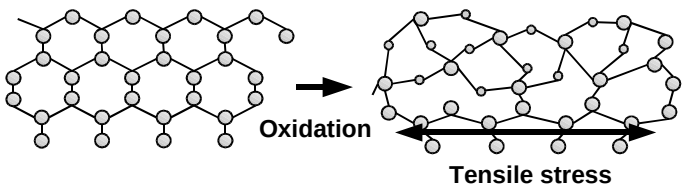

Figure 3.18: Model illustration of appearance of tensile stress at Si interface induced by oxide growth.

3.59 eV. The right axis of Fig. 3.17 shows stress calculated from eq. (3.10). It is found that the Si surface stress reaches 200 MPa when native oxide grows to 0.3 nm.

3.4 Characterization of Thermal Oxidation

3.4.1 Experimental Procedure

The n-Si (100) wafers (~ 0.02 Ω cm) were cleaned by RCA method and treated by buffered HF to remove of the native oxide. The growth of SiO_2 thin film was carried out in a dry O_2 atmosphere. The oxide thickness was measured by the ellipsometer (Mizojiri DVA-36VW-UV) or XPS. Figure 3.19 shows comparison of the oxide thickness measured by XPS with that measured by ellipsometry. Both thicknesses well agree in the range 2–5 nm, however, they do not agree in further range. Thickness measurement by XPS is valid in $d_{ox} < 3\lambda_{ox} = 7.5$ nm [13]. Thus, we use SiO_2 thickness value measured by XPS in the range less than 5 nm or by ellipsometry in above range.

3.4.2 Stress at Interface between Si and Thermal Oxide

Large strain arises on the surface because of the lattice mismatch between Si and SiO_2 as well as the case of native oxide growth. Si receives tensile strain and SiO_2 receives compressive strain. According to previous reports [2–5], the stress decreases as the growth temperature of the oxide increases. PRS spectra were measured for samples oxidized at various growth temperatures for 30 min. Figure 3.20 shows PRS spectra for these samples. The spectra are normalized by peak intensity of them. The spectrum of the lower oxidation samples is located at a lower energy side than that of the higher oxidation sample. Figure 3.21 shows the relationship between the growth temperature of the oxide and E_1 critical point obtained by curve fitting of PRS spectra. E_1 increases with increasing growth temperature. The stress calculated from E_1 by using eq. (3.10) is as shown on the right-hand-side y-axis in Fig. 3.21. The stress decreases with increasing growth temperature. These results agree well with tendencies of the previous reports [2–5]. The oxide thickness is 10–1000 nm, as mentioned in Refs. [2–4], however, 1–5 nm oxide thickness was used in this experiment. The stress value in the previous reports (~ 300 MPa at 700°C) is larger than our value (~ 100 MPa at 700°C). Hence, we considered that the stress is lower than that mentioned in previous reports.

Generally, the Raman spectroscopy is utilized for characterization of lattice strain [14]. Figure 3.22 shows Raman spectra (Renishaw Ramascope1000) of SiO_2/Si structures. The SiO_2 thicknesses are 0.7, 5, 6, 10 nm, respectively. The Raman peak shift caused by lattice strain cannot be observed in Fig. 3.22. The Ar ion laser (514.5 nm) was used for exciting light source of these raman measurement. Using eq. (2.111), the penetration depth at 514.5 nm is about 500 nm. Therefore, raman peak includes characteristics at not only Si surface but also inside to 500 nm. It is considered that the intrinsic stress caused by the molar volume mismatch between the Si substrate and the SiO_2 film localizes near Si surface. Moreover, the Raman shift is 3–8 cm^{-1}/GPa (for zinc

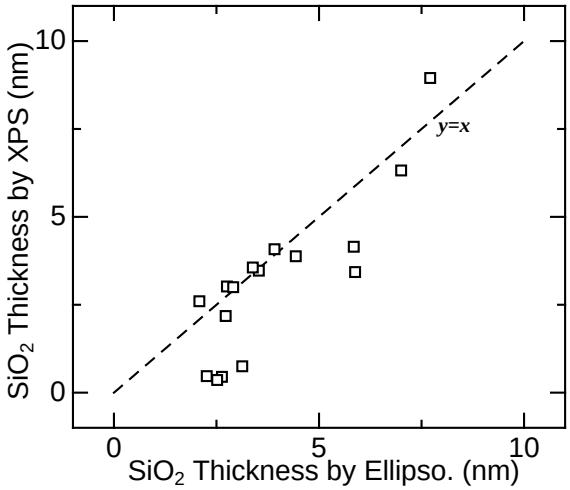

Figure 3.19: Relation between oxide thicknesses estimated by XPS and that measured by ellipsometry.

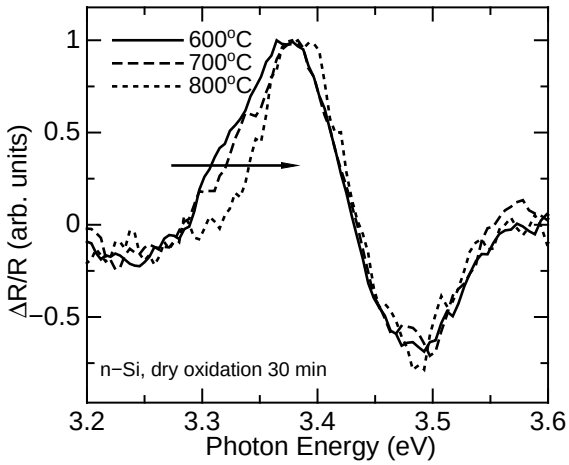

Figure 3.20: PRS spectra for samples oxidized at various temperatures. Peak intensity are normalized with positive peak value.

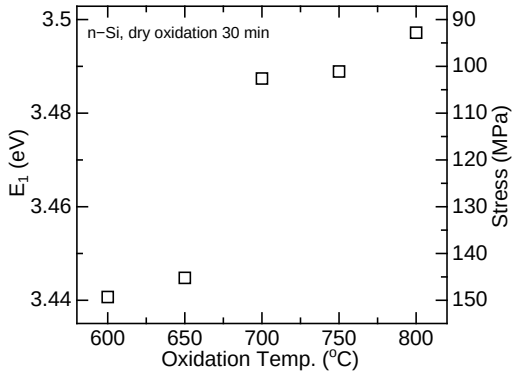

Figure 3.21: E_1 transition energy at critical point and corresponding stress as a function of oxide growth temperature.

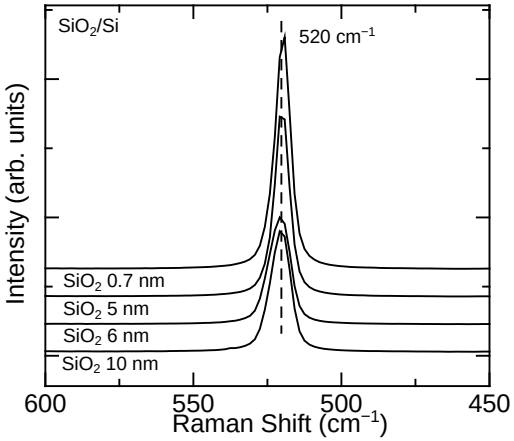

Figure 3.22: Raman peaks at 520 cm^{-1} of the SiO_2/Si structures. The SiO_2 thicknesses are 0.7, 5, 6, 10 nm, respectively.

blende structure, by hydrostatic pressure). Very high spectral resolution ($\sim$ 0.01 cm^{-1}) need to measure the stress of 10 MPa. It is considered that PRS is better for stress measurement near Si surface and smaller order ($\sim$ 10 MPa) than Raman spectroscopy.

3.4.3 Dependence of PRS Spectral Intensity on SiO_2 Thickness

To measure the dependence of PRS spectral intensity on SiO_2 thickness, the thermally oxidized SiO_2 films which have various thicknesses were prepared by changing the oxidation time or etching time by dilute HF (0.1%). Figure 3.23 shows PRS spectral intensity as a function of thermal oxide thickness. PRS spectral intensity decreases with increasing thickness of 3 nm and above. This dependence agrees with that in Fig. 2.18. It is considered that the potential at SiO_2 (> 3 nm) surface becomes a constant value. On the other hand, the spectral intensity increases with increasing thickness less than 3 nm. This dependence can be explained similarly to § 3.3.2. Namely, SiO_2 surface charge gradually varies from positive to negative with increasing SiO_2 thickness (< 3 nm).

3.5 Summary

The SiO_2/Si structure has been characterized by PRS. Si diaphragm structure was prepared by anisotropic etching to give stress to Si surface. E_1 critical point obtained from curve fitting of PRS spectrum is linearly changed by Si surface stress given by pressing Si diaphragm. It is found that relationship between E_1 and Si surface stress is obtained by using elastic analysis of diaphragm so that Si surface stress can be estimated from the PRS spectrum.

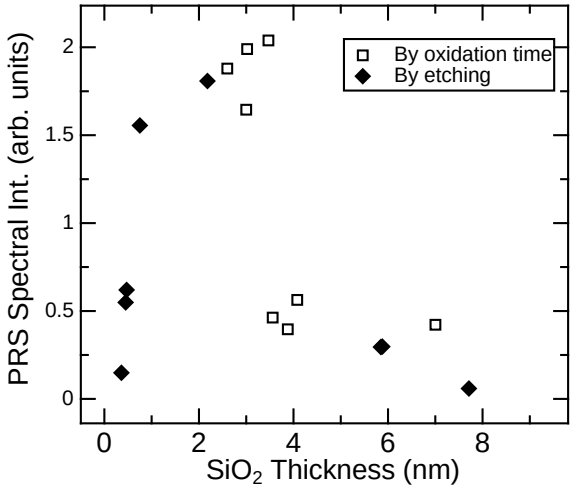

Figure 3.23: PRS spectral intensity as a function of SiO_2 thickness. Open squares show samples prepared by various oxidation time, closed diamonds show samples prepared by HF etching.

PRS spectral intensity increases with native oxide growth. This means that surface charge at native oxide varies from the positive value to the negative with growth. Moreover, E_1 critical point obtained from PRS spectrum linearly decreases with native oxide thickness. It is considered that the tensile stress at Si surface increases with oxide growth because of molar volume mismatch between Si substrate and SiO_2 film.

Si surface stress by thermally-oxidation decreases with increase of oxidation temperature. Estimated tensile stress is about 150 MPa for 600°C growth and about 90 MPa for 900°C growth. The dependence of PRS spectral intensity on SiO_2 thickness has been measured. PRS spectral intensity decreases with increasing thickness of 3 nm and above. On the other hand, it increases with increasing thickness of less than 3 nm. It is considered that PRS spectral intensity is inseparably connected to the charge state at SiO_2 surface.

Reference

[1] T. Mizuno: Oyo buturi **72** (2003) 1130.

[2] J. T. Fitch, C. H. Bjorkman, G. Lucovsky, F. H. Pollak and X. Yin: J. Vac. Sci. & Technol. **B7** (1989) 775.

[3] L. M. Mack, A. Reisman and P. L. Bhattacharya: J. Electrochem. Soc. **136** (1989) 3433.

[4] E. Kobeda and E. A. Irene: J. Vac. Sci. & Technol. **B4** (1986) 720.

[5] M. Morifuji, P. Youngwattanasoontorn, K. Taniguchi, C. Hamaguchi and Y. Ozawa: Jpn. J. Appl. Phys. **32** (1993) 2735.

[6] T. Imai, A. Fujimoto, M. Okuyama and Y. Hamakawa: Jpn. J. Appl. Phys. **35** (1996) 1073.

[7] Z. Yang, Y. H. Chen, J. Y. L. Ho, W. K. Liu, X. M. Fang and P. J. McCann: Appl. Phys. Lett. **71** (1997) 87.

[8] C. Wilson and P. Beck: J. Microelectromechanical Systems **5** (1996) 142.

[9] F. Shimura: *Handoutai Silicon Kesshou Kougaku* (Crystal Engineering of Silicon Semiconductors) (Maruzen, Tokyo, 1993) Chap. 4 [in Japanese].

[10] M. Hirose, M. Takakura, T. Yasaka and S. Miyazaki: Hyoumen Kagaku **13** (1992) 324 [in Japanese].

[11] T. Watanabe, M. Maeda, Y. Imai, Y. Ishikawa, H. Ikeda and M. Tabe: Ext. Abstr. (65th Autumn Meet. 2004); Japan Society of Applied Physics, 3a-P9-36.

[12] S. R. Morrison: *Electrochemistry at Semiconductor and Oxidized Metal Electrodes* (Penum Press, New York, 1980) p. 49.

[13] *X-sen Koudenshi Bunkouhou* (X-ray Photoelectron Spectroscopy), ed. The Surface Science Society of Japan (Maruzen, Tokyo, 1998) p. 194 [in Japanese].

[14] *Handoutai Hyouka Gijutsu* (Characterization Techniques of Semiconductors), ed. T. Katoda (Sangyotosho, Tokyo, 1989) p. 281–291 [in Japanese].

[15] *Hakumaku no Rikigaku-teki Tokusei Hyouka Gijutsu* (Characterization Techniques of Kinetic Properties of Thin Films), ed. A. Kinbara, (Realize, Tokyo, 1992) p. 264–271.

Chapter 4

Characterization of High-k/Si Structures

4.1 Introduction

As mentioned in Chap. 1, high-k films have various difficulty compared with SiO_2. In particular, growth of the interfacial layer between film and substrate and large fixed charges in film affect electric characteristics of FET fabricated using high-k/Si structure. The interfacial layer decreases total dielectric constant of the film so that capacitance of the film closes to SiO_2. The flat band shift is caused by fixed charges. Their affects emerge as change of Si surface potential. PRS spectral intensity is a function of Si surface potential, as shown in § 2.5. So, it is considered that their affects can be characterized by PRS spectral intensity.

In this chapter, various high-k thin films/Si structures are characterized by PRS. The excimer laser irradiation effect is employed to confirm the relation between amount of defects in high-k film and PRS spectral intensity. It is already reported that defects in SiO_2 film is increased by laser irradiation [1]. Then deposition conditions and rapid thermal annealing (RTA) conditions of HfO_2, PrO_x and other materials films are characterized by using PRS. HfO_2 is mainstream of the material for gate oxides in recently [2, 3]. PrO_x (because the prepared film includes Pr_2O_3 and Pr_6O_{11} phase [5]) has been one of high-k film of lanthanoid oxide candidates. Lanthanoid oxides have high dielectric constant (20–30), so they have attracted attention as next-generation high-k materials [4].

4.2 Sample Preparation

4.2.1 Pulsed Laser Deposition Method

After RCA cleanings and buffered HF (NH_4HF_2 20%) treatment, high-k thin films were deposited on Si substrate by using pulsed laser deposition (PLD) method. PLD has following features [5];

- wide range of ambient gas pressure
- carbon-free
- no plasma damage

The schematic diagram of PLD equipment is shown in Fig. 4.1. Samples were set in high-vacuum chamber, then ArF excimer laser beam (Lambda Physik LPX 100; wavelength: 193 nm) was applied to the ceramic targets and ablated particles were deposited on Si surface. The detailed condition of PLD is shown in Table 4.1.

For electric characterization, Al electrodes were deposited by vacuum evaporation (Ulvac EBH-6) on HfO_2/Si. The base vacuum chamber pressure is about 2×10^{-6} Torr. The size of electrode is about 0.15 mmϕ.

4.2.2 Metal Organic Decomposition Method

Some high-k films were also deposited by metal-organic decomposition (MOD) method. This method allows a simple preparation without vacuum process and a film deposited uniformly. After organic cleanings and HF treatment, a precursor solution (Kojundo SK-AL04, SYM-ZR04 and SYM-LA01) was spin-coated on Si substrate. Then samples were dried in air and annealed in O_2 atmosphere. Detail of MOD process is shown in Fig. 4.2. The materials are ZrO_2, Al_2O_3 and La_2O_3.

4.2.3 RTA Treatment

The rapid thermal annealing (RTA) is an annealing treatment using the infrared heating equipment (Nihon-tokusyukikai VF-11-461F). Figure 4.3 shows the sample-temperature control process for RTA. The sample is rapidly heated-up by irradiation of an infrared lamp. The rate of heat-up is about 50°C/sec. Then the sample temperature is held constant for holding time. The furnace is cooled by coolant water after holding temperature. The atmospheres of RTA treatment are N_2, O_2 and $H_2(5\%)/N_2$ (known as a forming gas). The flow rate of gas is 1 l/min.

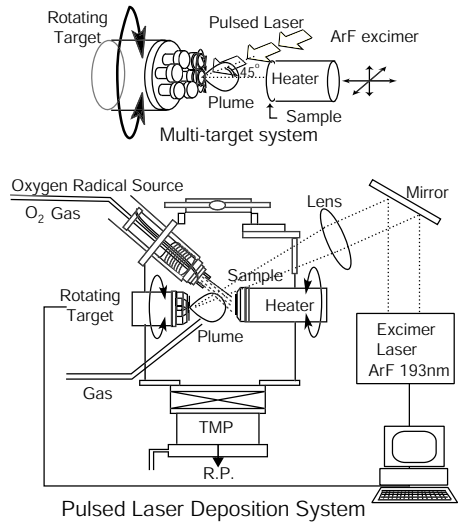

Figure 4.1: Schematic diagram of PLD apparatus.

Table 4.1: Deposition conditions of PLD.

Sintered target	HfO_2, Pr_6O_{11} ceramics
Substrate	n-type Si(100) (0.01–0.02 Ω cm) for PRS measurement
	n-type Si(100) (1000–2000 Ω cm) for ESR measurement
	p-type Si(100) (0.7–10 Ω cm) for electric measurement
Substrate temperature	R. T.–600°C
Gas	O_2, N_2
Pressure	~ 0.02 Torr
Laser	ArF excimer (193 nm)
Repetition frequency	1.0 Hz
Shot energy	90 mJ/cm^2/shot
Target-substrate distance	40–60 mm

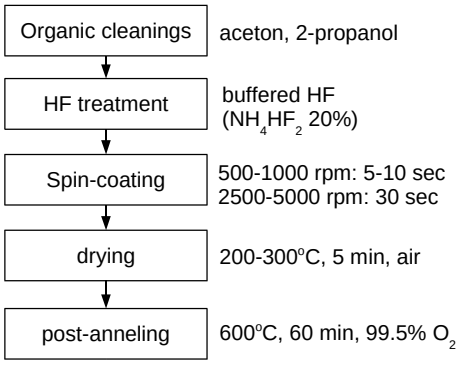

Figure 4.2: Flow chart of MOD process.

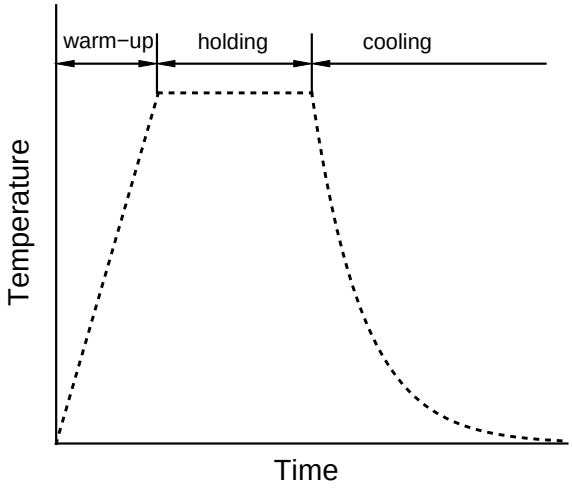

Figure 4.3: Control process of the sample temperature for RTA.

4.3 Excimer Laser Irradiation Effect

The samples were irradiated with ArF excimer laser light in air at room temperature. Figure 4.4 shows the electron spin resonance (ESR) spectra of HfO_2/Si structure with and without ArF laser irradiation. The peak around $g \simeq 2.003$ increases with the laser irradiation. It is considered that this peak arises from oxygen vacancy in the HfO_2 film, not from interface defects, since it is independent of the direction of the magnetic field [6]. From the ESR results (Fig. 4.4), the laser irradiation generated unpaired electrons induced by oxygen vacancy in the HfO_2 film. It is considered that the dangling bonds of Hf atoms are generated by the laser irradiation.

The *C*-*V* curves of the Al/HfO_2/Si structure with and without the laser irradiation are shown in Fig. 4.5. The *C*-*V* curves are normalized by accumulation capacitance of them. The *C*-*V* curves shift to the negative voltage direction. This result implies that the positive fixed charge in the HfO_2 film increases with the laser irradiation. From ESR and *C*-*V* measurement, it should be considered that the HfO_2 film becomes positively charged as a result of these dangling bonds.

Figure 4.6 shows PRS spectral intensity as a function of the number of laser shots. The intensity is normalized by the intensity of the as-deposited sample. The spectral intensity decreases with increasing number of laser shots. It is unlikely that the surface potential at HfO_2 film is changed by laser irradiation, so it is considered that PRS spectral intensity reflects amount of positive charge in the film.

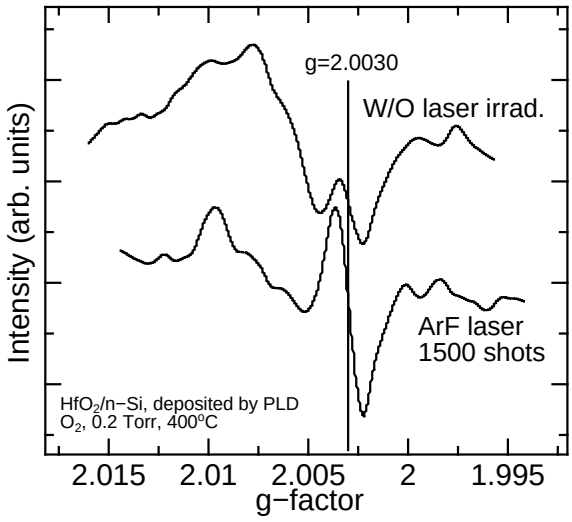

Figure 4.4: ESR spectra of HfO_2/Si structure without and with ArF laser irradiation.

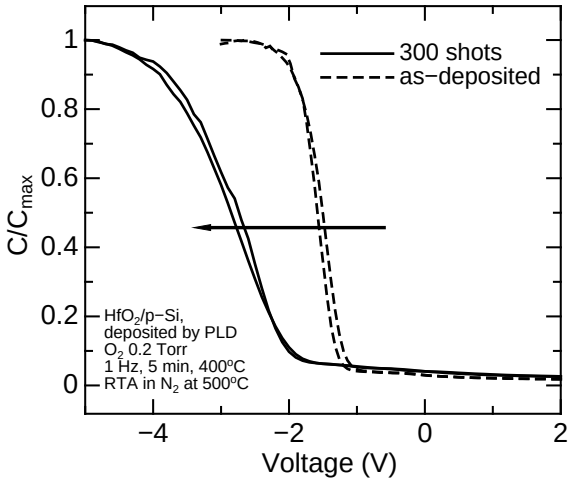

Figure 4.5: *C-V* curve of Al/HfO_2/Si with and without ArF laser irradiation.

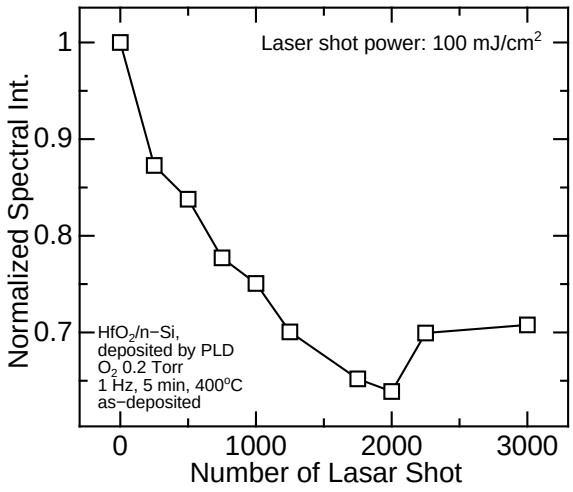

Figure 4.6: PRS spectral intensity as a function of number of laser shots normalized by PRS intensity of as-deposited sample.

4.4 HfO_2/Si Structure

4.4.1 Deposition Condition Dependence

HfO_2 thin films were deposited on Si substrate by PLD. The dependences on deposition atmosphere and on deposition temperature have been investigated.

Figure 4.7 shows the PRS spectra of HfO_2/Si structures deposited in O_2, N_2 and a mixture of these gases (O_2 : N_2 = 2 : 1) at 400°C. PRS spectral intensity depends on the deposition atmosphere. The positive fixed charges per unit area in the HfO_2 film calculated from a flat band voltage shift (ΔV_{FB}) of C-V curves and PRS spectral intensities are shown in Fig. 4.8. The positive charge in the HfO_2 film deposited in N_2 is larger than that in the HfO_2 film deposited in the other atmospheres. This larger positive charge is assumed to be caused by oxygen vacancy because HfO_2 film is deposited in reduced atmosphere. On the other hand, PRS spectral intensity of HfO_2/Si deposited in N_2 is smaller than that of HfO_2/Si deposited in the other atmospheres. PRS spectral intensity decreases with increasing positive charge, as discussed in § 4.3. Thus, the relationship between deposition atmosphere and positive charge in the film can be investigated by PRS.

The PRS spectral intensity of HfO_2/Si deposited in O_2 is smaller than that of HfO_2/Si deposited in the mixture gas in spite of smaller charge density of the former. Assuming that the potential at HfO_2 surface (V) is constant, PRS spectral intensity decreases with decreasing the dielectric constant or increasing film thickness for HfO_2 film, as shown in Fig. 2.18. Figure 4.9 shows the cross-sectional TEM images of HfO_2/Si deposited in (a) O_2 and (b) N_2 at 400°C. The interfacial layer growth is observed in the TEM image of HfO_2 deposited in O_2 (Fig. 4.9 (a)). Similar results are obtained by measurement of the XPS spectrum of Si 2p. The interfacial layer includes Si oxide so that it has lower dielectric constant than that of HfO_2. From these results, it is considered that a small PRS spectral intensity is caused by lower dielectric constant because of the interfacial layer growth.

Figure 4.10 shows dependence of PRS spectrum on HfO_2 deposition temperature. PRS spectral intensity increases with increasing deposition temperature. C-V characteristics of Al/HfO_2/Si deposited at temperatures 100, 200, 300 and 400°C are shown in Fig. 4.11. Although the flat band voltage shift scarcely changes with deposition atmosphere, the accumulation capacitance (the maximum capacitance of C-V curve) increases with increasing temperature. Figure 4.12 shows PRS spectral intensity and the maximum of C-V curve as a function of HfO_2 deposition temperature. It is found that there is correlationship between PRS spectral intensity and the maximum capacitance. The accumulation capacitance almost equal to capacitance of HfO_2 film. Assuming thickness of HfO_2 film is independent on deposition temperature, it should be considered that dielectric constant of HfO_2 film increases with deposition temperature. PRS intensity also increases with dielectric constant of HfO_2 film, as shown in Fig. 2.18. Figure 4.13 shows Si surface stress in

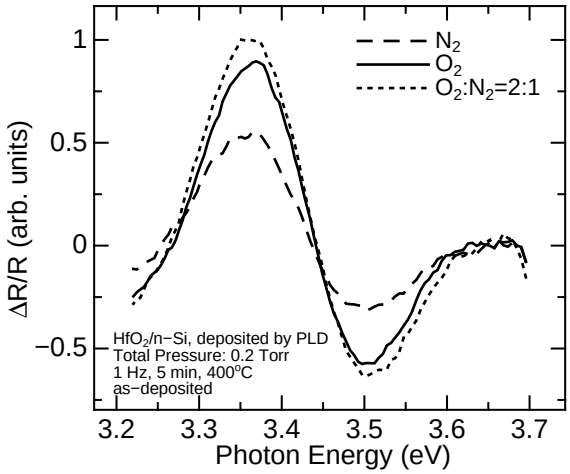

Figure 4.7: PRS spectra of HfO_x/Si deposited in O_2, N_2 and a mixture (O_2 : N_2 = 2 : 1) gas.

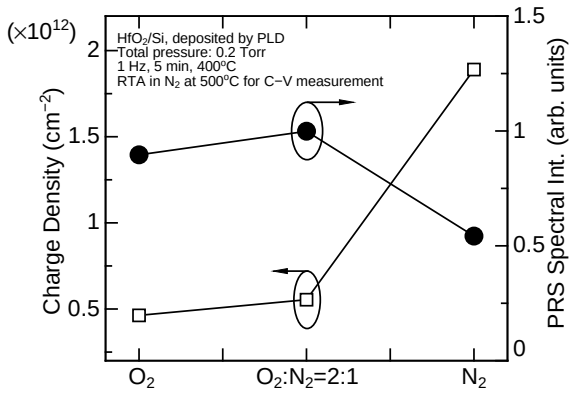

Figure 4.8: Fixed oxide charges and PRS spectral intensities of HfO_2/Si deposited in O_2, N_2 and N_2/O_2 mixture gas.

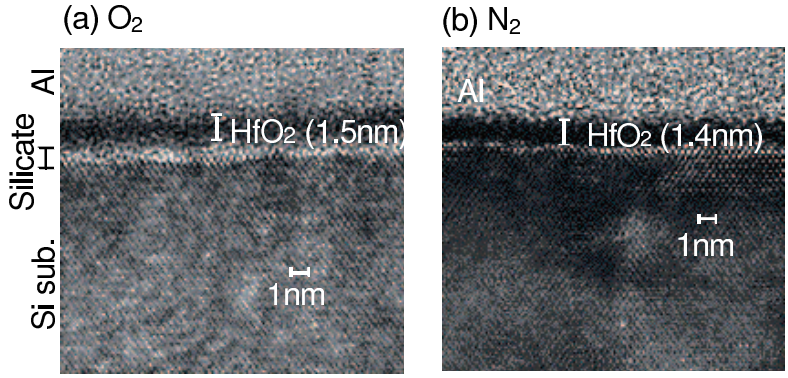

Figure 4.9: Cross-sectional TEM images of HfO_2/Si deposited in (a) O_2 and (b) N_2 at 400°C.

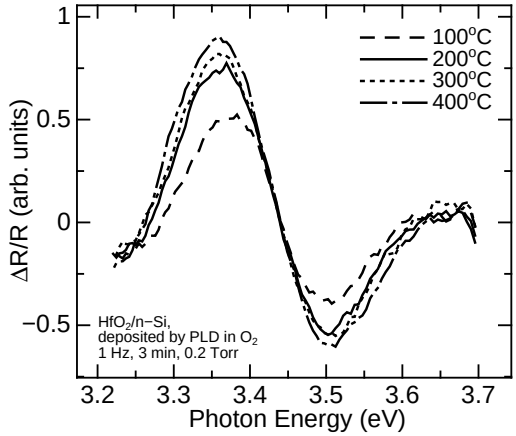

Figure 4.10: Dependence of PRS spectrum on HfO_2 deposition temperature.

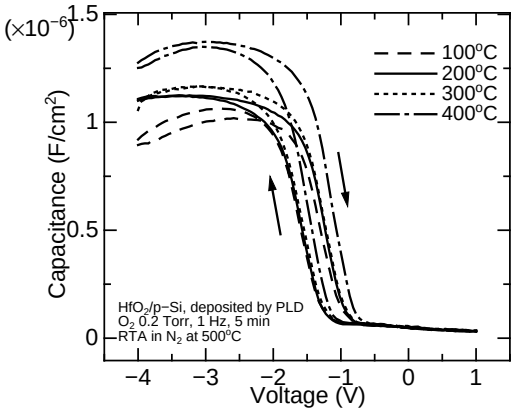

Figure 4.11: Dependence of the *C-V* characteristic on HfO_2 deposition temperature.

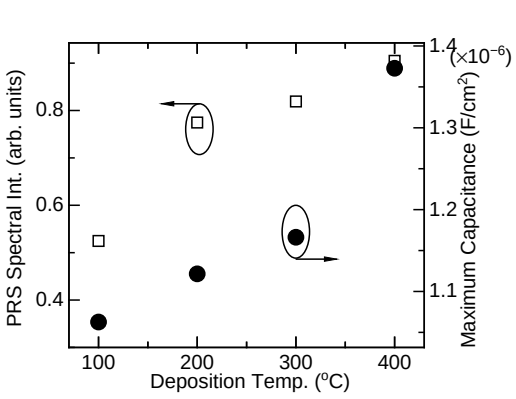

Figure 4.12: PRS spectral intensity and maximum capacitance of *C-V* curve as a function of HfO_2 deposition temperature.

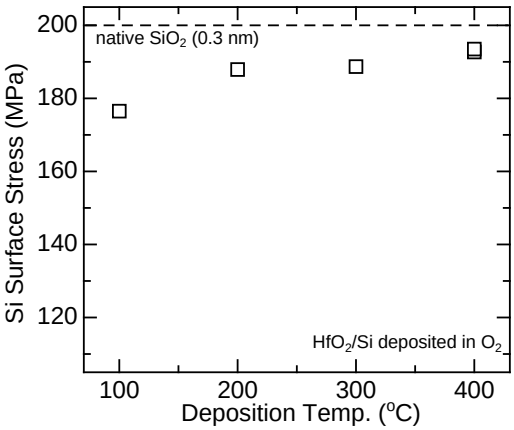

Figure 4.13: Si surface stress obtained from E_1 critical point of PRS spectra as a function of HfO_2 deposition temperature.

HfO_x/Si obtained by PRS curve fitting as a function of deposition substrate temperature. Dashed line in Fig. 4.13 shows the tensile stress value induced native oxide (0.3 nm) shown in Fig. 3.17. Although the tensile stress at Si surface slightly increases with increasing substrate temperature, it do not reach to the stress at interface between native oxide and Si. This result means that the interfacial layer growth is hardly observed for deposition at up to 400°C.

4.4.2 RTA Condition Dependence

PRS was utilized for the characterization of RTA in N_2, O_2 and a forming gas. The holding time for RTA was 0 sec.

The dependences of fixed charge density obtained from *C-V* curves and PRS spectral intensity

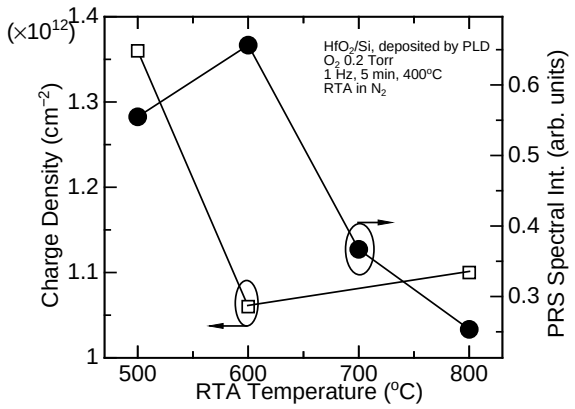

Figure 4.14: Dependences of fixed charge density and PRS spectral intensity on RTA temperature in N_2 atmosphere.

on RTA temperature in N_2 atmosphere are shown in Fig. 4.14. The PRS spectral intensity of the sample annealed at 600°C is larger than that of that annealed at 500°C for RTA in N_2. As discussed previously, PRS intensity decreases with increasing positive charge in the film. Therefore, it is suggested that the reduction in the number of positively charged defects in HfO_2 by RTA is found by PRS.

The spectral intensity rapidly decreases at 700°C and above for RTA in N_2. Figure 4.15 shows the XPS spectra of the Si $2p$ of HfO_2/Si structure treated by RTA in N_2. The signal from substrate at 99.4 eV [8] was used for the binding energy reference. The chemically-shifted peak (SiO_2: 103.4 eV [8]) of Si $2p$ rapidly increases at high temperatures. This result means that an interfacial layer (including Hf-silicate and SiO_2) grows by RTA at high temperatures. Similar results are obtained by TEM image. The decrease in PRS spectral intensity corresponds to an interfacial layer growth found by XPS measurement. It is considered that the spectral intensity decreases with decreasing dielectric constant of HfO_2, as shown in Fig. 2.18. It is suggested by these PRS results that suitable temperature for RTA in N_2 atmosphere of HfO_2/Si structure is 600°C.

Figure 4.16 shows the PRS spectral intensity of HfO_2/Si as a function of temperature of RTA in O_2 atmosphere. PRS spectral intensity has a similar temperature dependence to the case of RTA in N_2. Figure 4.17 shows XPS spectra of HfO_2/Si structure treated by RTA in O_2 atmosphere. The SiO_2 peak of Si $2p$ rapidly increases at high temperatures as well as N_2 RTA. The interfacial growth for O_2 RTA is larger than that for N_2 RTA. Therefore, the positive charge in HfO_2 film decreases by RTA in O_2 at up to 600°C and the interfacial layer growth occurs by RTA in O_2 above 700°C, so that it is considered that the suitable temperature for RTA in O_2 atmosphere of HfO_2/Si structure is also 600°C.

Figure 4.18 shows the PRS spectral intensity of HfO_2/Si as a function of temperature of RTA in the forming gas atmosphere. Although PRS spectral intensity has a similar temperature depen-

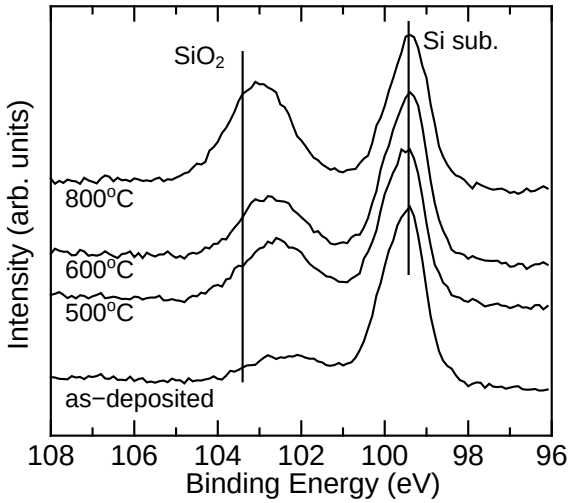

Figure 4.15: XPS Si 2*p* spectra of HfO_2/Si structure treated at 500, 600 and 800°C by RTA in N_2.

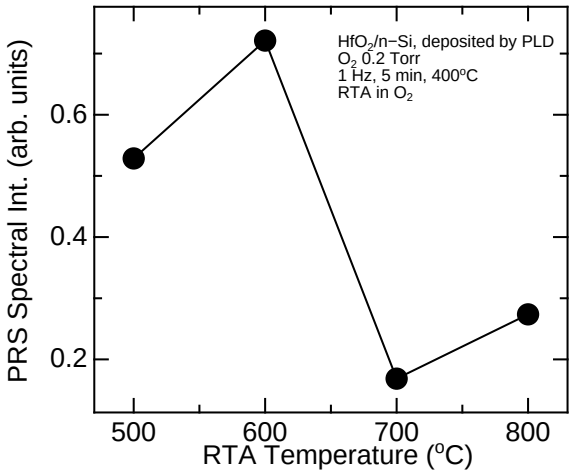

Figure 4.16: PRS spectral intensity as a function of temperature of RTA in O_2 atmosphere.

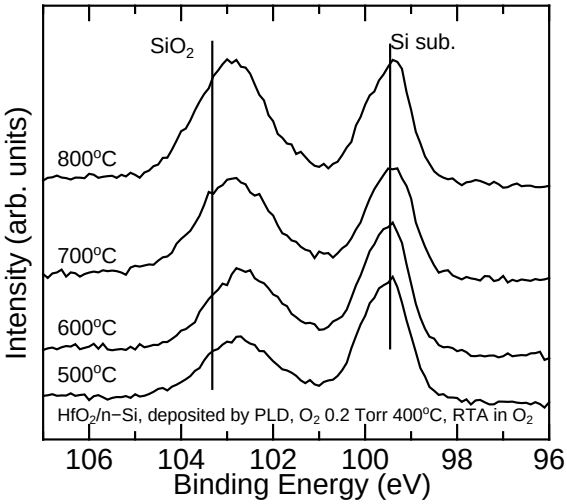

Figure 4.17: XPS Si 2*p* spectra of HfO_2/Si structure treated at 500, 600, 700 and 800°C by RTA in O_2 atmosphere.

dence to the case of RTA in N_2 and O_2, the increase in PRS intensity occurs at up to 500°C for RTA in the forming gas. Figure 4.19 shows XPS spectra of HfO_2/Si structure treated by RTA in the forming gas atmosphere. The chemically-shifted peak of Si 2*p* rapidly increases at 600°C and above. The increase in the area of an interfacial layer for forming gas RTA occurs at a lower temperature than those for the other atmospheres. Moreover, the chemically-shifted peak locates at a lower binding energy than SiO_2. This means that the composition of the interfacial layer grown by forming gas RTA is more silicate-like than that grown by O_2 and N_2 RTA. The forming gas is generally used for sintering of electrodes because of reducing behavior of H_2. So, it is considered that Hf oxide is reduced and then Hf-Si-O bond is formed by forming gas annealing. Anyhow, we can determine the suitable temperature for forming gas RTA 500°C by PRS spectral intensity.

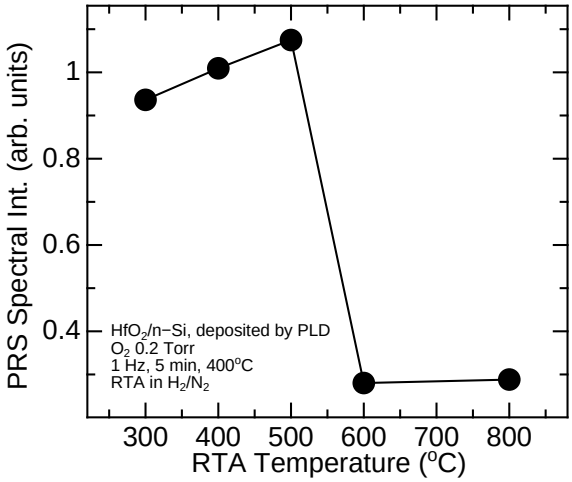

Figure 4.18: PRS spectral intensity as a function of temperature of RTA in the forming gas atmosphere.

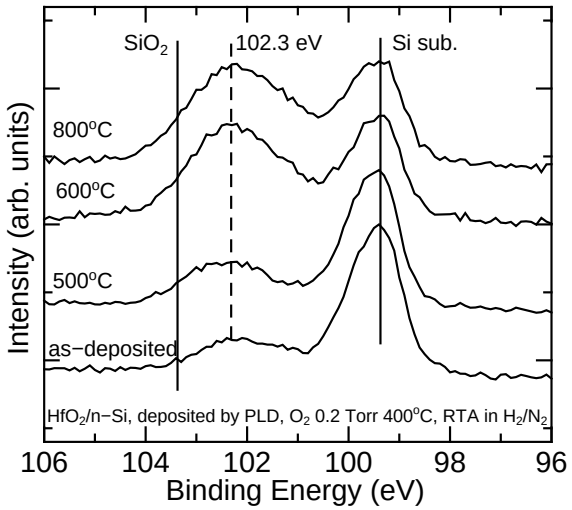

Figure 4.19: XPS Si 2*p* spectra of HfO_2/Si structure treated at 500, 600 and 800°C by RTA in the forming gas atmosphere.

4.5 PrO_x/Si Structure

4.5.1 Deposition Condition Dependence

Figure 4.20 shows PRS spectra of PrO_x/Si structure deposited in O_2 atmosphere (0.2 Torr) and high-vacuum (1×10^{-7} Torr). PRS spectral intensity of the sample deposited in O_2 atmosphere is larger than that deposited in high-vacuum. It is considered that PrO_x deposited in O_2 has less oxygen vacancy so that PRS spectral intensity is enhanced by less positive charges in the film. It is also found that PrO_x deposited in high-vacuum has large positive charges from flat band voltage shift of C-V curve [5].

Figure 4.21 shows PRS spectra of PrO_x/Si structure deposited at various substrate temperatures. PRS spectral intensity increases with deposition temperature. It is considered that PrO_x film deposited at higher temperature has higher dielectric constant because of higher film density observed by grazing incidence X-ray reflectometry (GIXR) [5]. Moreover, PRS spectrum seems to shift to low energy side for the sample deposited at high substrate temperature. Figure 4.22 shows Si surface stress in PrO_x/Si obtained by PRS curve fitting as a function of deposition substrate temperature. The tensile stress at Si surface significantly increases with increasing substrate temperature in sharply contrast to HfO_2 (Fig. 4.13). Dashed line in Fig. 4.22 shows the tensile stress value induced native oxide (0.3 nm) shown in Fig. 3.17. The stress value of PrO_x/Si deposited at higher temperature comes closer in this value. This result means that the interface between PrO_x and Si substrate becomes like SiO_2/Si. Figure 4.23 shows TEM image of PrO_x/Si structure deposited at 400°C. The interfacial layer growth is observed. From these results, it is considered that the interfacial layer which is like SiO_2 grows in the case of deposition at high substrate temperature, as shown in Fig. 4.24.

4.5.2 RTA Condition Dependence

PrO_x/Si structure deposited by PLD in O_2 atmosphere is treated by RTA. The holding time of RTA is for 1 min. The temperature and atmosphere of RTA are 400–800°C and O_2 gas, respectively.

Figure 4.25 shows dependence of PRS spectra of PrO_x/Si on RTA temperature. PRS spectral intensity is rapidly decreased by RTA above 600°C. XPS Si $2p$ spectra of these samples are shown in Fig. 4.26. The chemically-shifted peak corresponding to Si oxide is increased by RTA above 600°. It is considered that the interfacial layer including SiO_2 and silicate is significantly grown by high-temperature RTA. The interfacial layer has lower dielectric constant than PrO_x film so that effective dielectric constant of total film decreases. If dielectric constant decreases, PRS spectral intensity decreases as shown in Fig. 2.18. Figure 4.27 shows Si surface stress obtained from PRS spectra as a function of RTA temperature. Si surface stress is increased by RTA. Moreover, the stress induced by RTA at 600°C becomes like that of native SiO_2/Si. This result fortifies the

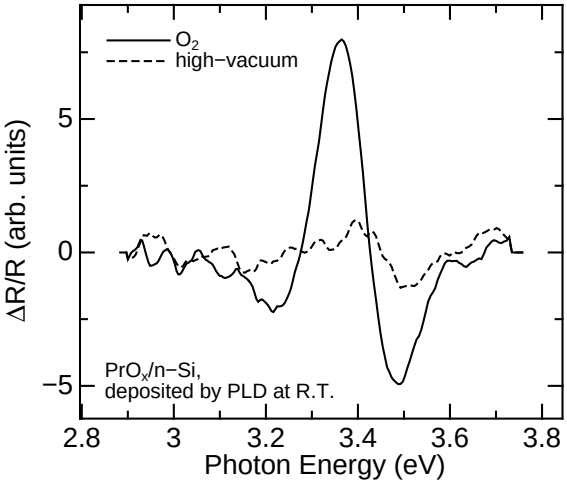

Figure 4.20: PRS spectra of PrO_x/Si structure deposited in O_2 atmosphere and high-vacuum.

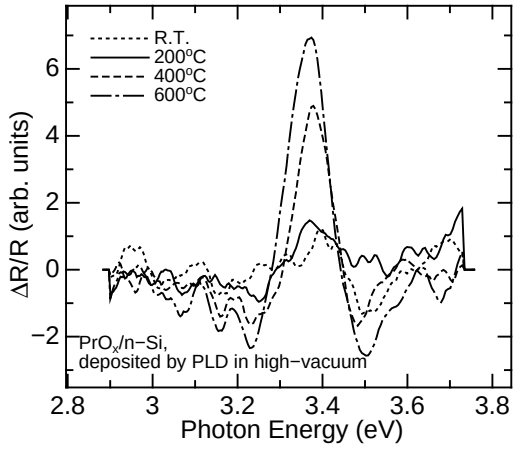

Figure 4.21: PRS spectra of PrO_x/Si structure deposited at room temperature, 200°C, 400°C and 600°C.

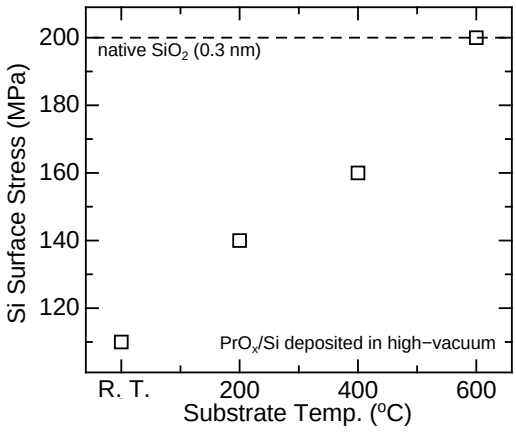

Figure 4.22: Si surface stress in PrO_x/Si obtained by PRS curve fitting as a function of deposition substrate temperature.

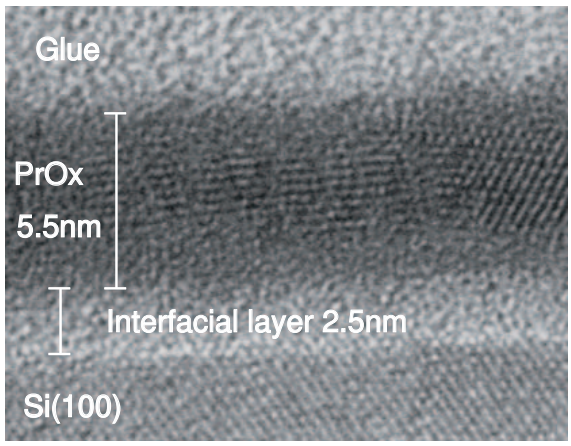

Figure 4.23: Cross-sectional TEM image of PrO_x/Si structure.

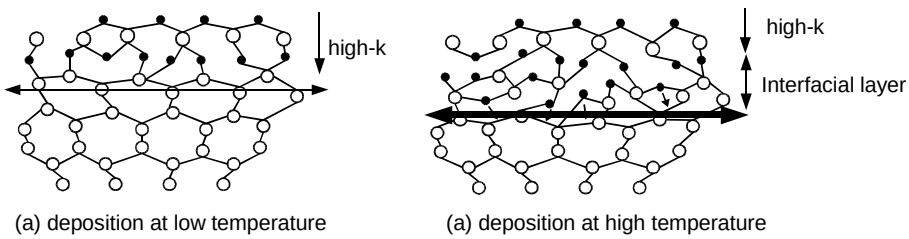

Figure 4.24: Model illustration of PrO_x/Si structure deposited (a) at low temperature and (b) at high temperature.

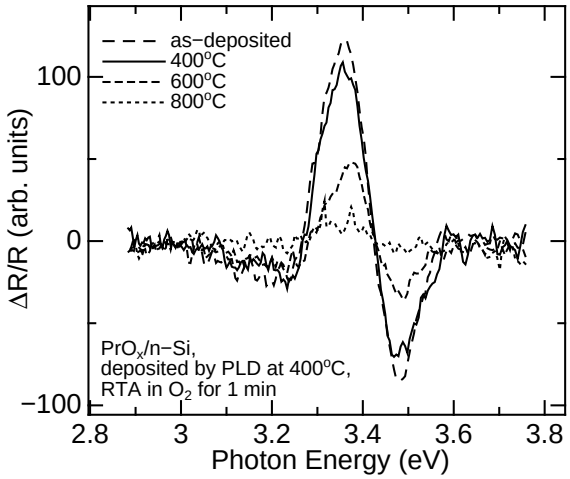

Figure 4.25: Dependence of PRS spectra of PrO_x/Si on RTA temperature.

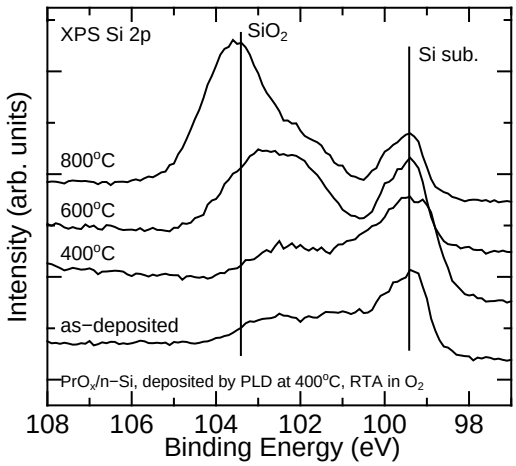

Figure 4.26: Dependence of XPS Si 2*p* spectra of PrO_x/Si on RTA temperature.

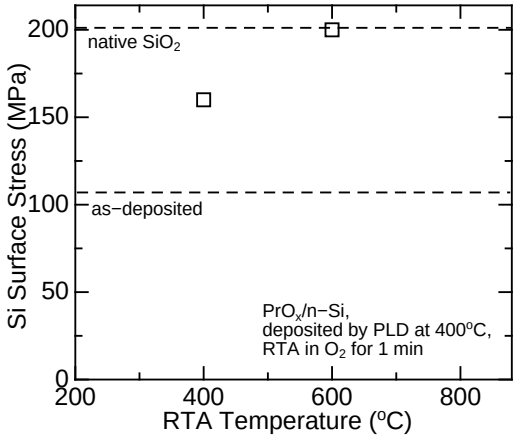

Figure 4.27: Si surface stress obtained from PRS spectra as a function of RTA temperature.

interfacial layer growth by RTA at high temperature.

4.6 Other High-k Materials

ZrO_2, Al_2O_3 and La_2O_3 were characterized except HfO_2 and PrO_x as described above. Their films were deposited on Si substrate by MOD. Figure 4.28 shows the dependence of PRS spectra on ZrO_2 thickness. PRS spectral intensity and Si surface stress obtained from PRS spectrum as a function of ZrO_2 thickness are shown in Fig. 4.29. PRS spectral intensity decreases with increasing ZrO_2 thickness. This result can be explained by Fig. 2.18. Moreover, PRS spectrum has the large spectral intensity compared with SiO_2 in spite of thick film (cf. Fig. 3.23). This large intensity is caused by high dielectric constant of ZrO_2 film. Si surface stress decreases with increasing ZrO_2 thickness. This result means that Si surface stress is reduced in the case of thick ZrO_2 film.

Figure 4.30 shows PRS spectra of Al_2O_3/Si, ZrO_2/Si and La_2O_3/Si deposited by MOD. The film thickness of these films is about 40 nm. Despite lowest dielectric constant ($\sim$ 11 [10]), PRS spectral intensity of Al_2O_3/Si is the largest among them. Generally, Al_2O_3/Si interface almost always has a high density of negative fixed charges [11]. If the negative charge exists in the insulator film, PRS spectral intensity increases contrary to the case of positive charge existence. Thus, very large PRS spectrum is measured for Al_2O_3/Si. On the other hand, PRS spectrum for La_2O_3/Si is very small in spite of high dielectric constant ($\sim$ 25–30 [10]). Although his origin is not known, it is assumed that there is the large positive charge in La_2O_3 film or large interface level as the recombination center of modulation carries at La_2O_3/Si interface.

4.7 Summary

The high-k thin film/Si structures have been characterized by PRS. From excimer laser irradiation effect, it is found that PRS spectral intensity decreases with increasing the positive charge in high-k films.

HfO_2 deposited in N_2 atmosphere has large amount of positive charges found by smaller PRS spectral intensity. PRS spectral intensity depends on deposition temperature of both HfO_2 and PrO_x films. This result means that dielectric constant of these films increases with increasing deposition temperature because these films are densified. The Si surface stress hardly depends on deposition temperature in the case of HfO_2. On the other hand, Si surface tensile stress of PrO_x/Si slightly increases with deposition temperature.

PRS spectral intensity of HfO_2/Si increases with RTA treatment at temperatures up to 600°C in N_2 and O_2 atmosphere. Above 700°C, the spectral intensity decreases contrarily. This decrease is caused by a decrease in the dielectric constant of the film with the interfacial layer growth observed by XPS spectra. Similar results are obtained for PrO_x films, but decrease of PRS spectral intensity occurs at 600°C and above. It is considered that HfO_2 is more thermally-stable than

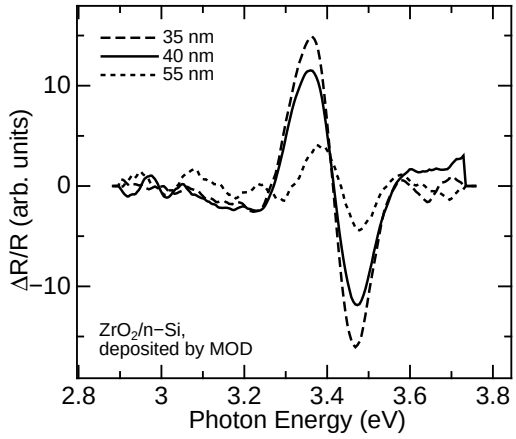

Figure 4.28: PRS spectra of ZrO_2/Si structures with ZrO_2 films of various thicknesses, 35, 40 and 55 nm.

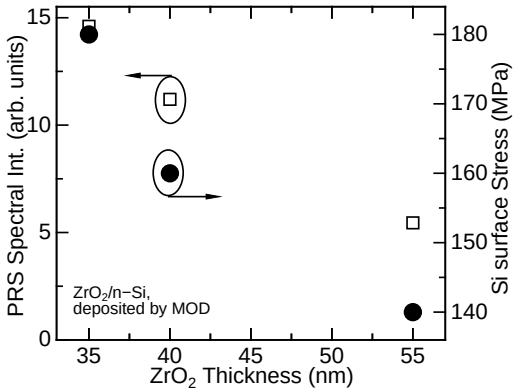

Figure 4.29: PRS spectral intensity (open square) and Si surface stress (closed circle) obtained from PRS spectrum as a function of ZrO_2 thickness.

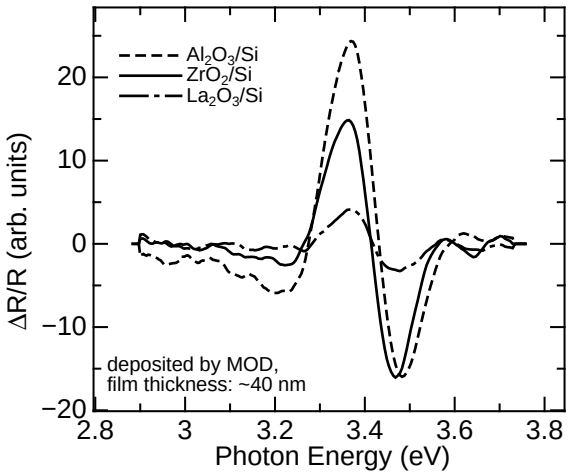

Figure 4.30: PRS spectra of Al_2O_3/Si, ZrO_2/Si and La_2O_3/Si. The film thickness is about 40 nm.

PrO_x.

The other high-*k* materials have been also characterized. PRS spectral intensity and Si surface stress of ZrO_2/Si decrease with increasing ZrO_2 thickness. Al_2O_3/Si structure has large PRS spectral intensity because of large amount of negative charge in Al_2O_3 film. On the other hand, La_2O_3/Si has small spectral intensity in spite of similar thickness, because La_2O_3 assumably has large positive charge or large interface level.

Reference

[1] T. Kanashima: Dr. Thesis, Faculty of Engineering Science, Osaka University, Osaka, 1996.

[2] M. Niwa: Oyo Buturi **72** (2003) 1143 [in Japanese].

[3] K. Sekine, S. Inumiya, A. Kaneko, M. Sato, I. Hirano, T. Yamaguchi, K. Eguchi and Y. Tsunashima: Oyo Buturi **73** (2004) 1200 [in Japanese].

[4] S. Ohmi, C. Kobayashi, I. Kashiwagi, C. Ohshima, H. Ishiwara and H. Iwai: J. Electrochem. Soc. **150** (2003) F134.

[5] S. Kitai, O. Maida, T. Kanashima and M. Okuyama: Jpn. J. Appl. Phys. **42** (2003) 247.

[6] T. Kanashima, K. Ikeda, T. Tada, M. Sohgawa and M. Okuyama: to be published in J. Korean Phys. Soc.

[7] S. M. Sze, *Physics of Semiconductor Devices* (Wiley, New York, 1981), 2nd ed., p. 368.

[8] *X-sen Koudenshi Bunkouhou* (X-ray Photoelectron Spectroscopy), ed. The Surface Science Society of Japan (Maruzen, Tokyo, 1998) p. 218 [in Japanese].

[9] *Handoutai Hyouka Gijutsu* (Characterization Techniques of Semiconductors), ed. T. Katoda (Sangyotosho, Tokyo, 1989) p. 142–146 [in Japanese].

[10] A. I. Kingon, J. P. Maria, D. Wicaksana and C. Hoffman: *Ext. Abstr. Int. Workshop Gate Insulator* (Business Center for Academic Societies Japan, Tokyo, 2001) p. 36.

[11] R. S. Johnson, G. Lucovsky and I. Baum: J. Vac. Sci. Technol. A **19** (2001) 1353.

Chapter 5

Characterization of MFIS Structure

5.1 Introduction

As described in § 1.1.2, MFIS-FET type FeRAM has been expected to be a next-generation memory. As prospective materials for ferroelectric layer of MFIS structure, $SrBi_2Ta_2O_9$ (SBT) thin films have attracted much interest recently [1]. The SBT has Bismuth-layered structure and less fatigue degradation than $Pb(Zr,Ti)O_3$ (PZT) [2–4]. However, the retention property of remanent polarization of SBT film is not so good [2,5–8]. Searching of the suitable deposition and annealing parameters is fundamental to improve retention property. In this chapter, SBT/SiO_2/Si structures are characterized by PRS. PRS allows quick and damage-free characterization of memorized states of SBT/SiO_2/Si structure without electrode formation.

5.2 Sample Preparation and Characterization

After RCA cleaning and removing native oxide, n-type Si (100) wafers ($\rho \sim 0.02\ \Omega$ cm) were oxidized in O_2 atmosphere at 700°C. Then SBT films (200–500 nm) were deposited by MOD method. The precursor solution (Kojundo Y-1 type O) was coated on SiO_2/Si by the spin-coater. The samples were dried at 200°C and baked at 400°C in air, These processes were repeated to obtain the film of desired thickness (4–8 times). Finally, the samples were post-annealed in O_2 atmosphere at 500–1000°C for 10–30 min. For C-V measurement, Au top electrode and AuSb bottom electrode were deposited by vacuum evaporation (Ulvac VPC-260F). The base vacuum chamber pressure is about 2×10^{-6} Torr. The size of top electrode is about 0.15 mm ϕ. The detailed preparation process of MFIS structure is shown Fig. 5.1.

The structural property of the samples was characterized by X-ray diffraction (XRD; Rigaku RINT2000). The diffracted X-ray from Cu Kα radiation source was counted through 0.15 mm slit plate. The SBT film thickness was measured by ellipsometer.

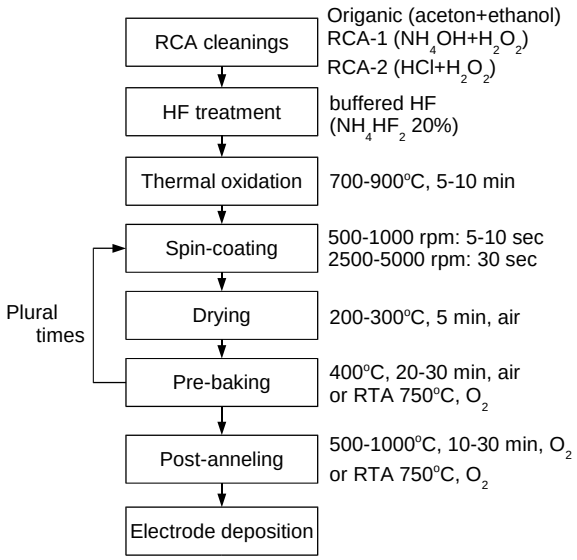

Figure 5.1: Flow chart of preparation process of MFIS structure.

5.3 PRS Spectrum of FIS Structure

Figure 5.2 shows PRS spectra of SiO_2 and SBT/SiO_2/Si stacked structures. The film thickness of SiO_2 and SBT are about 15 nm and 400 nm, respectively. It is found that PRS spectral intensity is enhanced by deposition of SBT film. Figure 5.3 shows XRD patterns of SBT films post-annealed at 600–900°C in O_2 atmosphere for 10 min. The XRD peak at $2\theta = 29.0°$ indicates (115) peak of bismuth-layered ferroelectric SBT [9]. SBT (115) peak is well found above 700°C. Figure 5.4 shows PRS spectral intensity and the intensity of (115) XRD peak as a function of post-annealing temperature. It is considered that PRS spectral intensity increases with the ferroelectricity of SBT film, and Si surface potential is increased by spontaneous polarization of SBT film.

Figure 5.5 shows PRS spectra of SBT/SiO_2/Si structures films which have various SBT thickness. The spectral shape significantly varies with SBT thickness. The SBT film is thick (> 100 nm) and has large refractive index ($\sim$ 2.3 [10]) so that it may be considered that the phase of PRS spectrum changes with thickness. However, it seems that the spectral shape change of measured PRS spectrum is more drastic than that of calculated one. The SBT film is not transparent perfectly (transmittance: 20–50% [10]) at spectral range of measured PRS spectrum, so the refractive index has the imaginary part. Moreover, the transmittance depends on photon energy. Therefore, it is considered that the spectral shape change of measured PRS spectrum do not agree well than that of calculated one.

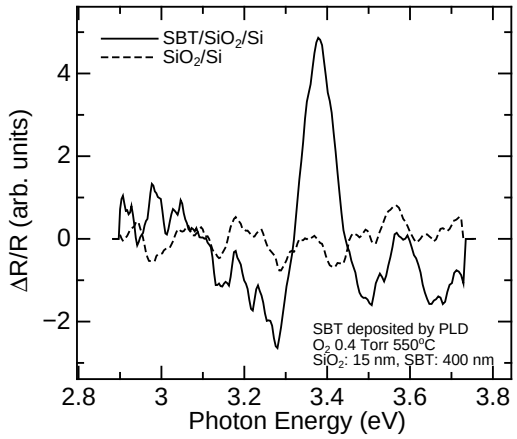

Figure 5.2: PRS spectra of SiO_2/Si and SBT/SiO_2/Si structures.

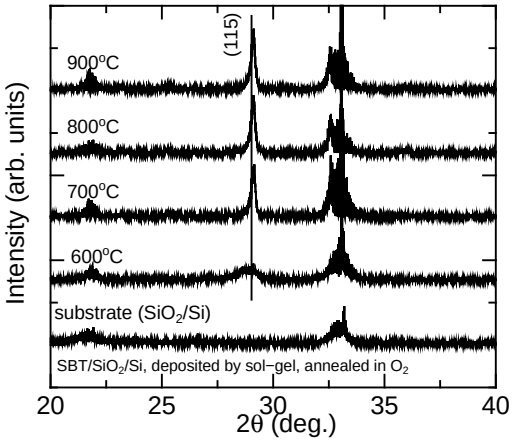

Figure 5.3: XRD patterns of SBT/SiO_2/Si structures annealed at different temperatures. SBT thin films were deposited by sol-gel method.

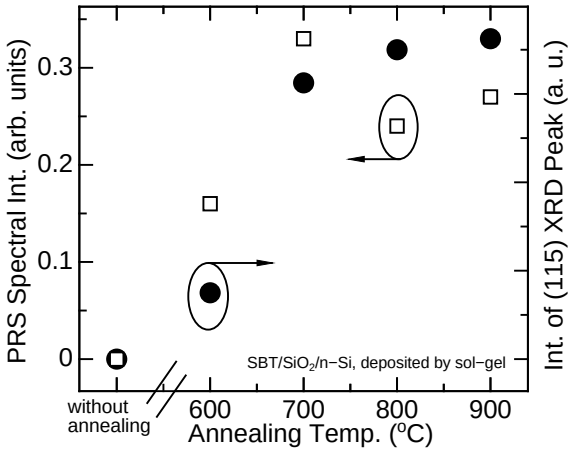

Figure 5.4: PRS spectral intensity and XRD intensity of (115) peak as a function of post-annealing temperature.

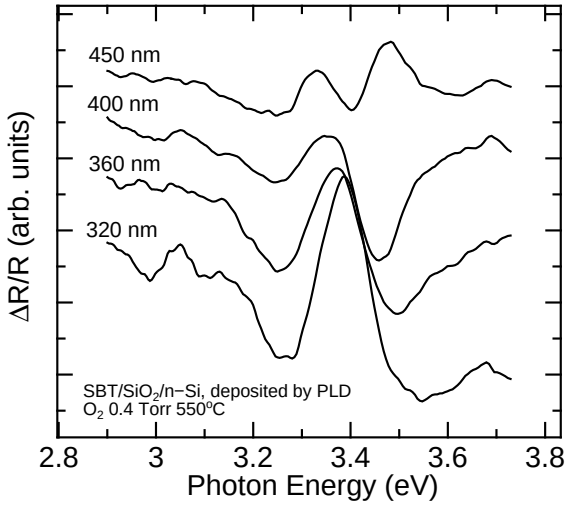

Figure 5.5: PRS spectra of SBT/SiO_2/Si structures with various SBT thickness.

5.4 Memorized States of MFIS Capacitor

To characterize of memorized states of SBT/SiO_2/Si structures, it was poled by DC voltage without electrode. The bottom of the sample (with native oxide) was grounded during poling process. After poling of SBT film, SBT/SiO_2/Si structure was measured by PRS, as shown in Fig. 5.6.

5.4.1 Poling Effect

Figure 5.7 shows PRS spectra of poled SBT/SiO_2/Si structure. PRS spectral intensity greatly increases by -3 V poling. PRS spectral intensity as a function of applied poling voltage is shown in Fig. 5.8. The spectral intensity has exponential dependence on poling voltage. If negative voltage is applied, Si surface potential is enlarged by remanent polarization in SBT layer, as solid line in Fig. 5.9, so that PRS spectral intensity increases as shown by eq. (2.103).

PRS spectral intensity of PRS also depends on modulation laser power P_m (eq. (2.103)). The Si surface potential Ψ_s can be estimated by the experimental data with theoretical curve of eq. (2.103). Figure 5.10 shows PRS spectral intensity as a function of power of modulation light (open square) and fitted curve (dashed line) using by eq. (2.103). The theoretical curve is well fitted to experimental data. Si surface potential obtained by curve fitting is shown in Fig. 5.11. Si surface potential linearly increases with increasing negative poling voltage. The increase of Si surface potential by -1 V poling is 0.17 eV.

Figure 5.12 shows PRS spectra normalized by peak intensity of negative poled SBT/SiO_2/Si. The shift to low energy side of PRS spectrum increases with increases negative poling voltage. Figure 5.13 shows E_1 critical point obtained by curve fitting of PRS spectrum and Si surface stress calculated using eq. (3.10) as a function of poling voltage. E_1 linearly decreases with increasing negative poling voltage. This result means increase of tensile stress at Si surface. The SBT film has not only ferroelectricity but also piezoelectricity. The relationship between electric displacement D (= P_s: remanent polarization) and stress T of SBT film without external electric

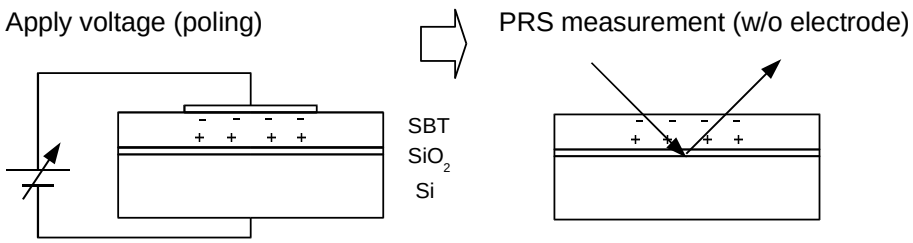

Figure 5.6: Sample measurement structures of memorized states of SBT/SiO_2/Si with and without electrodes.

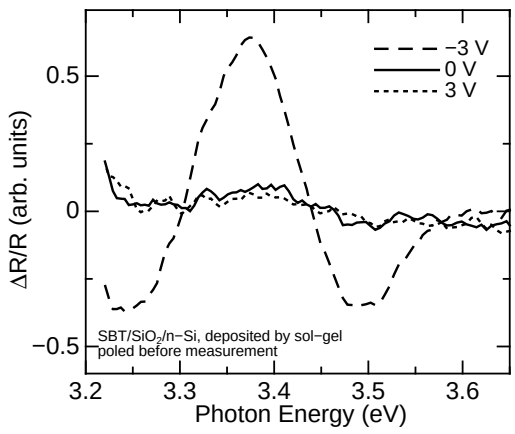

Figure 5.7: PRS spectra of poled $SBT/SiO_2/Si$ structure.

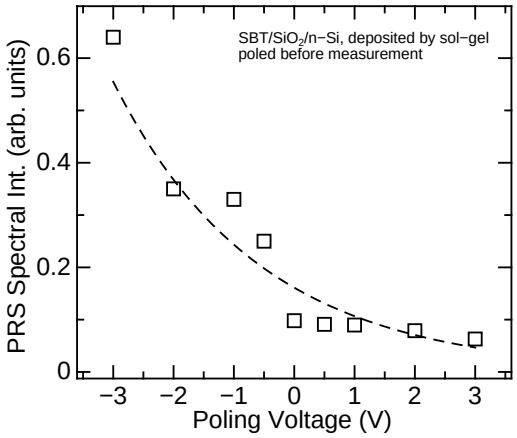

Figure 5.8: PRS spectral intensity as a function of poling voltage.

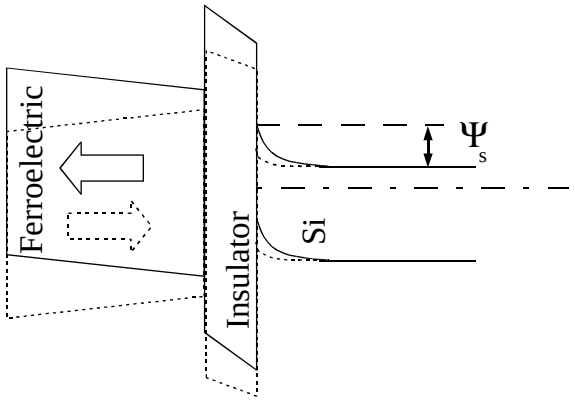

Figure 5.9: Band diagram of FIS structure. The arrows in ferroelectric layer express direction of remanent polarization. Solid line shows the case of negative polarization and dashed line shows the case of positive polarization.

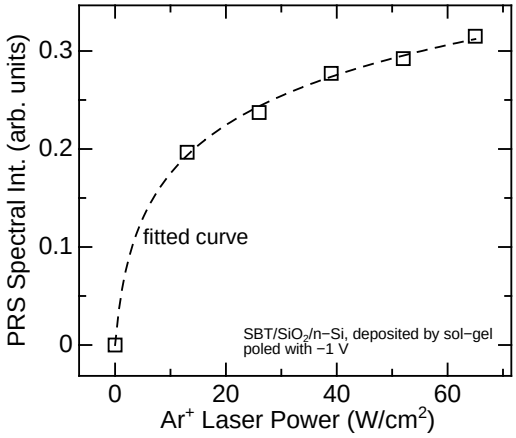

Figure 5.10: PRS spectral intensity as a function of power of modulation light (open square) and fitted curve (dashed line) calculated by using eq. (2.103).

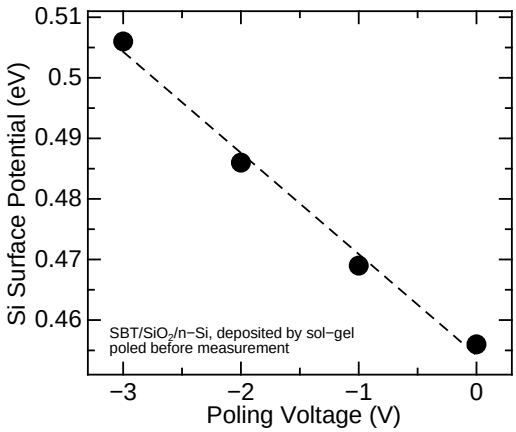

Figure 5.11: Si surface potential obtained from PRS spectra as a function of poling voltage.

field is expressed as a following equation [11],

$$D = P_s = dT, \tag{5.1}$$

where d is piezoelectric constant. It is considered that Si surface stress is increased by piezoelectric effect of SBT film throughout SiO_2 layer. The poling at -3 V induces tensile stress of ~ 30 MPa.

Figure 5.14 shows the Raman spectra of SBT/SiO_2/Si structure poled at -5 V and 0 V. The peak shift of Raman spectra is hardly observed. This result means that the small stress induced by ferroelectric layer which cannot be observed by Raman spectroscopy can be characterized by PRS spectra.

5.4.2 Retention Property

The retention property of memory of SBT/SiO_2/Si structure was characterized by utilizing PRS. The time dependence of PRS spectrum of SBT/SiO_2/Si structure after poling -5 V and hold at 0 V is shown in Fig. 5.15. PRS spectral intensity gradually decreases after poling. Figure 5.16 shows the time dependence of difference of retained capacitances of SBT/SiO_2/Si witten at +5 V and -5 V (open square), and the time dependence of PRS spectral intensity (close circle). It is found that these time dependencies show the same tendencies. Si surface potential decreases with decreasing charge injection or the remanent polarization in SBT film. Therefore, it is considered that PRS spectral intensity in Fig. 5.16 reflects retention property of SBT film so that retention property of MFIS structure can be characterized by contactless measurement of PRS spectral intensity.

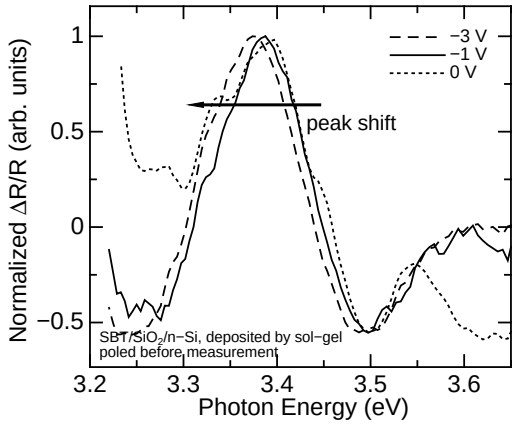

Figure 5.12: PRS spectra normalized by peak intensity of negative poled $SBT/SiO_2/Si$.

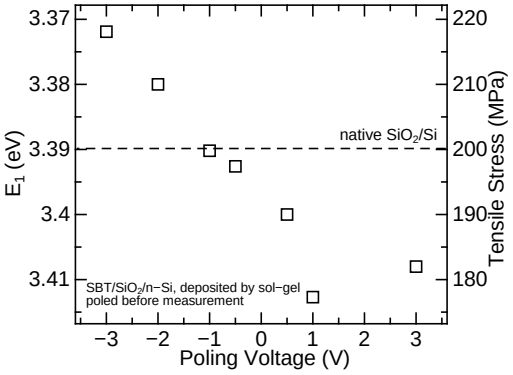

Figure 5.13: E_1, transition energy at critical point obtained from PRS spectrum as a function of poling voltage.

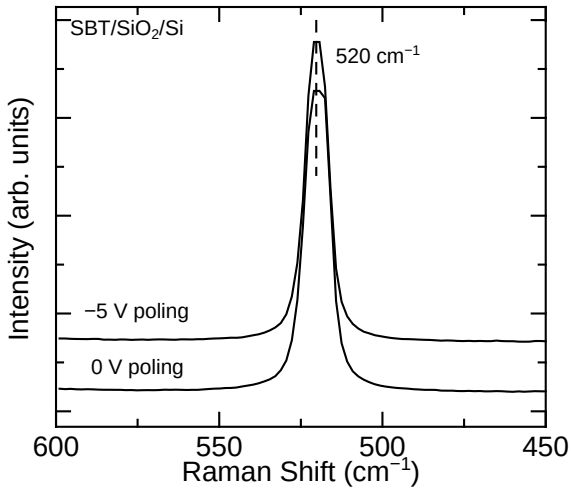

Figure 5.14: Raman spectroscopy of $SBT/SiO_2/Si$ structure poled at −5 V and 0 V.

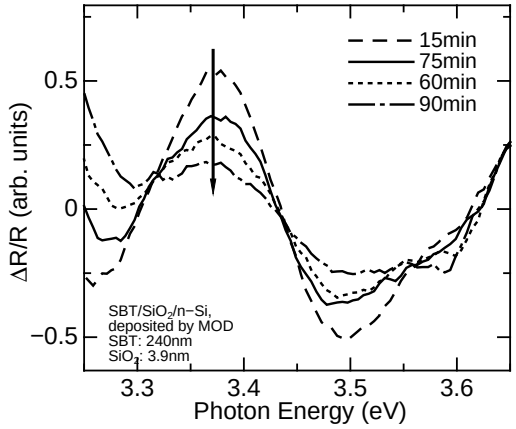

Figure 5.15: Time dependence of PRS spectrum of $SBT/SiO_2/Si$ structure. Writing (poling) voltage is −5 V and holding voltage is 0 V.

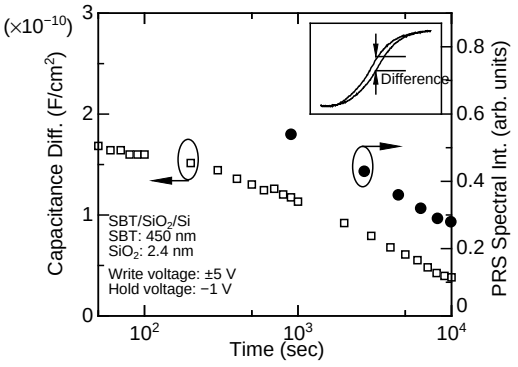

Figure 5.16: Time dependence of retained capacitance of $SBT/SiO_2/Si$ (open square), and the time dependence of PRS spectral intensity (close circle).

It has been reported that the memory retention property of $SBT/SiO_2/Si$ is significantly improved by RTA after deposition [7]. And the crystallographic structure of SBT [12] and (Bi, La)$_4$Ti$_3$O$_{12}$ (BLT; has Bi layered structure as well as SBT) [13] thin film is also improved by RTA for each spin-coated layer (layer-by-layer RTA). Consequently, we have confirmed the improvement of retention property of $SBT/SiO_2/Si$ structure by layer-by-layer RTA using PRS. RTA process were performed after spin-coating and drying for 30 sec (see § 5.1). The post-annealing also performed in RTA furnace for 30 min. The atmosphere and temperature of RTA were O_2 and 750°C, respectively. Figure 5.17 shows PRS spectral intensity of $SBT/SiO_2/Si$ deposited by conventional process (open square) and that deposited by layer-by-layer RTA process (close circle). The decrease of PRS spectral intensity for layer-by-layer RTA is obviously smaller than that for conventional process. It is considered that improvement of memory retention property of $SBT/SiO_2/Si$ structure is observed by PRS measurement without electrode formation.

5.4.3 Characterization of Hysteresis without Electrode Formation

To apply voltage during PRS measurement, a plate glass with indium tin oxide (ITO) transparent electrode was firmly attached to the sample, as shown in Fig. 5.18. Thickness of ITO film is about 200 nm.

Figure 5.19 shows the dependence of PRS spectra on applying voltage after ±5 V poling. The spectral intensity depends on the direction (plus or minus) of poling voltage. (the intensity with applying 0 V after −5 V poling is larger than that after +5 V poling). Figure 5.20 shows applied voltage dependence of PRS spectral intensity after ±5 V poling. The spectral intensity has a clockwise hysteresis loop. The C-V curve of $Au/SBT/SiO_2/Si$ is shown in Fig. 5.21. The curve

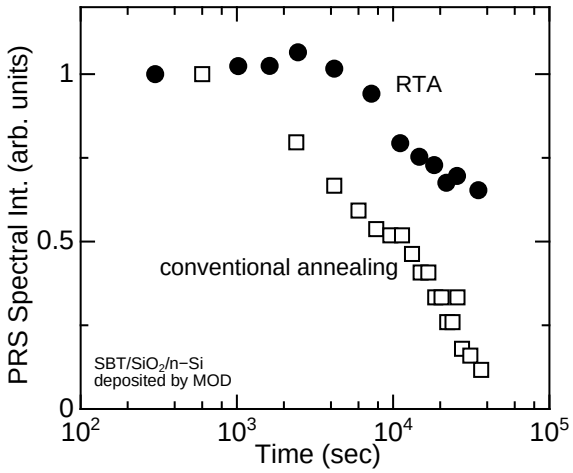

Figure 5.17: PRS spectral intensity of SBT/SiO_2/Si deposited by conventional process (open square) and that deposited by layer-by-layer RTA process (close circle).

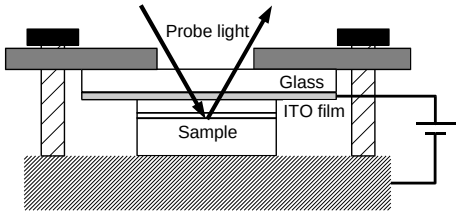

Figure 5.18: PRS measurement with attaching ITO transparent electrode.

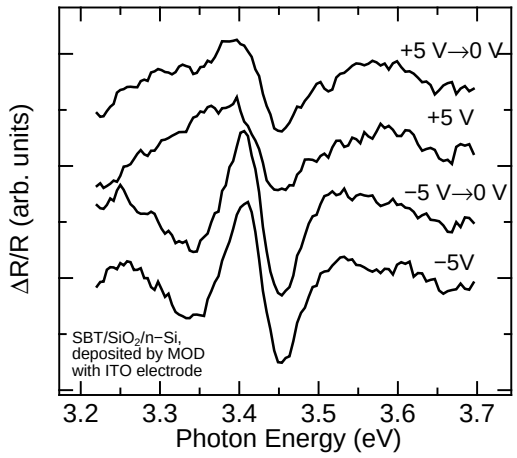

Figure 5.19: Dependence of PRS spectra on applying voltage after ±5 V poling.

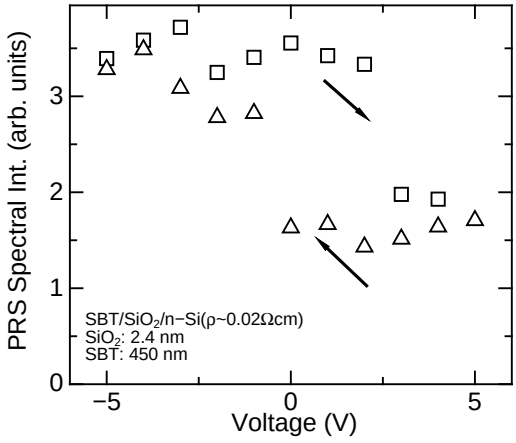

Figure 5.20: Applied voltage dependence of PRS spectral intensity. Open squares show the case after −5 V poling and open triangles show the case after +5 V.

shows a counterclockwise hysteresis loop which signifies the ferroelectricity. The hysteresis of PRS spectral intensity has reverse loop toward *C-V* curve.

The *D-E* hysteresis loop of ferroelectric is expressed by Miller's equation [14].

$$D_{\rm sat}^{\pm} = \pm P_s \tanh\left[\frac{\pm E - E_c}{2\delta}\right] + \varepsilon_0 \varepsilon_f E, \tag{5.2}$$

where

$$\delta = E_c \left[\ln\left(\frac{1 + P_r/P_s}{1 - P_r/P_s}\right)\right]^{-1}, \tag{5.3}$$

P_r and P_s are the remanent polarization and spontaneous polarization, E_c is coercive force, and ε_f is the ferroelectric linear dielectric constant. Hence, capacitance of ferroelectric layer (thickness: d_f) is expressed as follows,

$$\begin{aligned} C_f^{\pm} &= \frac{dD}{dE}\frac{1}{d_f} \\ &= P_s \frac{1}{2\delta}\mathrm{sech}^2\left[\frac{\pm E - E_c}{2\delta}\right] + \varepsilon_0 \varepsilon_f. \end{aligned} \tag{5.4}$$

Assuming that there is no charge at interfaces and in insulator film, electric density is continuous through MFIS stack from Gauss' low [15]. So, the space charge density at Si surface (Q_s) expressed by eq. (2.106) equals to $D_{\rm sat}^{\pm}$. The capacitance of MFIS structure is obtained by

$$C = \left(\frac{1}{C_f} + \frac{1}{C_i} + \frac{1}{C_D}\right)^{-1}, \tag{5.5}$$

where C_i and C_D are capacitances of insulator (thickness: d_i) and dipletion layer of Si surface, respectively [16],

$$C_i = \frac{\varepsilon_i}{d_i} \tag{5.6}$$

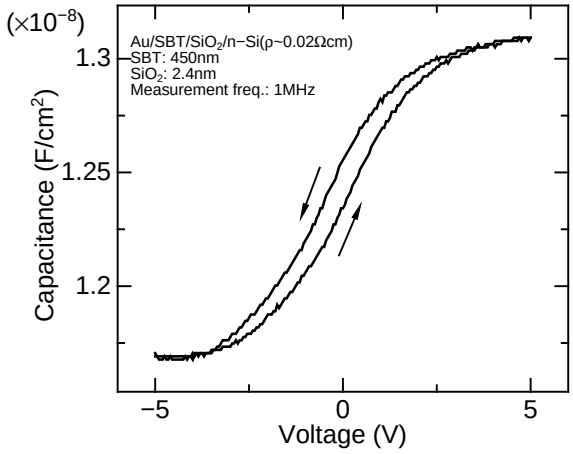

Figure 5.21: C-V curve of Au/SBT/SiO_2/Si diode.

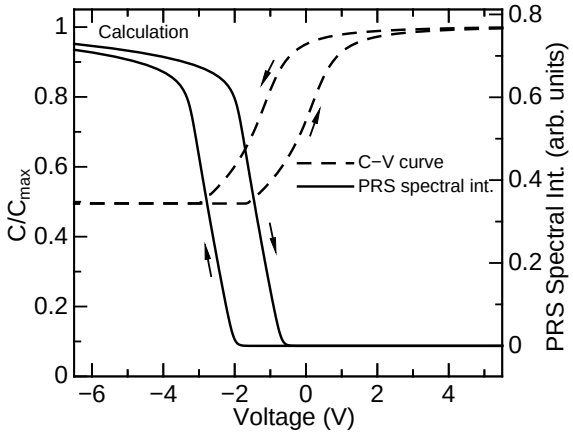

Figure 5.22: Calculated C-V curve and PRS spectral intensity as a function of applied voltage.

$$C_D = \frac{\partial Q_s}{\partial \Psi_s} = \frac{\varepsilon_s}{\sqrt{2}L_D} \frac{1 - e^{-\frac{\Psi_s}{kT}} + \frac{p}{n}\left(e^{\frac{\Psi_s}{kT}} - 1\right)}{F(\Psi_s)}, \tag{5.7}$$

and $F(\Psi_s)$ is expressed by eq. (2.107). C-V curve can be calculated by using eqs. (2.108) and (5.5). PRS spectral intensity can be calculated by obtaining Ψ_s from eq. (5.7) and substituting Ψ_s to eq. (2.103).

Figure 5.22 shows calculated C-V curve and PRS spectral intensity as a function of applied voltage. The values used for calculation are shown Table 5.1. The directions of hysteresis are same as measured data (Figs. 5.20 and 5.21). Therefore, it is considered that the hysteresis loop of PRS spectral intensity reflects ferroelectricity of SBT film as well as C-V curve.

Table 5.1: Conditions for calculation of MFIS structure.

Ferroelectric layer	
E_c	35 kV/cm
P_r	10 μC/cm^2
P_s	12 μC/cm^2
ε_f	248
Insulator layer	
ε_i	3.9

5.5 Summary

SBT/SiO_2/Si structures have been characterized by PRS. PRS spectral intensity increases by deposition of SBT film because of spontaneous polarization in SBT film. PRS spectral intensity is closely related to SBT (115) peak intensity in XRD pattern. It is considered that PRS spectrum reflects the ferroelectricity of SBT film.

PRS spectral intensity linearly increases with negative poling voltage because of Si surface potential is enlarged by remanent polarization in SBT. The holding time dependence of PRS spectral intensity is measured. PRS spectral intensity gradually decreases as well as capacitance difference of *C-V* curve. Moreover, decrease of PRS spectral intensity is reduced by introduce of RTA process. It is considered that the memory retention property of SBT/SiO_2/Si can be characterized by time dependence of PRS spectral intensity.

The spectral intensity reflects hysteresis characteristic of SBT/SiO_2/Si structure. From these results, it is considered that PRS can be applied to characterization of ferroelectricity in MFIS structures as a cotactless measurement.

Reference

[1] M. Takahashi: Dr. Thesis, Graduate School of Engineering Science, Osaka University, Osaka, 2003.

[2] M. Okuyama, M. Noda and K. Yamashita: Mater. Sci. Semicond. Processing **2** (1999) 239.

[3] M. Noda, Y. Matsumuro, H. Sugiyama and M. Okuyama: Jpn. J. Appl. Phys. **38** (1999) 2275.

[4] M. Okuyama, H. Sugiyama and M. Noda: Appl. Surf. Sci. **154–155** (2000) 411.

[5] K. Kodama, M. Takahashi, D. Ricinschi, A. I. Lerescu, M. Noda and M. Okuyama: Jpn. J. Appl. Phys. **41** (2002) 2639.

[6] M. Takahashi, K. Kodama, T. Nakaiso, M. Noda and M. Okuyama: Integrated Ferroelectrics **40** (2001) 125.

[7] M. Noda, K. Kodama, I. Ikeuchi, M. Takahashi and M. Okuyama: Jpn. J. Appl. Phys. **42** (2003) 2055.

[8] M. Noda, K. Kodama, S. Kitai, M. Takahashi, T. Kanashima and M. Okuyama: J. Appl. Phys. **93** (2003) 4137.

[9] JCPDS-International Centre for Diffraction Data.

[10] W. F. Zhang, M. S. Zhang, Z. Yin, Y. Z. Gu, Z. L. Du and B. L. Yu: Appl. Phys. Lett. **75** (1999) 902.

[11] *Ceramics no Kagaku* (Science of Ceramics), ed. H. Yanai and M. Nagai (Gihodo Shuppan, Tokyo, 1993), 2nd ed., p. 152–156 [in Japanese].

[12] G. Hu, T. Tang and J. Xu: Jpn. J. Appl. Phys. **41** (2002) 6877.

[13] W. C. Shin, N. Y. Lee, S. O. Ryu, I. K. You, S. M. Cho, S. M. Yoon, B. G. Yu, J. B. Park, K. J. Choi, S. G. Yoon and W. J. Lee: Electrochem. Solid-State Lett. **6** (2003) F25.

[14] S. L. Miller, J. R. Schwank, R. D. Nasby and M. S. Rodgers: J. Appl. Phys. **70** (1991) 2849.

[15] *Denki-Jiki-Gaku Kiso Ron* (Basic Theory of Electricity and Magnetism), ed. Institute of Electrical Engineers (Denki-Gakkai, Tokyo, 1994), 7th ed., p. 43–46 [in Japanese].

[16] S. M. Sze, *Physics of Semiconductor Devices* (Wiley, New York, 1981), 2nd ed., p. 369–371.

Chapter 6

Conclusions

The principal results obtained in this thesis work are summarized as follows:

1. PRS spectral intensity has been calculated from Si surface potential as a function of dielectric constant and thickness of insulator film. It has been shown that properties of insulator film can be characterized by PRS spectral intensity. (Chap. 2)

2. E_1 critical point obtained from PRS spectrum linearly decreases with increasing tensile stress at Si surface. The decrease of E_1 is 0.01 eV per 10 MPa. It has been shown that the Si surface stress can be estimated by PRS. (Chap. 3)

3. Si surface stress caused by thermally oxidation decreases with increasing oxidation temperature. Estimated tensile stress is 150 MPa for 600°C oxidation and 90 MPa for 800°C oxidation. (Chap. 3)

4. The relationship between PRS spectral intensity and oxygen defects in HfO_2 film induced by excimer laser irradiation has been investigated. It has been brought out that PRS spectral intensity is reduced by existence of positive charges caused by oxygen defects. (Chap. 4)

5. Deposition and RTA conditions of HfO_2 thin films have been evaluated by PRS. For deposition in N_2 atmosphere, PRS spectral intensity becomes small because of positive charge caused by oxygen defects. PRS spectral intensity is increased by RTA at up to 600°C in N_2 or O_2, and decreased for more than 600°C because of interfacial layer growth. (Chap. 4)

6. Deposition and RTA conditions of PrO_x thin films have been evaluated by PRS. It is found that PrO_x film which has small oxygen defects and high dielectric constant can be obtained by deposition in O_2 atmosphere at high temperature (400°C). The interfacial layer growth is obviously observed by RTA at 600°C and above found by decrease of PRS spectral intensity. (Chap. 4)

7. PRS spectral intensity significantly increases and shifts to low energy side with poling of SBT/SiO_2/Si structure by negative voltage. The change of spectral intensity reflects increase of Si surface potential by remanent polarization in SBT film. Si surface potential obtained by dependence of PRS on modulation light power increases 0.17 eV by -1 V poling. (Chap. 5)

8. The memory retention property of SBT film has been characterized by PRS spectral intensity. The spectral intensity decreases with decrease of remanent polarization as time passes. Using RTA process for deposition, decrease of PRS spectral intensity is suppressed. This means that the improvement of retention property can be characterized by contactless PRS. (Chap. 5)

9. PRS measurement with applying voltage using ITO transparent electrode has been performed. PRS spectral intensity shows a hysteresis characteristic which reflects C-V curve. (Chap. 5)

Vita

SOHGAWA Masayuki (寒川 雅之)

Masayuki SOHGAWA was born in Kawabe, Hidaka, Wakayama, Japan on April 4, 1977 (Showa 52). After graduating from Wakayama National College of Technology, Wakayama, Japan on March, 1998 (Heisei 10), he entered 3rd grade at School of Engineering Science, Osaka University and graduated on March, 2000 (Heisei 12). He entered Graduate School of Engineering Science, Osaka University on April, 2000 (Heisei 12). He received Master of Engineering degree in Electrical Engineering on March, 2002 (Heisei 14) from Osaka University.

Publications

Academic Journals

1. M. Sohgawa, M. Agata, T. Kanashima, K. Yamashita, K. Eriguchi, A. Fujimoto and M. Okuyama: "Nondestructive and Contactless Monitoring Technique of Si Surface Stress by Photoreflectance", Jpn. J. Appl. Phys. **40** (2001) 2844–2848

2. H. Kanda, M. Sohgawa, Y. Toyoshima, T. Kanashima and M. Okuyama: "Characterization of Si Interface in FIS Structure by Photoreflectance Spectroscopy", J. Korean Phys. Soc. **42** (2003) S1072–S1075

3. T. Kanashima, M. Sohgawa, H. Kanda, K. Ikeda and M. Okuyama: "Characterization of ZrO_2 and PrO_x Thin Films for High-k Gate Insulator Prepared by Pulsed Laser Deposition", J. Korean Phys. Soc. **42** (2003) S1357–S1361

4. M. Sohgawa, H. Kanda, T. Kanashima, A. Fujimoto and M. Okuyama: "Characterization of Ferroelectric Thin Film/SiO_2/Si Structure by Photoreflectance", Ferroelectrics **303** (2004) 119–123

5. M. Sohgawa, M. Yoshida, T. Kanashima, A. Fujimoto and M. Okuyama: "Electrodeless Characterization of Memorized States of MFIS Structure by Photoreflectance Spectroscopy", J. Korean Phys. Soc. **46** (2005) 262–264

6. T. Kanashima, K. Ikeda, T. Tada, M. Sohgawa and M. Okuyama: "Electron Spin Resonance Characterization of the Defects in High-k HfO_2 Thin Film Prepared by Pulsed Laser Deposition", J. Korean Phys. Soc. **46** (2005) 258–261

7. M. Sohgawa, M. Yoshida, T. Naoyama, T. Tada, K. Ikeda, T. Kanashima, A. Fujimoto and M. Okuyama: "Contactless Characterization of Fixed Charge in HfO_2 Thin Film by Photoreflectance", to be published in Jpn. J. Appl. Phys.

Proceedings of Conferences

1. M. Agata, M. Sohgawa, O. Maida, K. Eriguchi, A. Fujimoto, T. Kanashima and M. Okuyama: "Optical Characterization of Gate Oxide Charging Damage by Photoreflectance Spectroscopy", *IEICE Tech. Rep. SDM99-173* (the Institute of Electronics, Information and Communication Engineers, Tokyo, 1999) p. 75–p. 80 [in Japanese]

2. M. Agata, M. Sohgawa, O. Maida, K. Eriguchi, A. Fujimoto, T. Kanashima and M. Okuyama: "Optical Characterization of Antenna-Area-Dependent Gate Oxide Charging Damage in MOS Capacitors by Photoreflectance Spectroscopy", *Ext. Abstr. 5th Int. Symp. Plasma-Process Induced Damage, Santa Clara, 2000* (American Vacuum Society, Santa Clara, 2000) p. 97–p. 100

3. M. Sohgawa, T. Kanashima, M. Agata, K. Yamashita, M. Okuyama, A. Fujimoto and K. Eriguchi:"Non-Destructive and Contactless Monitoring Technique of Si Surface Stress by Photoreflectance", *Ext. Abstr. Int. Conf. Solid State Devices and Mater. (SSDM 2000), Sendai, 2000* (Business Center for Academic Societies Japan, Tokyo, 2000) p. 456–p. 457

4. S. Kitai, M. Sohgawa, H. Kanda, T. Kanashima and M. Okuyama: "Preparation and Characterization of ZrO_2 High-k Gate Insulators films by PLD", *IEICE Tech. Rep. SDM2001-56* (the Institute of Electronics, Information and Communication Engineers, Tokyo, 2001) p. 24–p. 29 [in Japanese]

5. M. Sohgawa, S. Kitai, H. Kanda, T. Kanashima, A. Fujimoto and M. Okuyama: "Preparation and Characterization of ZrO_2/Si Structure", *Ext. Abstr. Int. Workshop Gate Insulator (IWGI 2001), Tokyo, 2001* (Business Center for Academic Societies Japan, Tokyo, 2001) p. 170–p. 173

6. S. Kitai, M. Sohgawa, H. Kanda, T. Kanashima and M. Okuyama: "Preparation of PrO_x Gate Insulators using Pulsed Laser Deposition", *IEICE Tech. Rep. SDM2001-185* (the Institute of Electronics, Information and Communication Engineers, Tokyo, 2001) p. 11–p. 16 [in Japanese]

7. T. Kanashima, S. Kitai, M. Sohgawa, H. Kanda and M. Okuyama: "Preparation by Pulsed Laser Deposition and Characterization of ZrO_2, HfO_2 and PrO_x Thin Films for High-k Gate Insulator", *Proc. 13th IEEE Int. Symp. Appl. Ferroelectrics (ISAF 2002), Nara, 2002* (IEEE, Piscataway, 2002) p. 199–p. 202

8. M. Sohgawa, H. Kanda, T. Kanashima, A. Fujimoto and M. Okuyama: "Characterization of Si Surface Stress in Various Dielectric Thin Film/Si Structure by Photoreflectance Spec-

troscopy", *Ext. Abstr. Int. Conf. Solid State Devices and Mater. (SSDM 2002), Nagoya, 2002* (Business Center for Academic Societies Japan, Tokyo, 2002) p. 54–p. 55

9. T. Kanashima, M. Sohgawa, K. Ikeda, H. Kanda and M. Okuyama: "Electrical and Optical Properties of PrO_x Thin Film for High-k Gate Insulator", *IEICE Tech. Rep. SDM2002-219* (the Institute of Electronics, Information and Communication Engineers, Tokyo, 2002) p. 45–p. 49 [in Japanese]

10. T. Kanashima, M. Sohgawa, K. Ikeda, M. Yoshida and M. Okuyama: "Characterization of HfO_2 interface deposited by PLD", *IEICE Tech. Rep. SDM2003-187* (the Institute of Electronics, Information and Communication Engineers, Tokyo, 2003) p. 51–p. 56 [in Japanese]

11. T. Kanashima, K. Ikeda, T. Tada, M. Sohgawa and M. Okuyama: "Characterization of Defects in HfO_2 by ESR", *IEICE Tech. Rep. SDM2004-54* (the Institute of Electronics, Information and Communication Engineers, Tokyo, 2004) p. 43–p. 48 [in Japanese]

12. M. Sohgawa, M. Yoshida, T. Naoyama, T. Tada, K. Ikeda, T. Kanashima, A. Fujimoto and M. Okuyama: "Contactless Characterization of Fixed Charge in HfO_2 Thin Film by Photoreflectance", *Ext. Abstr. Int. Conf. Solid State Devices and Mater. (SSDM 2004), Tokyo, 2004* (Business Center for Academic Societies Japan, Tokyo, 2004) p. 536–p. 537

13. M. Sohgawa, T. Kanashima M. Yoshida, T. Tada, M. Okuyama and A. Fujimoto: "Characterization of Fixed Charge in High-k Dielectric Thin Film by Photoreflectance", *IEICE Tech. Rep. SDM2004-196* (the Institute of Electronics, Information and Communication Engineers, Tokyo, 2004) p. 25–p. 30 [in Japanese]

Presentation of International Conferences

1. M. Agata, M. Sohgawa, O. Maida, K. Eriguchi, A. Fujimoto, T. Kanashima and M. Okuyama: "Optical Characterization of Antenna-Area-Dependent Gate Oxide Charging Damage in MOS Capacitors by Photoreflectance Spectroscopy", 5th Int. Symp. Plasma-Process Induced Damage (P2ID'00), May 2000, Santa Clara CA USA

2. M. Sohgawa, T. Kanashima, M. Agata, K. Yamashita, M. Okuyama, A. Fujimoto and K. Eriguchi:"Non-Destructive and Contactless Monitoring Technique of Si Surface Stress by Photoreflectance", 2000 Int. Conf. Solid State Devices and Mater. (SSDM 2000), August 2000, Sendai Japan

3. M. Sohgawa, S. Kitai, H. Kanda, T. Kanashima, A. Fujimoto and M. Okuyama: "Preparation and Characterization of ZrO_2/Si Structure", 2001 Int. Workshop Gate Insulator (IWGI 2001), November 2001, Tokyo Japan

4. T. Kanashima, S. Kitai, M. Sohgawa, H. Kanda and M. Okuyama: "Preparation by Pulsed Laser Deposition and Characterization of ZrO_2, HfO_2 and PrO_x Thin Films for High-k Gate Insulator", Int. Joint Conf. Appl. Ferroelectrics (IFFF 2002), May 2002, Nara Japan

5. H. Kanda, M. Sohgawa, Y. Toyoshima, T. Kanashima, A. Fujimoto and M. Okuyama: "Characterization of Si Interface in FIS Structure by Photoreflectance Spectroscopy", 4th Japan-Korea Conf. Ferroelectrics, August 2002, Osaka Japan

6. T. Kanashima, M. Sohgawa, H. Kanda, K. Ikeda and M. Okuyama: "Characterization of ZrO_2 and PrO_x Thin Films for High-k Gate Insulator Prepared by Pulsed Laser Deposition", 4th Japan-Korea Conf. Ferroelectrics, August 2002, Osaka Japan

7. M. Sohgawa, H. Kanda, T. Kanashima, A. Fujimoto and M. Okuyama: "Characterization of Si Surface Stress in Various Dielectric Thin Film/Si Structure by Photoreflectance Spectroscopy", 2002 Int. Conf. Solid State Devices and Mater. (SSDM 2002), September 2002, Nagoya Japan

8. M. Sohgawa, H. Kanda, T. Kanashima, A. Fujimoto, and M. Okuyama: "Characterization of Ferroelectric Thin Film/SiO_2/Si Structure by Photoreflectance", 10th European Meet. Ferroelectricity (EMF 2003), August 2003, Cambridge UK

9. M. Sohgawa, M. Yoshida, T. Kanashima, A. Fujimoto and M. Okuyama: "Electrodeless Characterization of Memorized States of MFIS Structure by Photoreflectance Spectroscopy", 5th Korea-Japan Conf. Ferroelectricity (KJC-FE5), August 2004, Seoul Korea

10. T. Kanashima, K. Ikeda, T. Tada, M. Sohgawa and M. Okuyama: "Electron Spin Resonance Characterization of the Defects in High-k HfO_2 Thin Film Prepared by Pulsed Laser Deposition", 5th Korea-Japan Conf. Ferroelectricity (KJC-FE5), August 2004, Seoul Korea

11. M. Sohgawa, M. Yoshida, T. Naoyama, T. Tada, K. Ikeda, T. Kanashima, A. Fujimoto and M. Okuyama: "Contactless Characterization of Fixed Charge in HfO_2 Thin Film by Photoreflectance", 2004 Int. Conf. Solid State Devices and Mater. (SSDM 2004), September 2004, Tokyo Japan

12. M. Sohgawa, M. Yoshida, T. Kanashima and M. Okuyama: "Characterization of Space Oxide Charge in HfO_2 Thin Film for High-k Gate Insulator by Photoreflectance Spectroscopy", Int. Workshop Mater. Sci. and Nano-Eng., December 2004, Osaka Japan

Domestic Meetings

1. M. Agata, M. Sohgawa, O. Maida, K. Eriguchi, A. Fujimoto, T. Kanashima and M. Okuyama: "Optical Characterization of Gate Oxide Charging Damage by Photoreflectance Spectroscopy", Meet. Silicon Devices and Mater.; Institute of Electronics, Information and Communication Engineers, December 1999, Nara

2. M. Agata, M. Sohgawa, K. Eriguchi, A. Fujimoto, T. Kanashima, K. Yamashita and M. Okuyama: "Analysis of the Strain at the SiO_2/Si/ Interface by Photoreflectance Spectroscopy", 47th Spring Meet. 2000; Japan Society of Applied Physics and Related Societies, 31a-YH-4, March 2000, Tokyo

3. M. Sohgawa, K. Eriguchi, A. Fujimoto, T. Kanashima and M. Okuyama: "Evaluation of the Si/SiO_2 Interface Stress by Photoreflectance Spectroscopy", 61st Autumn Meet. 2000; Japan Society of Applied Physics, 5p-ZC-6, September 2000, Sapporo

4. M. Sohgawa, H. Kanda, S. Kitai, M. Ueno, K. Eriguchi, A. Fujimoto, T. Kanashima and M. Okuyama: "Evaluation of the High-k Dielectric Film/Si Interface by Photoreflectance Spectroscopy", 48th Spring Meet. 2001; Japan Society of Applied Physics and Related Societies, 28p-C-2, March 2001, Tokyo

5. S. Kitai, M. Sohgawa, H. Kanda, T. Kanashima and M. Okuyama: "Preparation and Characterization of ZrO_2 High-k Gate Insulators films by PLD", Meet. Silicon Devices and Mater.; Institute of Electronics, Information and Communication Engineers, June 2001, Hiroshima

6. M. Okuyama, T. Kanashima, S. Kitai M. Ueno, O. Maida, M. Sohgawa and H. Kanda: "Zr, Hf および Lanthanoid 酸化物 High-k ゲート絶縁膜の作製 ", 関西支部 2001 年度第 1 回研究会; Surface Science Society of Japan, June 2001, Osaka

7. H. Kanda, M. Sohgawa, S. Kitai, T. Kanashima, K. Kodama, M. Okuyama, A. Fujimoto and K. Eriguchi: "Characterization of the Interface Si in FIS Structure by Photoreflectance Spectroscopy", 62nd Autumn Meet. 2001; Japan Society of Applied Physics, 11a-T-11, September 2001, Aichi

8. S. Fujita, S. Kitai, M. Sohgawa, H. Kanda, T. Kanashima, M. Okuyama and H. Ohashi: "Photo-induced Evaporation by High-flux Synchrotron Radiation from Figure-8 Undulator", 62nd Autumn Meet. 2001; Japan Society of Applied Physics, 13a-G-11, September 2001, Aichi

9. S. Kitai, M. Sohgawa, H. Kanda, T. Kanashima and M. Okuyama: "Preparation of PrO_x High-k Gate Insulator by PLD and Its Characterization", Meet. Electron. Mater.; Electronics, Information and Systems Society, Institute of Electrical Engineers of Japan, September 2001, Tokyo

10. S. Kitai, M. Sohgawa, H. Kanda, T. Kanashima and M. Okuyama: "Preparation of PrO_x Gate Insulators using Pulsed Laser Deposition", Meet. Silicon Devices and Mater.; Institute of Electronics, Information and Communication Engineers, December 2001, Nara

11. M. Sohgawa, S. Kitai, H. Kanda, T. Kanashima, A. Fujimoto and M. Okuyama: "Preparation and Characterization of High-k Gate Dielectric Films", 49th Spring Meet. 2002; Japan Society of Applied Physics and Related Societies, 29p-A-5, March 2002, Kanagawa

12. H. Kanda, M. Sohgawa, S. Kitai, K. Kodama, Y. Toyoshima, T. Kanashima, M. Okuyama, A. Fujimoto and K. Eriguchi: "Characterization of the Interface Si in FIS Structure by Photoreflectance Spectroscopy (2)", 49th Spring Meet. 2002; Japan Society of Applied Physics and Related Societies, 30a-ZA-9, March 2002, Kanagawa

13. S. Fujita, T. Orita, M. Sohgawa, T. Kanashima, M. Okuyama and H. Ohashi: "Preparation of Fuluoride Thin Films by High-flux Soft X-ray Ablation from Undulator", 49th Spring Meet. 2002; Japan Society of Applied Physics and Related Societies, 27a-G-9, March 2002, Kanagawa

14. M Sohgawa, H. Kanda, T. Kanashima, A. Fujimoto and M. Okuyama: "Evaluation of High-k/SiO_2/Si Structure by Photoreflectance Spectroscopy", 63rd Autumn Meet. 2002; Japan Society of Applied Physics, 27a-E-10, September 2002, Niigata

15. H. Kanda, M. Sohgawa, Y. Toyoshima, T. Kanashima, M. Okuyama, A. Fujimoto and K. Eriguchi: "Characterization of the SiO_2/Si Interface in MFIS Structure using SBT and PZT by Optical Method", 63rd Autumn Meet. 2002; Japan Society of Applied Physics, 24p-P4-15, September 2002, Niigata

16. T. Kanashima, M. Sohgawa, K. Ikeda, H. Kanda and M. Okuyama: "Electrical and Optical Properties of PrO_x Thin Film for High-k Gate Insulator", Meet. Silicon Devices and Mater.; Institute of Electronics, Information and Communication Engineers, December 2002, Kyoto

17. K. Ikeda, M. Sohgawa, T. Kanashima and M. Okuyama: "RTA Effects of PrO_x Thin Film Prepared by PLD", 50th Spring Meet. 2003; Japan Society of Applied Physics and Related Societies, 28p-ZW-20, March 2003, Kanagawa

18. S. Fujita, T. Tada, T. Kanashima, M. Sohgawa, H. Kanda, M. Okuyama, H. Ohashi Y. Tamenori and E. Ishiguro: "Photo-induced Etching by High-flux and High-density Synchrotron Radiation from Figure-8 Undulator", 50th Spring Meet. 2003; Japan Society of Applied Physics and Related Societies, 27p-YL-5, March 2003, Kanagawa

19. M. Sohgawa, M. Yoshida, T. Kanashima, A. Fujimoto and M. Okuyama: "Analysis of Ferroelectric Thin Film/SiO_2/Si Structure by Photoreflectance", 64th Autumn Meet. 2003; Japan Society of Applied Physics, 30a-T-11, August 2003, Fukuoka

20. M. Sohgawa: "フォトレフレクタンス分光法による強誘電体/SiO_2/Si 構造の評価", 2003 STARC Symposium; Semiconductor Technology Academic Research Center, September 2003, Osaka

21. T. Kanashima, M. Sohgawa, K. Ikeda, M. Yoshida and M. Okuyama: "Characterization of HfO_2 interface deposited by PLD", Meet. Silicon Devices and Mater.; Institute of Electronics, Information and Communication Engineers, December 2003, Nara

22. M. Yoshida, T. Naoyama, M. Sohgawa, T. Kanashima, A. Fujimoto and M. Okuyama: "Characterization of HfO_2/Si Structure by Photoreflectance Spectroscopy", 51th Spring Meet. 2004; Japan Society of Applied Physics and Related Societies, 29p-C-11, March 2004, Tokyo

23. K. Ikeda, T. Tada, M. Sohgawa, T. Kanashima and M. Okuyama: "ESR Characterization of Defects in HfO_2 Thin Films Prepared by PLD", 51th Spring Meet. 2004; Japan Society of Applied Physics and Related Societies, 29p-C-12, March 2004, Tokyo

24. T. Kanashima, K. Ikeda, T. Tada, M. Sohgawa and M. Okuyama: "Characterization of Defects in HfO_2 by ESR", Meet. Silicon Devices and Mater.; Institute of Electronics, Information and Communication Engineers, June 2004, Tokyo

25. M. Sohgawa, M. Yoshida, T. Kanashima, A. Fujimoto and M. Okuyama: "Contactless Characterization of Memorized States of MFIS Structure by Photoreflectance", 65th Autumn Meet. 2004; Japan Society of Applied Physics, 4a-Y-6, September 2004, Sendai

26. M. Sohgawa, T. Kanashima M. Yoshida, T. Tada, M. Okuyama and A. Fujimoto: "Characterization of Fixed Charge in High-k Dielectric Thin Film by Photoreflectance", Meet. Silicon Devices and Mater.; Institute of Electronics, Information and Communication Engineers, December 2004, Kyoto

Index